Influence of a settling particle on a Burgers vortex

by

Yohsuke TANAKA

(田中 洋介 83105805)

A thesis submitted
to
Department of Mechanical Engineering,
Graduate School of Engineering
in partial fulfilment of the requirements
for the degree
of
Doctor of Engineering

Advisor: Professor Toshitsugu TANAKA

OSAKA UNIVERSITY

Suita, Osaka

March, 2008

Abstract

In the present study, as an elementary physics for a particle-laden turbulent flow, the influence of a settling particle on a Burgers vortex is observed by using the Particle Image Velocimetry (PIV). A Burgers vortex, having the vortex axis directed in the gravitational direction, is generated in a cylindrical water tank, and a particle is gravitationally settled around the vortex axis. Four kinds of particles are used, and the resultant particle Reynolds numbers are ranged from 1430 to 3880. All particles shed vortices, and the measured particle motions are in equilibrium states with respect to the vortex motion. It is found that, in the near-particle region, the maximum vorticity increases in the case of particle passing through the forced vortex area, on the other hand, the maximum vorticity is not affected in the case of particle passing through the free vortex area. In the wake of particle, the interaction between the vortices shed from the particle and the Burgers vortex induces the large fluctuation of the circulation of the vortex. Moreover, the fragmentation and the mergence of the Burgers vortex core are observed.

Acknowledgments

I would first like to acknowledge my supervisor, Prof. Toshitsugu TANAKA, my vice supervisors, Prof. Takeo KAJISHIMA and Prof. Takehiko INABA for giving valuable advices and discussions. Many thanks also to the Prof. Yutaka TSUJI and Mr. Hiroshi IRUMAGAWA who gave me a good chance to conduct my research at Osaka university. Thanks to all staffs and members of Laboratory of Multiphase Flow Science and Engineering, who supported my daily activities in the laboratory. This work has supported from Research Fellowships of the Japan Society for the Promotion of Science for Young Scientists (DC2, no. 1337). Finally, I would like to thank my family for their encouragements and supports.

Contents

Chapter 1

Introduction

The prediction and control of turbulent flows laden with particles are practical engineering and environmental interests since these flows occur in energy convection devices (incinerators and pulverized coal combustion) and in environmental issues (atmospheric pollution, yellow-sand phenomenon and atmospheric scattering pollens). These flows have wide range of length and time scale, such as size distribution and response time scale of particle and vortex, in non-linear interactions of particles-vortices, particles-particles and vortices-vortices.

It has been found that, small amount of particles causes drastic changes in characteristics of turbulent flow such as turbulence intensities and Reynolds stress [1]-[7]. Even in the case of dilute particle-laden flows, the phenomenon is highly complicated, and is not yet understood essentially. Especially, the knowledge of particle-turbulent-eddy interaction, in which particle size is larger than smallest turbulence scale (Kolmogorov length scale), is insufficient due to difficulties in experimental measurements, theoretical analysis and numerical simulations.

In single-phase isotropic turbulence and wall-turbulence, the vortex structure, so-called "coherent structure" is observed. The coherent structures are composed of many tiny vortex tubes [8]-[14]. These vortex tubes play an important role in the momentum and energy transportation in turbulent flows. The vortex tube is modeled in terms of Burgers vortex [15]-[17], which is an analytical solution of Navier-Stokes equations [21],[22], and strained spiral vortex [18]-[20]. Kambe et al. [17] presented that fully developed turbulence is theoretically modeled by an ensemble of Burgers vortices distributed randomly in space. Thus, Burgers vortex is considered as an elementary vortex in turbulence.

A Burgers vortex [15] consists of a vortex tube superposed on an axisymmetric stagnation point flow. Figure 1.1 indicates the schematic image of physical features of Burgers vortex. The stagnation point flow convects the vorticity radially inward while

simultaneously straining the vortex tube in the axial direction. These processes exactly counterbalance the radial outward viscous dissipation of the vorticity.

In the cylindrical coordinate (r, θ, z), Burgers vortex has the exact solution of incompressible fluid written as [22]

$$u(r, \theta, z) = (-\alpha r, u_\theta(r), 2\alpha z), \tag{1.1}$$

where, α is the strain rate of the stagnation point flow field. The circumferential velocity $u_\theta(r)$ is given by

$$u_\theta(r) = \frac{\Gamma}{2\pi r}\left\{1 - \exp\left(-\frac{r^2}{l_b^2}\right)\right\}. \tag{1.2}$$

Here, Γ is the circulation, ν is the viscosity of the fluid, and $l_b(=\sqrt{2\nu/\alpha})$ is the Burgers length scale. The maximum value of $u_\theta(r)$ is found at the position $r \approx 1.12 l_b$ from Eq. (1.2) [22]. Substituting Eqs.(1.1) and (1.2) into the vorticity equation, the solution of the vorticity $\omega(r, \theta, z)$ is given as follows

$$\omega(r, \theta, z) = \left(0, 0, \frac{\Gamma}{\pi l_b^2}\exp\left(-\frac{r^2}{l_b^2}\right)\right). \tag{1.3}$$

A more detailed explanation of the derivation of the exact solution is provided in Appendix A.1.

Recently, by using direct numerical simulation, P.Bagchi and S.Balachander (2004) [23] indicated that the vortices shed from a particle larger than the Kolmogorov length scale have an influence on the total kinetic energy of turbulence in the isotropic turbulent flow. In their study, a stationary particle was subjected to a frozen isotropic turbulence superimposed on a uniform flow. The particle Reynolds number examined in their study is ranged from 50 to 600 and the particle diameter is ranged from 1.5 to 10 times of the Kolmogorov length scale. They observed enhancements of root-mean-square value of velocity fluctuation in the wake as effects of the particle on the isotropic turbulent flow.

The interaction between a single particle and a single vortex tube is considered as one of elementary interactions in turbulent flows laden with particles. Several researches have studied on the elementary interaction with different sizes of particles and conditions, as follows.

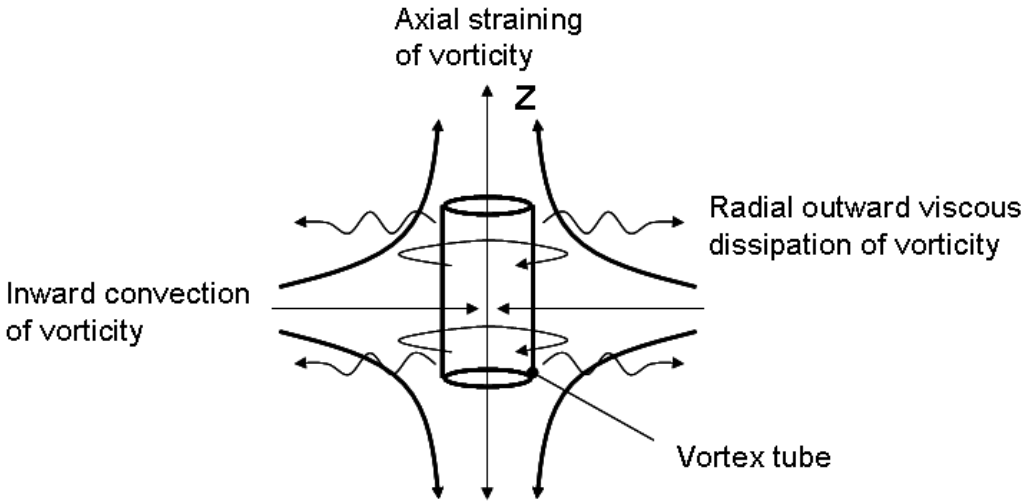

Figure 1.1: Schematic image of Burgers vortex

In the case of a particle larger than the Kolmogorov length scale, Kim et al. [24] and Niazmand et al. [25] numerically investigated that the lift force on a fixed particle caused by a vortex tube (or a pair of vortex tubes [26]) imposed on a uniform flow. As the vortex passes, the direction of the lift force changes. In the cases of small size vortex, the lift coefficient is lineally proportional to the circulation of the vortex tube. In the cases of large size vortex, the lift coefficient is linearly proportional to the maximum fluctuation velocity induced by the vortex tube.

An experimental study was performed on the interaction between a vortex tube and the wake of a particle [27]. The particle is supported by a support arm inserted from the outside of the water tank. The vortex generated is very similar to a Burgers vortex. The particle is initially moved toward the vortex at a constant velocity on a plane perpendicular to the vortex axis, and is then gradually brought to a rest point. In this experiment, the particle Reynolds numbers are sufficiently large to generate the unsteady vortex shed from the particle. The experiments were carried out for different diameters of particles by using a combination of Laser-Induced Fluorescence (LIF) and Particle Image Velocimetry (PIV). A variety of different interaction processes are observed to occur in the experiments, such as the entrainment of the particle wake into the vortex core, the formation of waves on the vortex, and the attraction of the vortex to the particle surface.

The focus of the present study is to examine the influence of the flow around a particle on a Burgers vortex, and the influence of the wake vortices shed from a particle

on a Burgers vortex. Concerning the interaction between a particle and a vortex, in the previous experimental and numerical studies, a particle is fixed in the flow. In the present study, the effects of a freely falling particle on a Burgers vortex is treated. A Burgers vortex, having the vortex axis directed in the gravitational direction, is generated in a cylindrical water tank. The observed plane perpendicular to the vortex axis is measured by using PIV. In the present experiments, the particle Reynolds number is sufficiently high to shed vortices. The experiments are made for four kinds of spherical particles that have the same diameter but different density. To visualize the structure of the interaction, quasi-three dimensional vorticity field is reconstructed by stacking two-dimensional vorticity fields, and the fluctuation of the intensity of the vortex caused by the shed vortices is observed.

This thesis is organized as follows: In chapter 2, experimental setup and conditions are explained. The selection of the optimal PIV algorithm for the present study is described. Visualization of the influence of the particle on the vortex is proposed. In chapter 3, the time change of the vortex intensity is observed without a settling particle. In stationary fluid, the flow around a settling particle and vortex structures are analyzed. In Chapter 4, the influence of the flow around a particle on a Burgers vortex and the interaction between the wake vortices shed from a particle and a Burgers vortex are proposed. The conclusions of this study are given in Chapter 5.

Chapter 2

Experiments

2.1 Introduction

In this chapter, the experimental setup, conditions, Particle Image Velocimetry (PIV) techniques and the visualization techniques for the examination of the influence of a settling particle on a Burgers vortex are presented. The components of the experimental setup, including the flow system of Burgers vortex, the optical system for PIV and the particle-detection system, are explained, respectively. In order to verify the generation of the Burgers vortex in the flow system, the circumferential velocity and the vorticity of the generated vortex are compared with the analytical solution of Burgers vortex. The conditions of Burgers vortex and settling particles are presented. The correspondence of the generated vortex and the vortex of an isotropic turbulent flow is clarified by using the length-scale relation between an isotropic turbulent flow and a Burgers vortex. Because the tracer particles used for PIV decrease over time in this setup, an optimal PIV algorithm which is robust in their decrease is selected. In the present experiment, a PIV measurement is performed in a plane perpendicular to the vortex axis, though a settling particle causes three dimensional flow structure. To make clear the effect of the three-dimensional flow structure on the two-dimensional flow measured on the plane, the superficial divergence on the measured plane is defined, and Balance between Vorticity and Divergence (BVD) plane is proposed to illustrate the correspondence between the vorticity and the divergence. In additionally, in order to visualize the vortex structures under the interaction between the Burgers vortex and vortices shed from a settling particle, quasi-three dimensional vorticity field is constructed by two dimensional vorticity fields obtained by PIV.

2.2 Experimental setup

The schematic diagram of the experimental setup is shown in Fig. 2.1. This system is composed of the flow system (**1-7**), the optical system for PIV(**8-12**) and the particle detection system (**13-15**).

The Burgers vortex is measured through the observation window installed at the lower part of the water tank by using PIV measurement. The test cross-section of the vortex is illuminated by the laser light sheet. The CMOS high-speed camera starts to capture the image when the settling particle is detected by the area sensor (as shown in the magnified view of Fig. 2.1). In the following subsections, the details of each system will be explained.

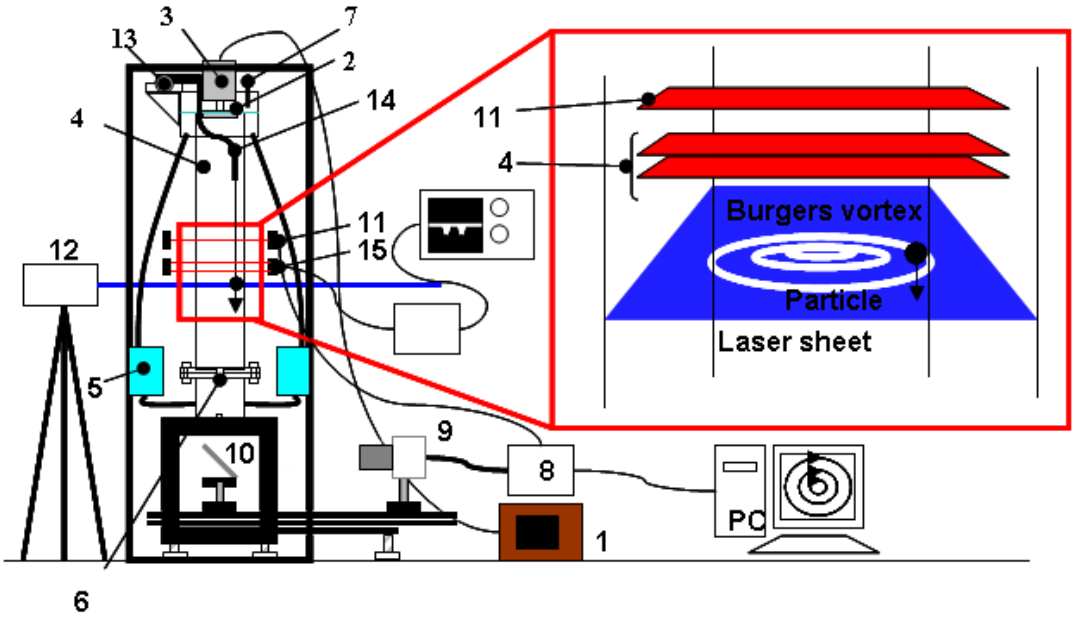

1. Motor controller
2. Rotating fan
3. Motor
4. Water tank
5. Pump
6. Oriffice meter
7. Digital thermometer
8. Camera controller
9. High speed camera (with color filter)
10. Mirror
11. Area sensor
12. Ar laser
13. X stage
14. Particle dispenser
15. Particle velocimetry

Figure 2.1: Experimental setup for the observation of the influence of a settling particle on a Burgers vortex

2.2.1 Flow system of Burgers vortex

Figure 2.2 shows that the flow system of Burgers vortex. A Burgers vortex in the lower part of the mathematical model is realized by four circulation pumps (BP-101K, Oriental Koshin) and the rotating fan (diameter: 60 mm, rotation: 400 rpm, motor: M425-001, Oriental motor) in the circularly water tank (inner diameter: 140 mm, height: 1000 mm).

In the water tank, the water flows downward. Because the fluid goes through the wide cross section of the upperpart of the water tank, which has the diameter of 140 mm, to the narrow cross section of the orifice, 20 mm in diameter, the stagnation point flow occurs. A vortex tube is generated by the rotating fan. Thus, a Burgers vortex is generated by these flows. As for the boundary condition of the analytic solution, the velocity field becomes infinity at $r \to \infty$. However, at the presented water tank, the velocity field becomes zero at the wall of the tank. To reduce an influence of the wall, the wall is installed at far from the center of the vortex.

In the flow system, the water is circulated through four pipelines by circulation pumps. In Fig. 2.2, only one circulation pipeline is illustrated. The flow rate is arbitrarily adjustable by the valves (G077, TAKAGI) equipped in the pipelines. The orifice plate at the bottom of the cylinder is also used as orifice flow meter. The flow rate is measured from the pressure difference across the orifice. The orifice plate is made of transparent acrylic so as to enable the visual observation through the plate.

The water jacket (cross section: 150×150 mm^2, height: 1 m) is attached around the tank to avoid an image deformation caused by the refraction when the test section is observed from the lateral direction and to focus the light sheet in the water tank. The space between the jacket and the tank is filled with water.

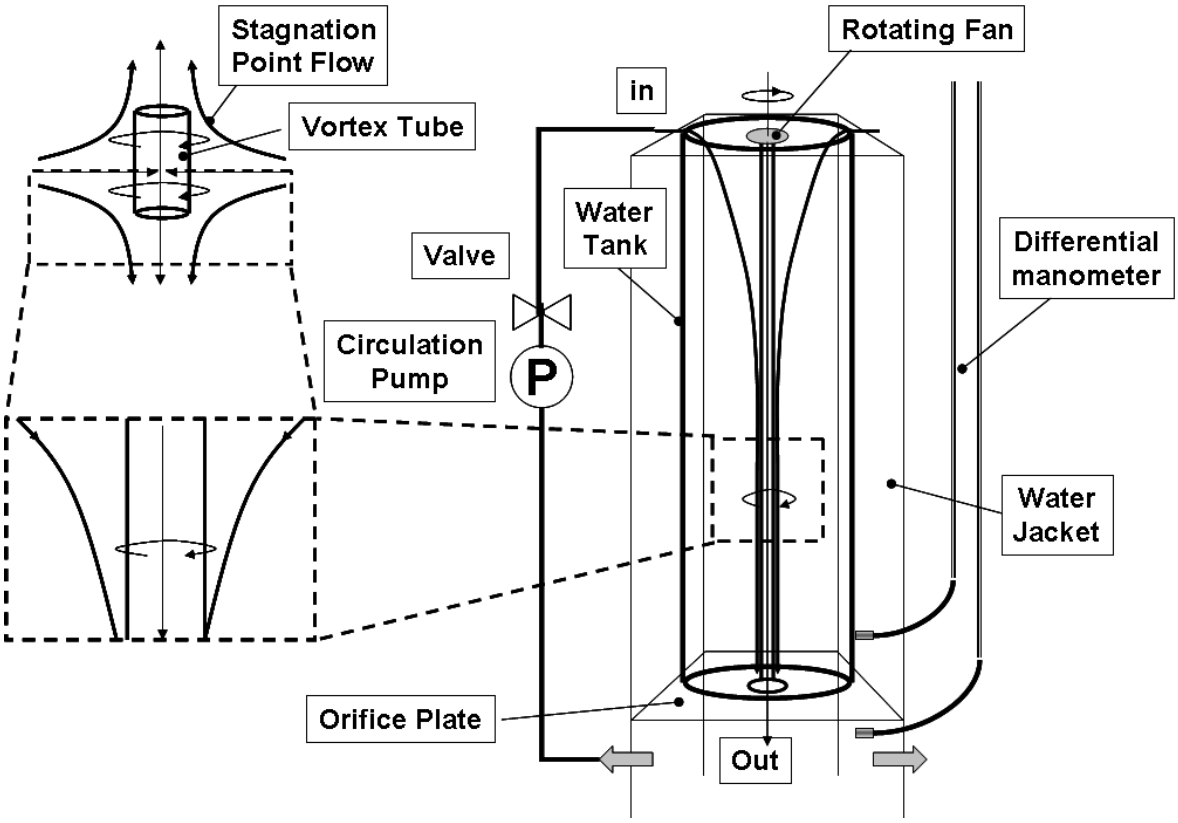

Figure 2.2: Flow system of Burgers vortex

2.2.2 Optical system for PIV

Figure 2.3 explains the optical system for PIV system which is mainly composed of an Ar laser (GLG3282, NEC) as a light source, a cylindrical lens as a transducer of laser light sheet and a high speed camera (Memrecam fx6000, NAC) as an observer.

The laser light sheet, transmitted from the laser beam by a cylindrical lens, illuminates the observation area. To intensify the light energy in the observation area, the laser sheet that passes through the water tank is reflected by the mirror attached on the outside surface of the water jacket.

The illuminated tracer particle's image in the observation area is reflected by the mirror under the water tank, and is observed by the high speed camera at 150 mm above the orifice plate. Fluorescence tracer particles, detailed in Appendix B.1, seeded in the area are excited by the light sheet, and the tracer particles emit an orange-red light. By using an orange-red filter (MC YA3, Kenko) attached to the lens, the scattering light (green-blue color) from the surface of the water tank, the water jacket, and a settling particle is eliminated.

PIV conditions are summarized in Table 2.1. The spatial resolution of the vortex is in the range of 1 to 61 mm, estimated from the grid interval and the observation area. The time resolution of the change of vortex is in the range of 1 to 62.5 Hz, estimated from the sampling rate and observation time.

Table 2.1: PIV conditions

Vector component	2 dimensional, 2 components
Spatial resolution of CMOS	0.13 [mm/pixel]
Recording frequency	125 [Hz]
Observation area	61×61 [mm^2]
Interrogation area	0.96×0.96 [mm^2]
Lens	f=105 [mm], f#=2.8, focal length 1300 [mm]
Camera	CMOS, 512×512 [pixel^2], 8 [bit]
Tracer	SP20SS with Rhodamin B, Averaged diamter: 73.5 [μm]
Lighting	Ar laser, CW, 2.8 [W], Thickness of light sheet: 2 [mm]
PIV algorithm	CEC-PIV
Vector number	57×57 [vectors], 250 [frames]
Measurement range of velocity	4.9 - 138 [mm/sec]

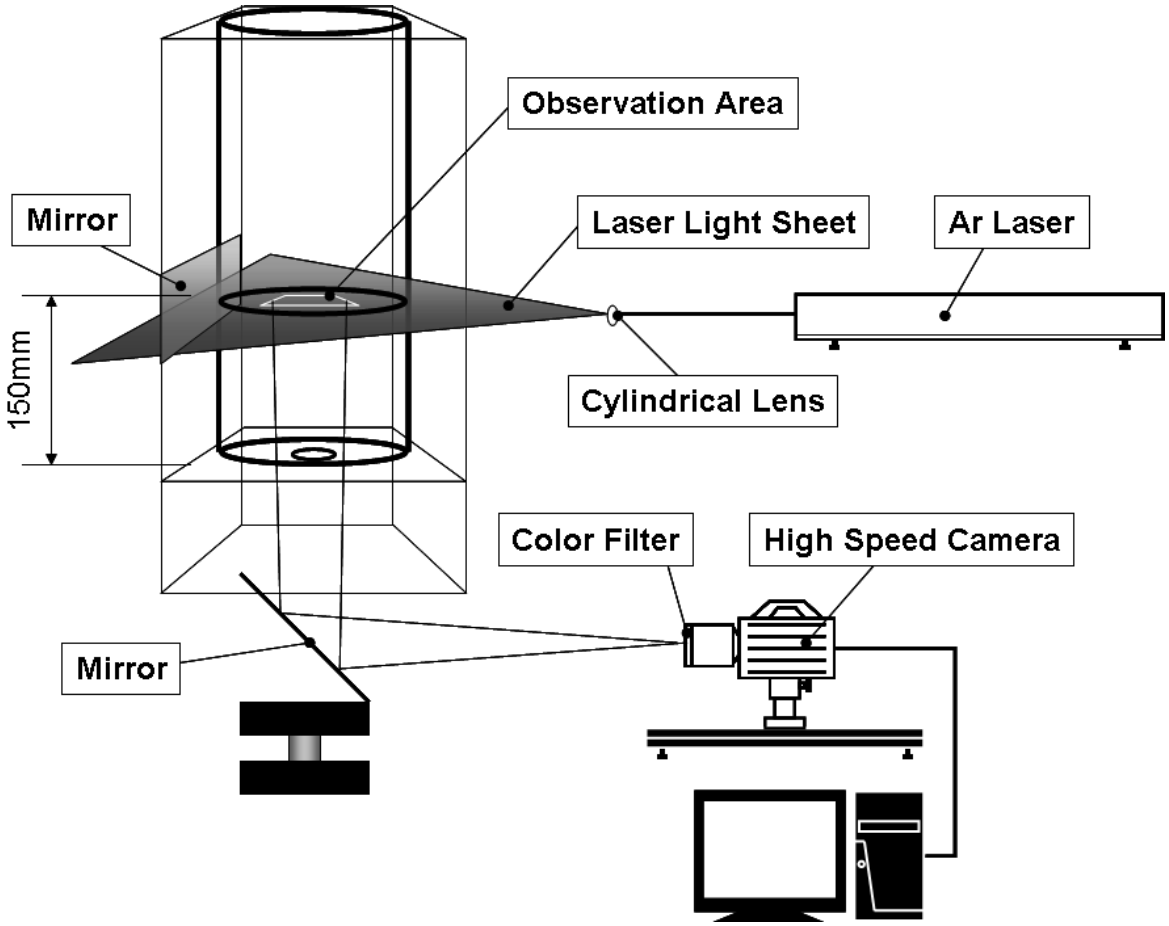

Figure 2.3: Optical system for PIV

2.2.3 Particle-detection system

The particle-detection system is made up of two main subsystems: the particle dispenser which enables a settling particle to be released reproducibly and the particle velocimetry system which measures the vertical component of particle velocity passing through the measuring area.

Particle dispenser

The particle dispenser is composed of an aluminum pipe (5 mm in outside diameter, 4 mm in inner diameter), a couple of shutters connected to the metal-based artificial muscle wire (0.25 mm in diameter, Biometal fiber: Toki corporation described in B.2), and a X-stage as shown in Fig. 2.4 .

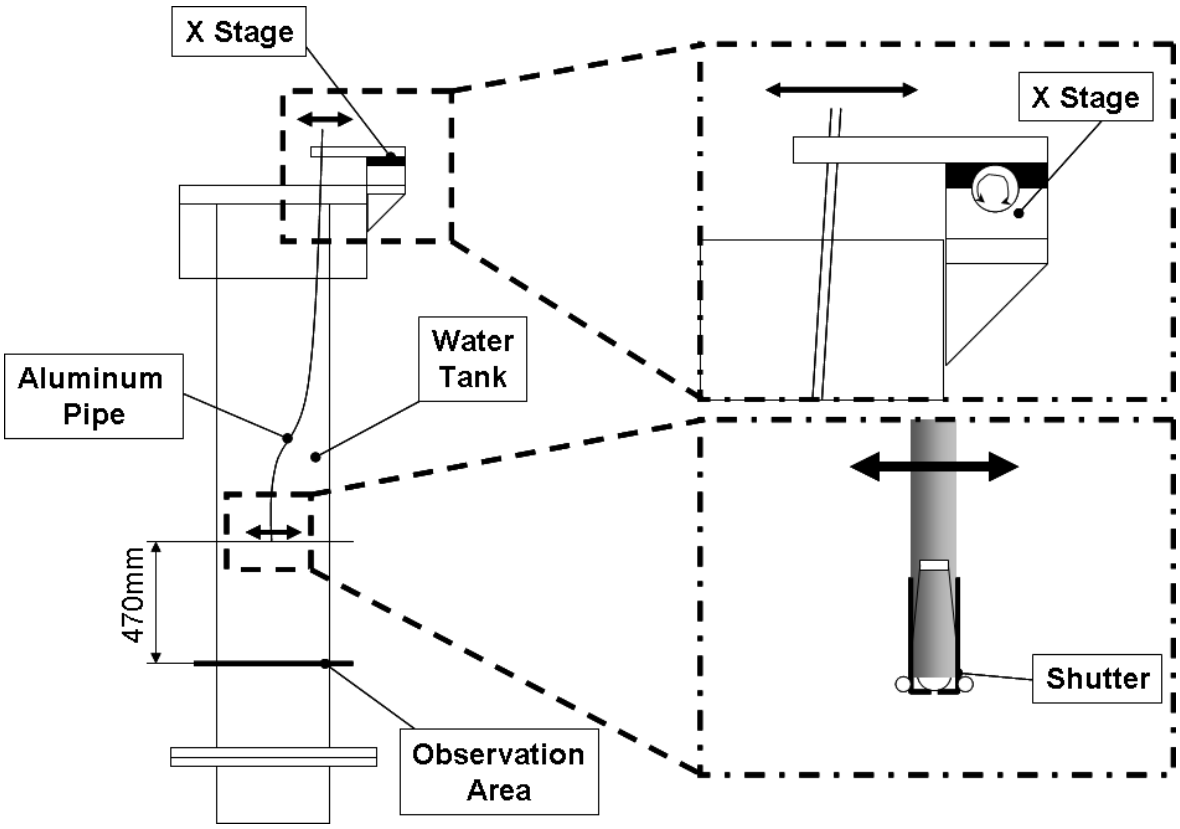

Figure 2.4: Particle dispenser

The particle dispenser is installed at 470 mm above the observation area, so that the particle velocity passing through the observation area can reach the terminal velocity for the presented conditions summarized in Table 2.3. The dispenser is mounted on the X stage (±15 mm) to adjust the particle initial position.

The setting procedure is as follows: The particle falls into the topside of the pipe, and the particle stops at the shutters attached to the end of the pipe. When current (DC 8 V, TE-Ⅱ, Olympus) is applied, the shutters are opened by contraction of the wire and the particle is released, and the shutters are closed by shutting down current as shown in Fig. 2.5. By using this dispenser, the standard deviation of the horizontal positions of the particle in the observation area is 8.87 mm.

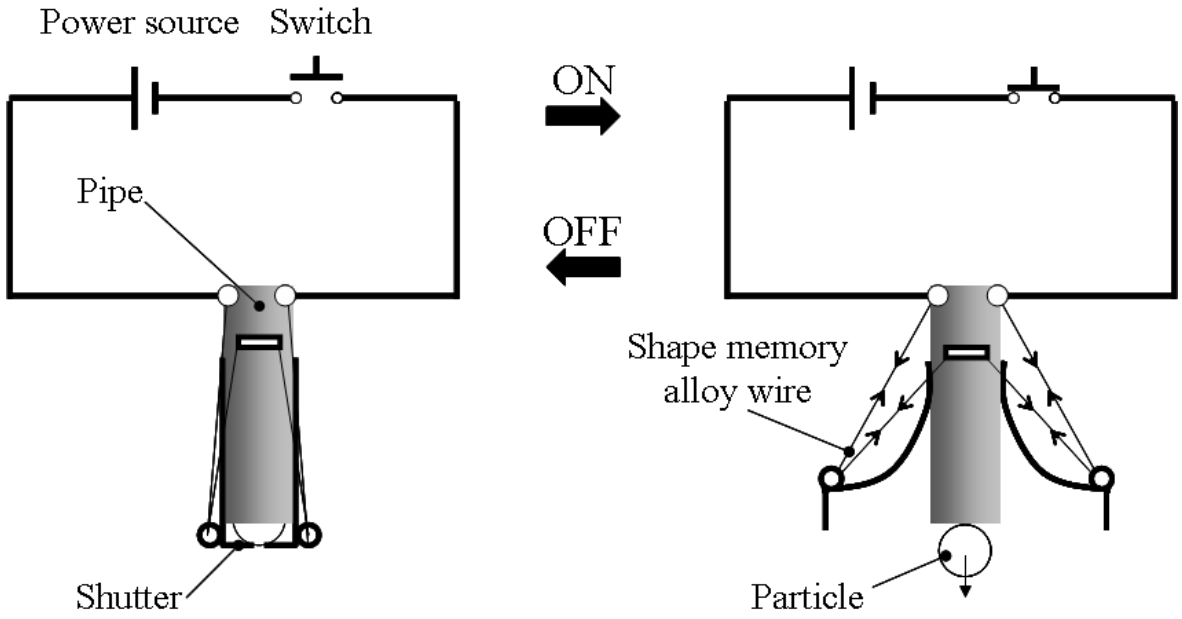

Figure 2.5: Electric circuit of particle dispenser

Particle velocimetry system

Figure 2.6 shows that the particle velocimetry system for the measurement of the vertical component of particle velocity is composed of a couple of area sensors (sampling rate: 12.5 kHz, width of laser sheet: 30 mm, transmitter: LX2-03T, receiver: LX2-03R and amplifier: LX2-V10 KEYENCE) and a digital signal recorder (Osiroscope: TDS2014, Tektronix) which records the output of the area sensors.

The measurement is made at 50 mm above the observation area. The particle velocity U is calculated by the spacing $L = 0.02$ m between the area sensors and the time delay ΔT of two signal peaks.

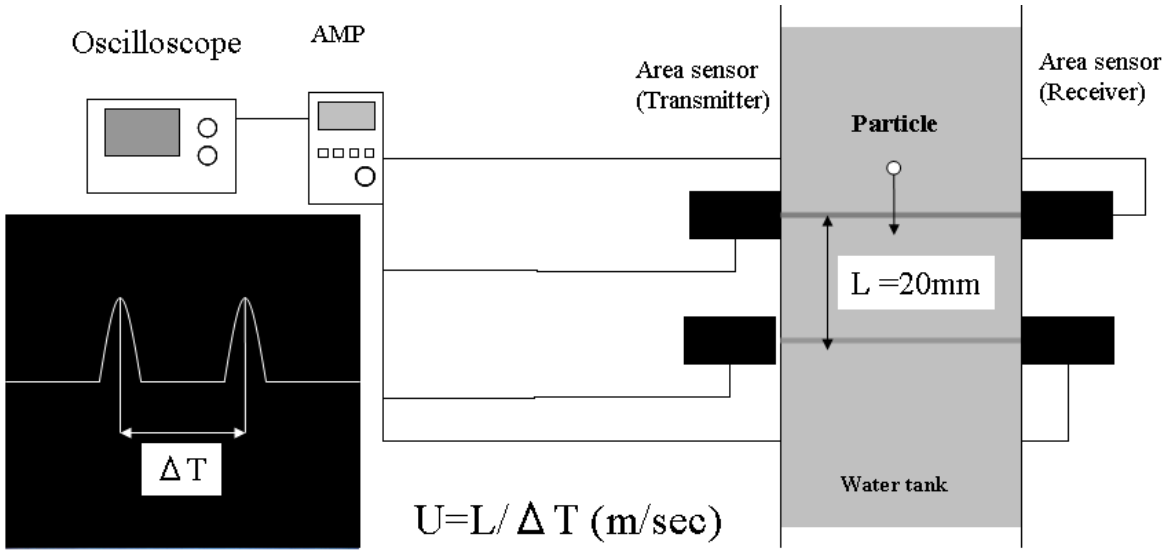

Figure 2.6: Particle velocimetry system

2.3 Experimental conditions

In this section, to clarify the correspondence of the generated vortex to the vortex of an isotropic turbulent flow, the length-scale relation between an isotropic turbulent flow and a Burgers vortex is used. To estimate the state of the particle motion with respect to the vortex motion, we introduce Stokes number. Additionally, the ratio of the particle size to Kolmogorov length scale is estimated.

2.3.1 Burgers vortex condition

Conditions of the Burgers vortex are shown in Table. 2.2. The water temperature controlled to be 31.1 ± 0.5 (C°). The temperature is observed by the digital thermometer (**7** in Fig. 2.1). Vortex Reynolds number is defined as $Re_\Gamma = \Gamma_0/\nu$, where the circulation Γ_0 is obtained in the area $r/l_b < 1.12$. At the observation area, the mean flow velocity $\overline{U}_z$ is measured by the orifice flow meter shown in Fig.2.2.

Kambe et al. [17] present that the relation between the Burgers vortex length scale l_b and Kolmogorov length scale η is given as follows, assuming that the rate of strain α is of the order of $2\alpha \approx v_{rms}/\lambda$,

$$\begin{aligned} l_b &= (2\nu/\alpha)^{1/2} = (4\nu\lambda/v_{rms})^{1/2} \\ &= (240\nu^3/\epsilon)^{1/4} \approx 3.9\eta, \end{aligned} \tag{2.1}$$

where λ is Taylor microscale, v_{rms}, root mean square value of velocity fluctuation and ϵ, the rate of dissipation of energy, respectively. In the present study, the radius of Burgers vortex is defined as $r = 1.12 l_b$. Substituting this radius into Eq. (2.1), the diameter d_v of Burgers vortex is given by 8.81η. It is observed that the most expected diameter is about 8 η in DNS database of homogeneous isotropic turbulence [13], and is 8-10η in DNS database of turbulent channel flow [14], respectively. Thus, the diameter of Burgers vortex is well consistent with the most expected diameter in turbulent flows.

Substituting the value l_b obtained from PIV data into Eq. (2.1), we obtain Kolmogorov length scale η, Kolmogorov velocity v_K and time τ_K. These variables are obtained from the following equations[30]:

$$\eta = (\nu^3/\epsilon)^{1/4} \tag{2.2}$$

$$v_K = (\epsilon\nu)^{1/4} \tag{2.3}$$

$$\tau_K = (\nu/\epsilon)^{1/2} \tag{2.4}$$

Where, ν is kinematic viscosity. Thus, scales of an isotropic turbulent flow which contained the Burgers vortex generated by the experimental setup can be estimated by Eqs. (2.2), (2.3) and (2.4), are presented in Table 2.2.

Table 2.2: Burgers vortex conditions

Water temperature	T [C°]	31.1 ± 0.5
Kinematic viscosity	ν $[m^2/sec]$	7.83×10^{-7}
Maximum circumferential velocity	$v_{\theta max}$ $[m/sec]$	41.99×10^{-3}
Vortex Reynolds number	Re_Γ [-]	6590
Mean flow velocity	$\overline{U}_z$ $[m/sec]$	19.4×10^{-3}
Burgers length scale	l_b $[m]$	15.8×10^{-3}
Kolmogorov length scale	η $[m]$	4.01×10^{-3}
Kolmogorov velocity	v_K $[m/sec]$	0.20×10^{-3}
Kolmogorov time	τ_K $[sec]$	20.57

2.3.2 Particle condition

In order to observe the influence of the particle on Burgers vortex, we used four kinds of particle (A,B,C, and D) as presented in Table 2.3. The diameter d_p of each particle is almost the same, but the density ρ_p is different. To estimate particle motions on the vortex tracking, Stokes number is defined as follows

$$St = \frac{\tau_p}{\tau_f}. \tag{2.5}$$

Here, τ_p and τ_f are the particle response time and the particle's residence time in the vortex, respectively. The Stokes number indicates the degree of particle tracking to the vortex for the particle motion. For $St \ll 1$, the particle will track the vortex motion, and shows in spiral motion. For $St \gg 1$, the particle motion will be independent of the vortex motion.

In the present study, the particle is exposed to the effect of the vortex tube after the release from the dispenser. Therefore, τ_f is defined as the time interval between the moment of releasing particle from the particle dispenser and the moment of particle

reaching the observation area. The particle response time τ_p is given by

$$\tau_p = \frac{2d_p^2(2\rho_p + \rho_f)}{3\mu Re_p C_d}. \tag{2.6}$$

In Eq. (2.6), virtual mass force is considered, because the particle density ρ_p is only about ten times of the fluid density ρ_f [31]. At the observation area, the range of the particle Reynolds number ($Re_p = d_p|\mathbf{u_f} - \mathbf{u_p}|/\nu$, $|\mathbf{u_f} - \mathbf{u_p}|$:relative velocity between the flow and the particle) shown in Table 2.3 is much larger than the Stokes drag range. All particles shed unsteady vortices as shown in Chap. 3. The relative velocity is obtained from the resultant vector described in Sec. 2.6.1. Therefore, the drag coefficient C_d is applied. The coefficient is derived from the empirical equation [32] in the range of $10^{-2} < Re_p < 3 \times 10^5$ as follows:

$$C_d = (2.25Re_p^{-0.31} + 0.36Re_p^{0.06})^{3.45}. \tag{2.7}$$

Table 2.3: Particle conditions

	A	B	C	D
Material	Glass	Alumina	Steal	Lead
d_p [mm]	2.96	2.98	3.00	2.99
ρ_p [kg/m^3]	2520	3600	7940	11520
ρ_f [kg/m^3]	995			
St [-]	0.05	0.07	0.16	0.22
τ_p [sec]	0.07	0.08	0.10	0.12
τ_f [sec]	1.33	1.01	0.63	0.54
Re_p [-]	1430	1940	3200	3880
$\|\mathbf{u_f} - \mathbf{u_p}\|$ [m/sec]	0.378	0.510	0.838	1.016
C_d [-]	0.44	0.42	0.40	0.39
V_{zexp} [m/sec]	0.378	0.508	0.838	1.019
V_{zemp} [m/sec]	0.363	0.487	0.823	1.022
$\overline{U}_z/V_{exp}$ [-]	0.051	0.038	0.023	0.019
d_p/η [-]	0.73	0.74	0.74	0.74

From the values of Stokes number in Table. 2.3, it is found that the time until particle reaches the cross section is longer than the particle response time, and all particle motion is in an equilibrium state with respect to the vortex motion. In the gravitational direction, the velocities of all particles reach terminal velocity by comparing the averaged particle velocity V_{zexp} (sample number=50) with V_{zemp} calculated by Eq. (2.7). Additionally, the ratio d_p/η of particle diameter to Kolmogorov length scale is presented.

2.4 Validation of generated Burgers vortex

Figure 2.7 indicates the time-averaged vorticity distribution (4 sec, 500 frames). The circularity value of the vortex is 0.865 at the contour line with respect to the maximum value of the circumferential velocity ($r/l_b \approx 1.12$). Here, a circularity value of 1.0 indicates a perfect circle. The circularity is measured by the image processing software (Image J).

Figure 2.8 shows the distributions of the measured circumferential velocity and the vorticity compared with the analytical solutions, Eqs. (1.2) and (1.3). ω' and V'_θ are non-dimensionalized by the maximum values of the circumferential velocity and the vorticity, respectively. The experimental results almost agree with analytical ones. Therefore, it is confirmed that the present setup generates a Burgers vortex. In the present study, the areas of $r/l_b < 1.12$ and $r/l_b > 1.12$ are defined as a forced vortex area and a free vortex area, respectively, although they are different from the a general definition [29].

Additionally, we evaluate the temporal stability of the vortex axis position. The position is defined as the point of the maximum vorticity. The position is measured by the longer time interval (4.0 sec) than the observation time (2.0 sec). The standard deviation of the position is obtained as 3.6 mm. This value is smaller than the diameter of the vortex 35.2 mm. Hence, it is found that the position is stable.

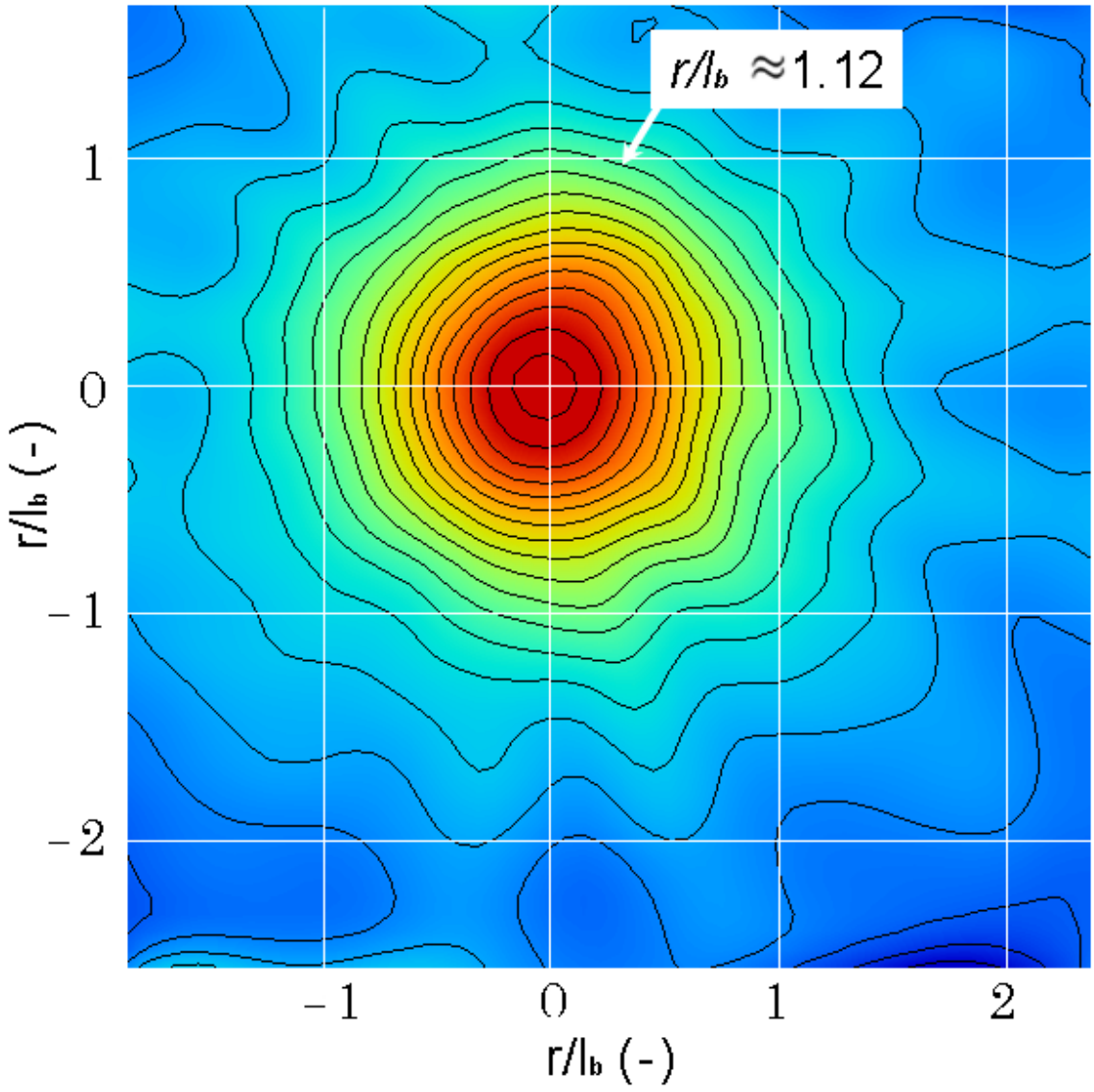

Figure 2.7: Time averaged vorticity distribution

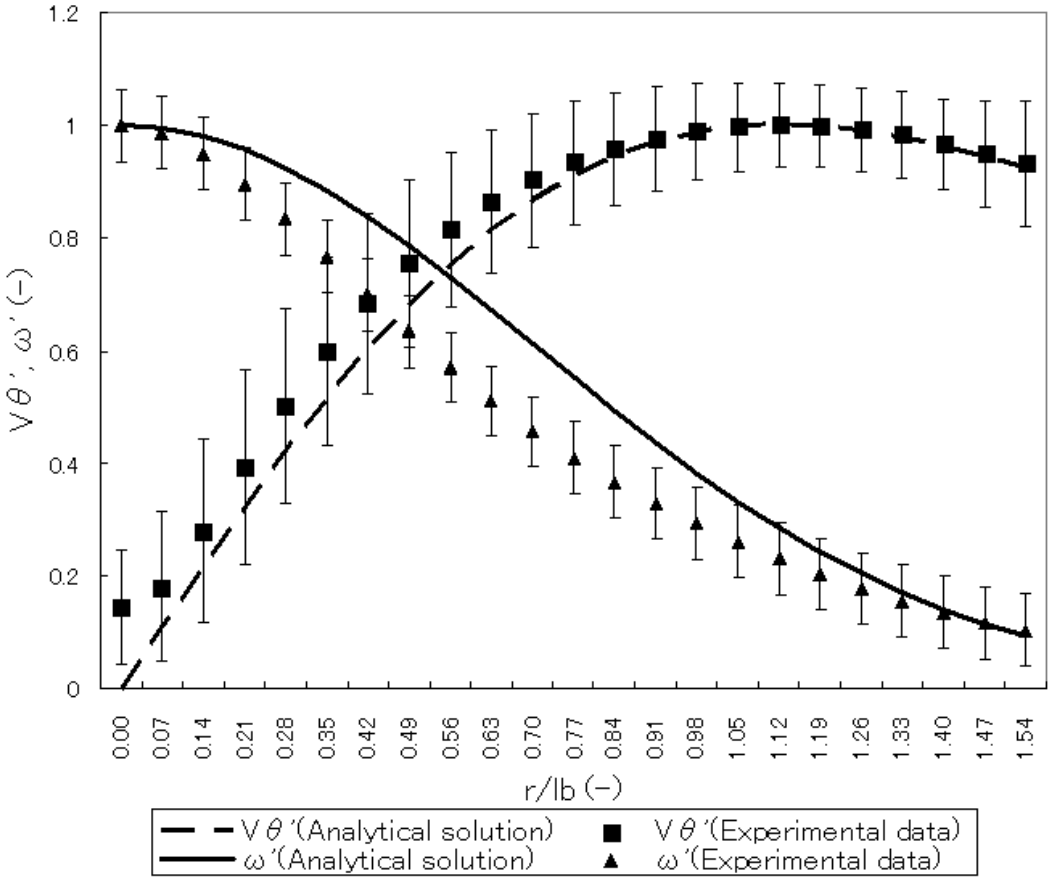

Figure 2.8: Distributions of fluid circumferential velocity and vorticity

2.5 Selection of optimal PIV algorithm

Particle image velocimetry (PIV) [33]-[34] is one of the optical flow measuring techniques, based on the image processing and several algorithms, such as CC-PIV (Cross-correlation PIV)[35], I-PIV (Iterative PIV) [36]-[40] and CEC-PIV (Correlation error correction PIV) [41], have been proposed.

Measurement accuracy depends on the number of tracer particles in the interrogation window. Because tracer particle is heavier than water, the number of particles decreases over time as shown in Fig. 2.9. In order to select the optimal PIV algorithm from these PIV algorithms for the present study, the measurement accuracy and the calculation time are compared with each other. Based on the resulting data, we examine the trade-off between the accuracy and the calculation time.

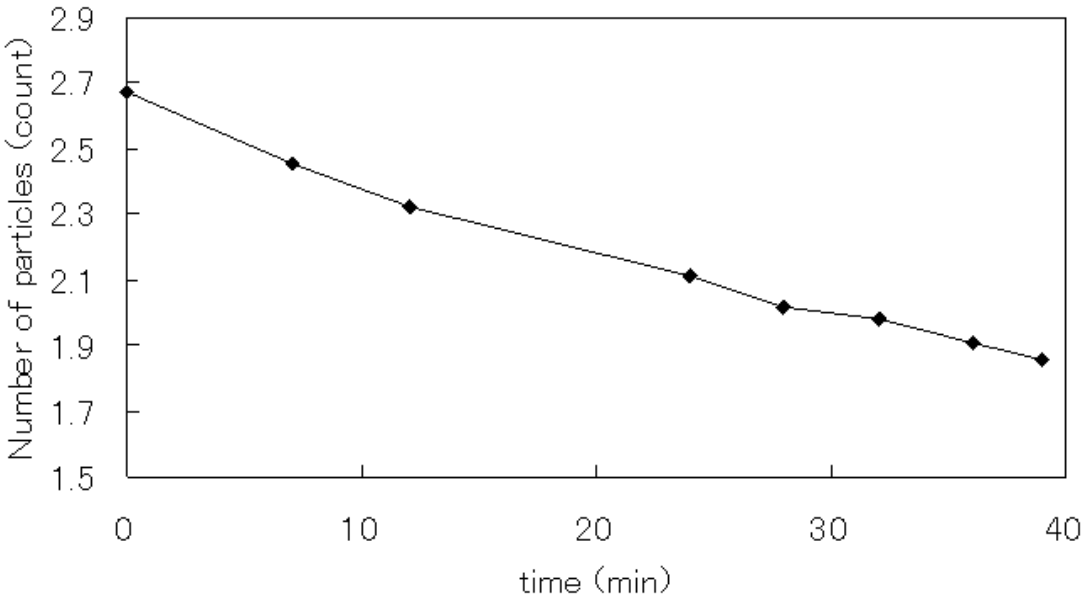

Figure 2.9: Temporal change of the number of particles in the interrogation window

2.5.1 Cross-correlation PIV (CC-PIV)

PIV measurement is used to obtain an instantaneous two-dimensional velocity data. The principle of PIV measurement is measuring the displacement of the tracer particles in the observed flow field during the known time interval. A representative example of PIV system is shown in Fig. 2.10. The flow field, seeded with tracer particles of neutral density, is illuminated by a laser light sheet and is recorded by a high speed camera.

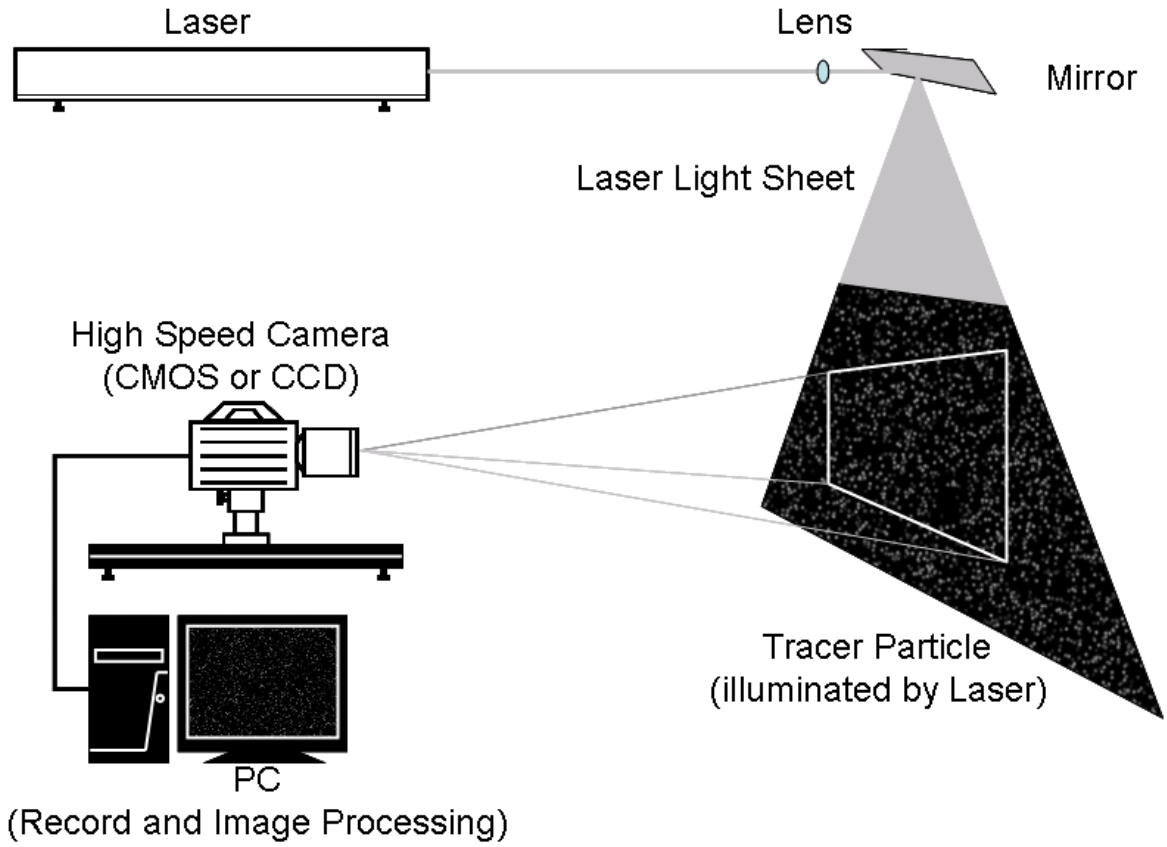

Figure 2.10: PIV system

The correlation method has been the most popular and conventional algorithm of PIV measurement [33]. The local displacement vector for two particle images of the first frame (t (sec)) and the second frame (t+Δt(sec)) is determined by cross-correlation table defined as follows:

$$C(x,y) = \frac{\sum_{i=0}^{i=N}\sum_{j=0}^{j=M}(S(i,j)-\bar{S}(i,j))(I(i+x,j+y)-\bar{I}(i,j))}{\sqrt{\sum_{i=0}^{i=N}\sum_{j=0}^{j=M}(S(i,j)-\bar{S}(i,j))\sum_{i=0}^{i=N}\sum_{j=0}^{j=M}(I(i+x,j+y)-\bar{I}(i,j))}}, \tag{2.8}$$

where, as shown in Fig. 2.11, $C(x,y)$ is the cross correlation table, $I(i,j)$ is the interrogation window in the first frame, and $S(i,j)$ is the search window in the second frame. $\bar{S}(i,j)$ and $\bar{I}(i,j)$ are their average value, respectively. $M \times N$ is an interrogation window size. Here, it is assumed that all the particles within these windows have moved homogeneously between the two illuminations.

In Figure 2.11(**b**), the cross-correlation coefficient is calculated in the place with which the interrogation window $I(i,j)$ has overlapped within the search window $S(i,j)$ and the cross-correlation table is calculated by moving the interrogation window for every pixel within the search window. The correlation table has one peak as shown in Fig. 2.11(**c**) and the local displacement vector $\mathbf{l}(x,y)$ corresponds to the displacement between the center of the table and the peak.

Three-point Gaussian peak fitting for a sub-pixel analysis is applied to the peak. This sub-pixel displacement $\mathbf{l}_{sub}(x,y) = (\Delta x, \Delta y)$ is defined as follows:

$$\Delta x = \frac{\log(C(x-1,y)) + \log(C(x+1,y))}{2\log(C(x-1,y)) + 4\log(C(x,y)) + 2\log(C(x+1,y))} \tag{2.9}$$

$$\Delta y = \frac{\log(C(x,y-1)) + \log(C(x,y+1))}{2\log(C(x,y-1)) + 4\log(C(x,y)) + 2\log(C(x,y+1))}. \tag{2.10}$$

Dividing the resultant vector of $\mathbf{l}(x.y)$ and $\mathbf{l}_{sub}(x.y)$ by the known interval Δt, the velocity vector $\mathbf{u}(x,y)$ is derived as follows:

$$\mathbf{u}(x,y) = \frac{\mathbf{l}(x,y) + \mathbf{l}_{sub}(x.y)}{\Delta t}. \tag{2.11}$$

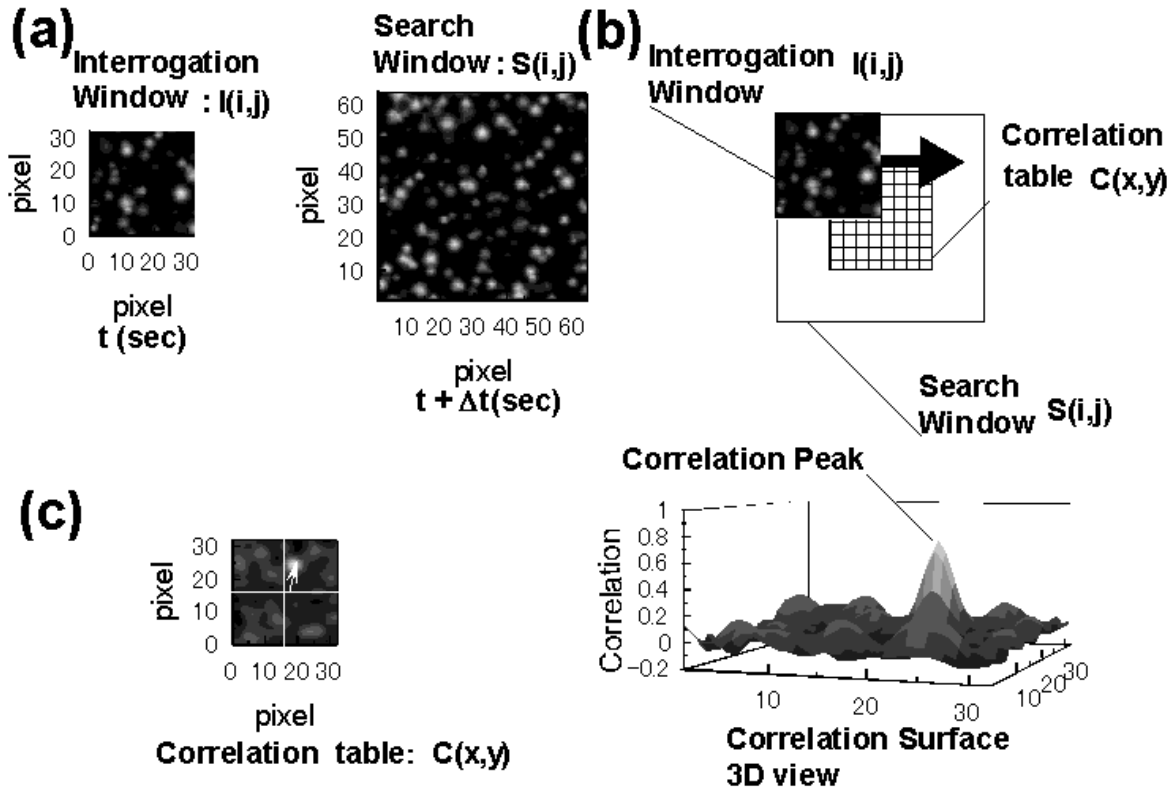

Figure 2.11: Cross correlation table of PIV

2.5.2 Post-processing of PIV data

Removal method of erroneous vectors

Erroneous vectors frequently occur in the vector field obtained from PIV measurement. The erroneous vector is defined as a different one in the length and direction compared with the surrounding vectors as shown in Fig. 2.12. The vector is caused by noises, for example, a background noise of captured image, an uneven intensity of laser light sheet and lack of tracer particles.

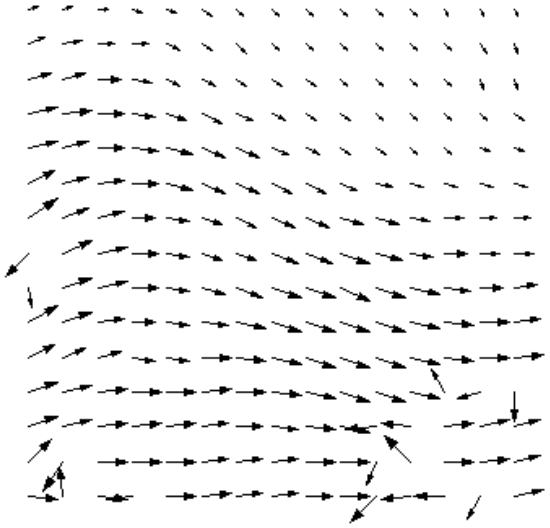

Figure 2.12: Vector field with erroneous vectors

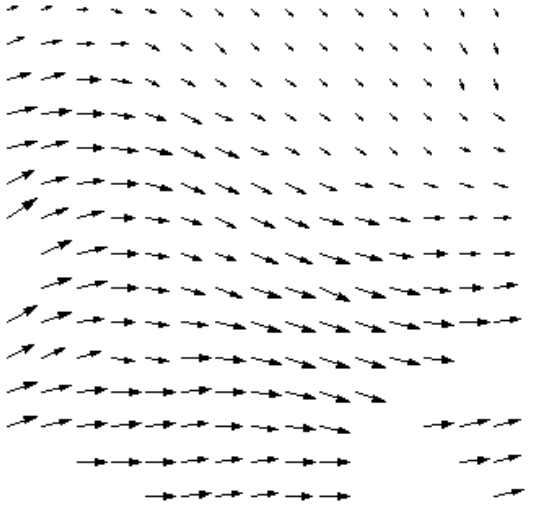

Figure 2.13: Vector field where erroneous vectors are removed

We adopted the removal method of erroneous vectors using Hopfield neural network [42] in the present study. The entire connection energy of the Hopfield neural network is represented as follows:

$$\mathrm{E} = \frac{1}{2}\sum_{i \neq j}(|\vec{v_i} - \vec{v_j}| - \frac{2}{3}\frac{|\vec{v_i}| + |\vec{v_j}|}{2})x_i x_j, \tag{2.12}$$

where i,j are the unit of the network, x is the output of the unit, $\vec{v}$ is the velocity vector and E is the energy function of the network. This energy function takes the minimum value by the iterative calculation of Eq.(2.12). In this procedure, the erroneous vectors are removed from vector field. Figure 2.13 shows the vector field after the removal of the erroneous vectors.

Interpolation method of removed vectors

In order to replace the removed vectors shown in Fig. 2.14 by interpolated vectors, we adopted the Laplace Equation Rearrangement (LER) [43] as the interpolation method. The interpolated velocities obtained by this rearrangement are written as follows:

$$u^*_{i,j} = \frac{\frac{u_{i+1,j}+u_{i-1,j}}{\Delta x^2} + \frac{u_{i,j+1}+u_{i,j-1}}{\Delta y^2}}{2(\frac{1}{\Delta x^2}+\frac{1}{\Delta y^2})} \tag{2.13}$$

$$v^*_{i,j} = \frac{\frac{v_{i+1,j}+v_{i-1,j}}{\Delta x^2} + \frac{v_{i,j+1}+v_{i,j-1}}{\Delta y^2}}{2(\frac{1}{\Delta x^2}+\frac{1}{\Delta y^2})}. \tag{2.14}$$

These interpolated vector $u^*_{i,j}$ and $v^*_{i,j}$ are obtained by the iterative calculation. Figure 2.15 shows the velocity field filled with the interpolated vectors.

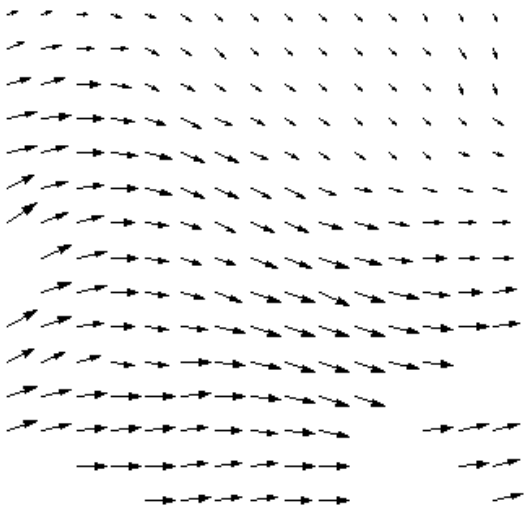

Figure 2.14: Vector field where erroneous vectors are removed

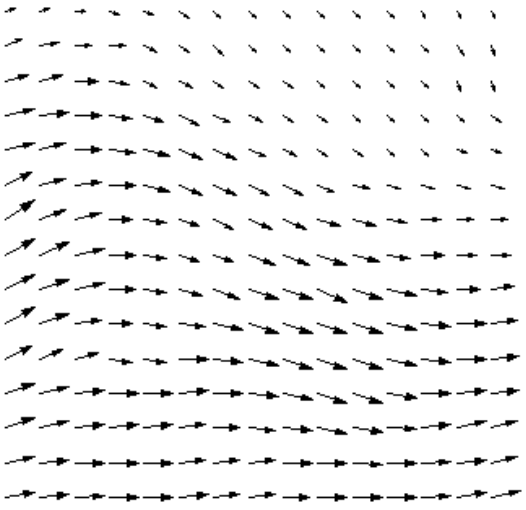

Figure 2.15: Vector field replaced by interpolated vectors

2.5.3 Iterative PIV (I-PIV)

Iterative PIV (hereafter we referred as I-PIV) [36, 37] using a gradient method [38, 40] has a hierarchical process in which the sampling grid is continually refined while the interrogation window size is reduced simultaneously. In general, the conventional PIV is fixed at a dynamic spatial range (an interrogation size). In such cases, the standard evaluation schemes cannot be used with small interrogation windows without losing the correlation signal due to the larger displacements. However, the dynamic spatial range can be increased effectively by the procedure. This is particularly useful in PIV recordings with both a high image density and a high dynamic range in the displacements. The hierarchical grid refinement algorithm is represented as follows:

Step 1: Calculate the cross-correlation.

Step 2: Remove the erroneous vectors using the neural network (see Sec.2.5.2) and interpolate using LER (see Sec.2.5.2). Since the recovered displacements serve only as estimates for the next higher resolution level, the erroneous vector detection can be more stringent than usual.

Step 3: Project the estimated displacement data onto the next higher resolution level. Use this displacement data to offset the interrogation windows with respect to each other.

Step 4: Increment the resolution level and repeat steps **1** through **4** until the standard image resolution is obtained.

Step 5: Finally perform an interrogation at the desired interrogation window size and calculate sub-pixel displacement using the gradient method (without neural network and LER).

In the final step, the window offset vectors have generally convergence $\pm$1pixel of the measured displacement. Therefore, this procedure can guarantee that the PIV image has been optimally evaluated.

In the case of the interrogation window with a size smaller than 32×32 pixels, the sub-pixel analysis (Gaussian peak fit) has the bias error that is called the peak-locking effect. The bias error resulted in the erroneous vectors. However, the gradient method can remove this error. In the final stage of Iterative PIV, the interrogation window size is small (8×8 pixels). Thus the gradient method is adopted in the final stage.

Figure 2.16 illustrates the image intensity in one dimension. It is assumed that the image intensity is exactly the same as that of the fluid motion and that of the particles that move from (x, y, t) to $(x + dx, y + dy, t + dt)$. Assuming that the change of the image pattern is smooth and that the luminance function $f(x, y, t)$ is expressed as a

Taylor series in time and space, it can be expressed in terms of a Lagrangian derivative,

$$\frac{\partial f}{\partial t} + u\frac{\partial f}{\partial x} + v\frac{\partial f}{\partial y} = \lim_{\Delta t \to 0} \frac{\Delta g(x, y, t, \Delta t)}{2\Delta t}. \tag{2.15}$$

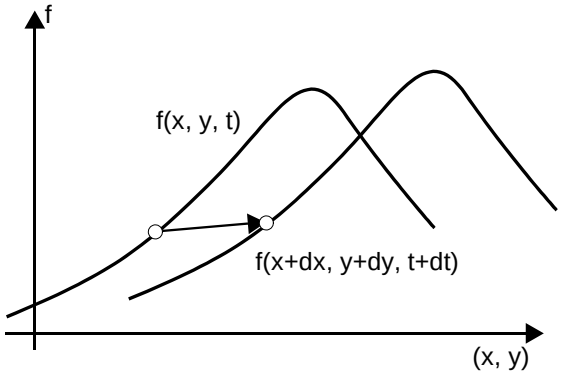

Figure 2.16: The principle of the gradient method

Assuming that the term in the right-hand side of Eq.(2.15) is white noise, the least squares method can be applied for the image in the interrogation window. If the velocities (u and v) are assumed to be constant in the window, the norm of the left-hand side terms $\sum_A \left\{ \frac{\partial f}{\partial t} + u\frac{\partial f}{\partial x} + v\frac{\partial f}{\partial y} \right\}^2$ is minimized. Then the velocity components (u, v) can be obtained by solving the following equations:

$$\begin{pmatrix} \sum_A \left(\frac{\partial f}{\partial x}\right)^2 & \sum_A \frac{\partial f}{\partial x}\frac{\partial f}{\partial y} \\ \sum_A \frac{\partial f}{\partial x}\frac{\partial f}{\partial y} & \sum_A \frac{\partial f}{\partial y}^2 \end{pmatrix} \begin{pmatrix} u \\ v \end{pmatrix} = - \begin{pmatrix} \sum_A \frac{\partial f}{\partial x}\frac{\partial f}{\partial t} \\ \sum_A \frac{\partial f}{\partial y}\frac{\partial f}{\partial t} \end{pmatrix}, \tag{2.16}$$

where A is the interrogation window.

Figure 2.17 shows Iterative PIV data [44] of Karman vortex street. The white squares in the lower left of each data set indicate the size of the interrogation window.

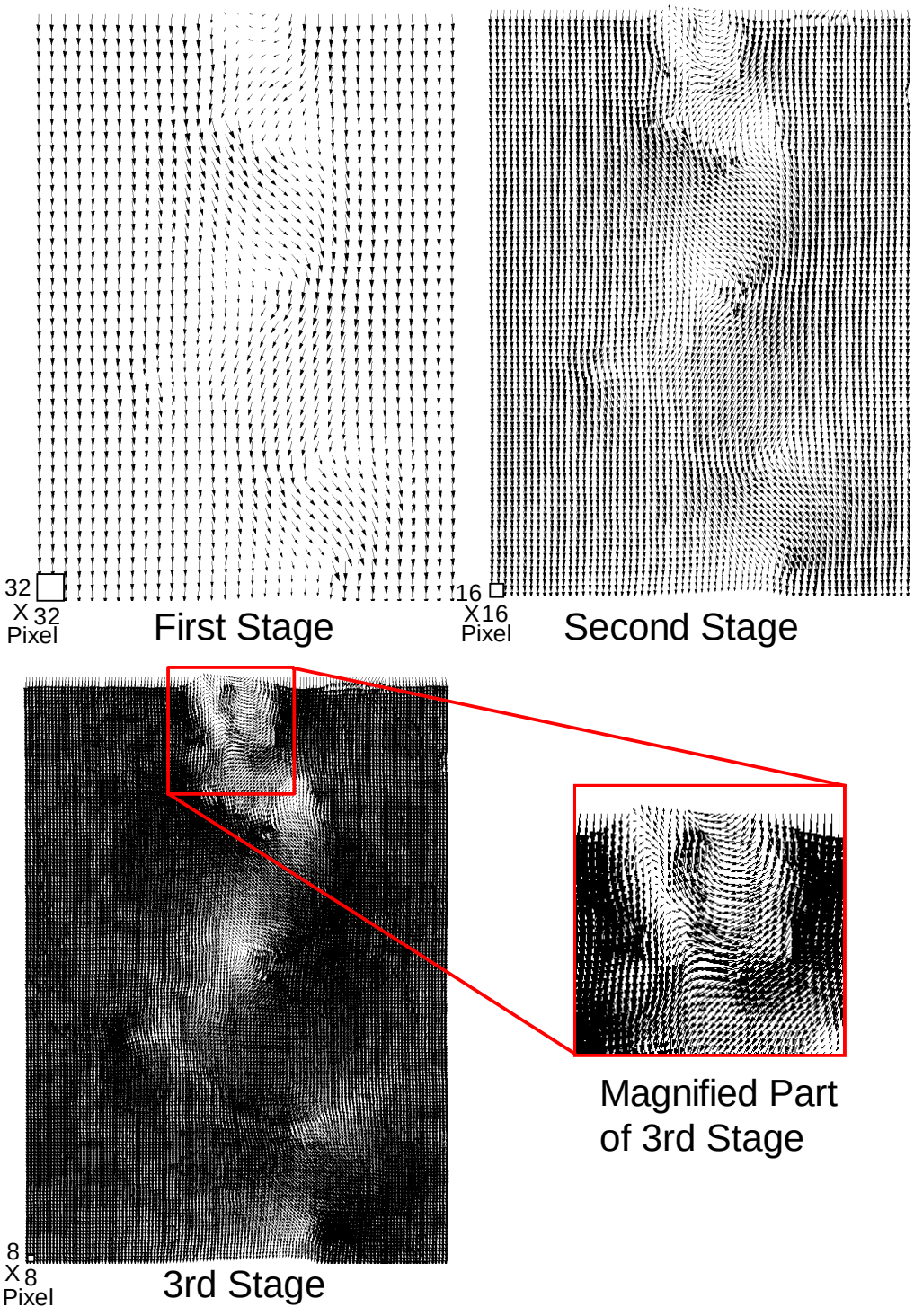

Figure 2.17: Results of Iterative PIV applied to Karman vortex [44]

2.5.4 Correlation error correction PIV (CEC-PIV)

Correlation error correction, henceforth referred to as CEC-PIV, proposed by Hart [41] is to amplify the signal of the correlation peak and eliminate anomalies peaks. Anomalies peaks occur from lack of tracer images, poor image quality, and unmatched tracer images within the correlated sample volume.

Assuming that the difference of each displacement of the correlation peak in surrounding correlation tables is enough small, the correlation table $\mathrm{C}_{i,j}(x,y)$ which has indiscernible correlation peaks is multiplied, element by element, by eight surrounding tables. The resulting correlation table $\mathrm{C}^*_{i,j}(x,y)$ is defined as follows:

$$\mathrm{C}^*_{i,j}(x,y) = \Pi_{k=i-1}^{k=i+1}\Pi_{l=j-1}^{l=j+1}\mathrm{C}_{k,l}(x,y). \tag{2.17}$$

Here, $\mathrm{C}_{i,j}(x,y)$ overlaps other tables by fifty percent. Correlation value that does not appear in each of multiplying tables is eliminated from the resulting table. Hence, CEC-PIV simultaneously amplifies a correlation peak and eliminates anomalies peaks.

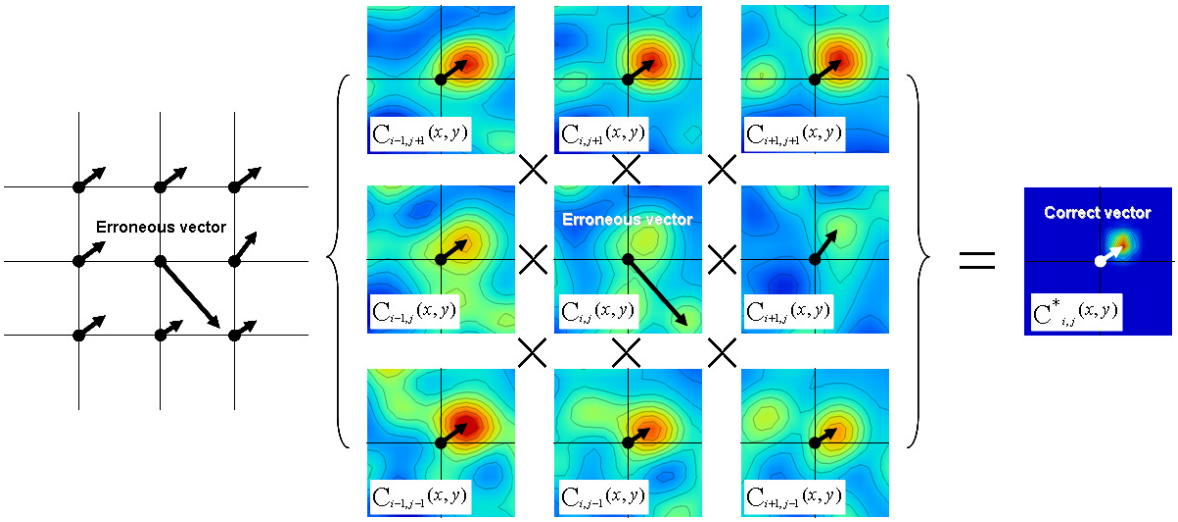

Figure 2.18: Correlation error correction

An example case of CEC-PIV is illustrated in Fig. 2.18. The correlation table $\mathrm{C}_{i,j}(x,y)$ in this example has several indiscernible peaks and the erroneous vector occurs from this correlation anomalies. On the other hand, surrounding tables almost have only one correlation peak. By applying CEC-PIV, the resulting table $\mathrm{C}^*_{i,j}(x,y)$ has very few correlation anomalies and has a very prominent correlation peak in the upper right-hand side.

The advantage of CEC-PIV is that signal-to-noise ratio grows much quicker. However, the major disadvantage is that, if a correlation table contains several zero signals

around the correlation peak, then the resulting table eliminates the peak. Although this is a rare case, post processing (the removal method and the interpolation method) described in Sec. 2.5.2 is applied to PIV data derived from CEC-PIV.

2.5.5 Specification of PIV algorithms

Specification of PIV algorithms is presented as schematic image (Fig. 2.19). The main difference among three algorithms is that CEC described in Sec. 2.5.4 is used or not used. On the other hand, common algorithms are the removal method described in Sec. 2.5.2 and the interpolation method described in Sec. 2.5.2.

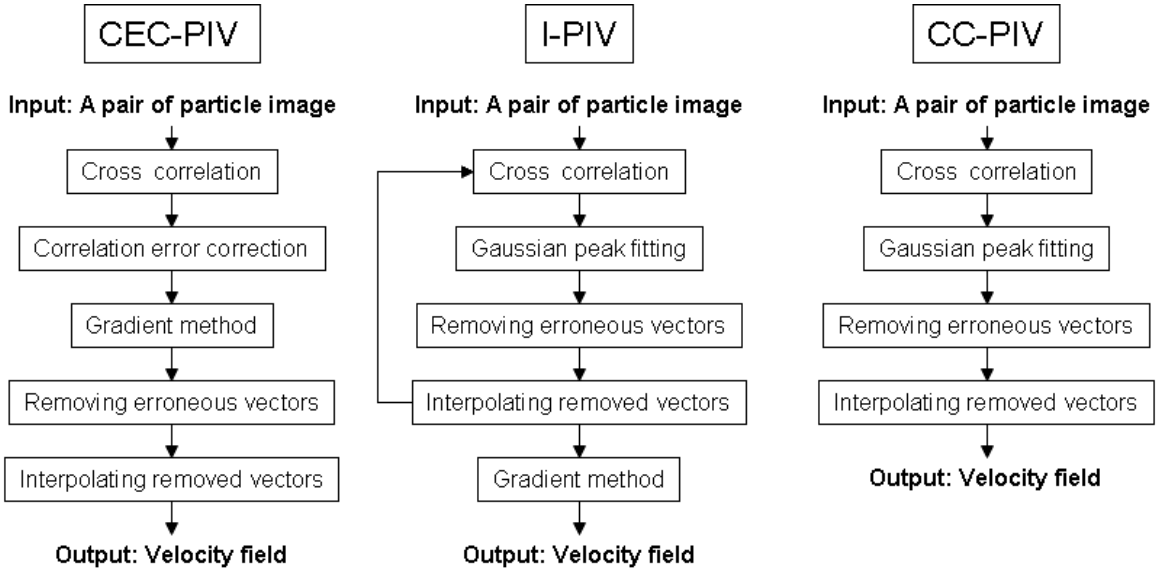

Figure 2.19: Three PIV algorithms

Here, PIV parameters are as follows: number of vectors, 113×113; grid size, 4 pixel; search window size, 32×32 pixels; interrogation window size, 16×16 pixels; correlation table, 17×17 pixels and gradient method's correlation table, 7×7 pixels. In I-PIV algorithm, the interrogation window size changes from 33×33 pixels (search window size: 64×64 pixels, interrogation window size: 32×32 pixels) to 17×17 pixels (search window size: 32×32 pixels, interrogation window size: 16×16 pixels).

2.5.6 Artificial particle image for PIV algorithm evaluations

In order to evaluate the performance of PIV algorithms (CC-PIV, I-PIV and CEC-PIV) described in Sec.2.5.5, a pair of artificial particle image frames with a size of 512×512 pixels representing Burgers vortex is generated by randomly distributing a particle image in the frame.

The individual particle is defined as the kernel matrix having a Gaussian intensity distribution. The light intensity distribution $I(x, y)$ of the particle image is expressed by the following equation [35]:

$$I(x, y) = I_0 \exp\left(-\frac{x^2 + y^2}{2\sigma^2}\right), \tag{2.18}$$

where I_0 denotes light intensity and σ for standard deviation of a Gaussian intensity distribution.

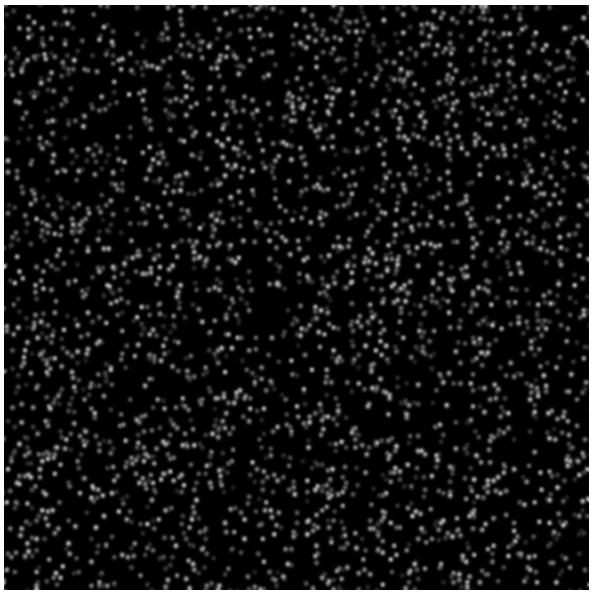

Figure 2.20: Particle image frame with the light intensity of Gaussian distribution

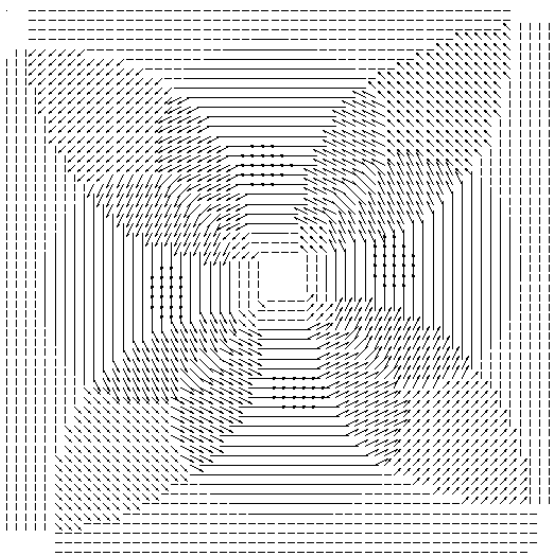

Figure 2.21: Burgers vortex with an integer velocity distribution

Figure 2.20 shows a particle image frame generated by Eq. (2.18). In this study, the value of I_0 is chosen randomly in the range $51 < I_0 < 255$, and $\sigma = 2.0$ is adopted. The positions of the particle in the second frame are obtained from the Burgers vortex velocity field (Eq.(1.1) and Eq.(1.2)). Flow parameters Γ, α and l_b are matched with experimental conditions. Fig. 2.21 shows the Burgers vortex which has the integer velocity distribution to avoid the sub-pixel error caused by the discretized particle image position. Thus the velocity field is not smooth and the each center of the particle is positioned at the integer value.

2.5.7 Comparison of PIV algorithms

In order to estimate the influence of lack of tracer particle in the interrogation window 17×17 pixels, a pair of artificial particle images is generated by stepwise changing the number of the particle images by 0.5 in the range from 0.5 to 5.0.

Figure 2.22(a)-(d) shows comparison between each PIV algorithm. By comparing the exact vector field of Burgers vortex with the resulting vectors field from the three algorithms, it is found that these resulting vector fields are substantially influenced by the number of the particle image.

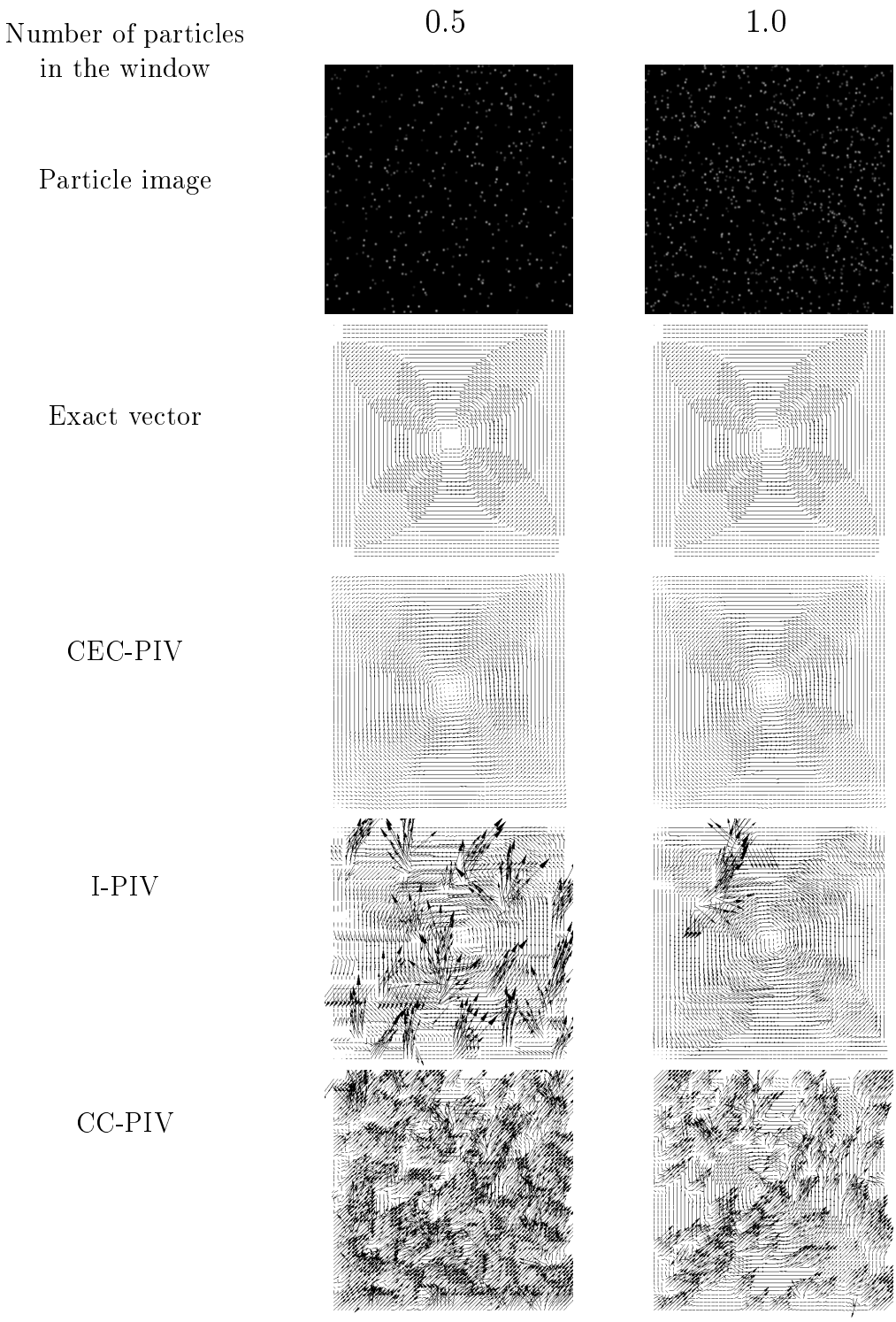

Figure 2.22**(a)**: Comparison between each PIV algorithm

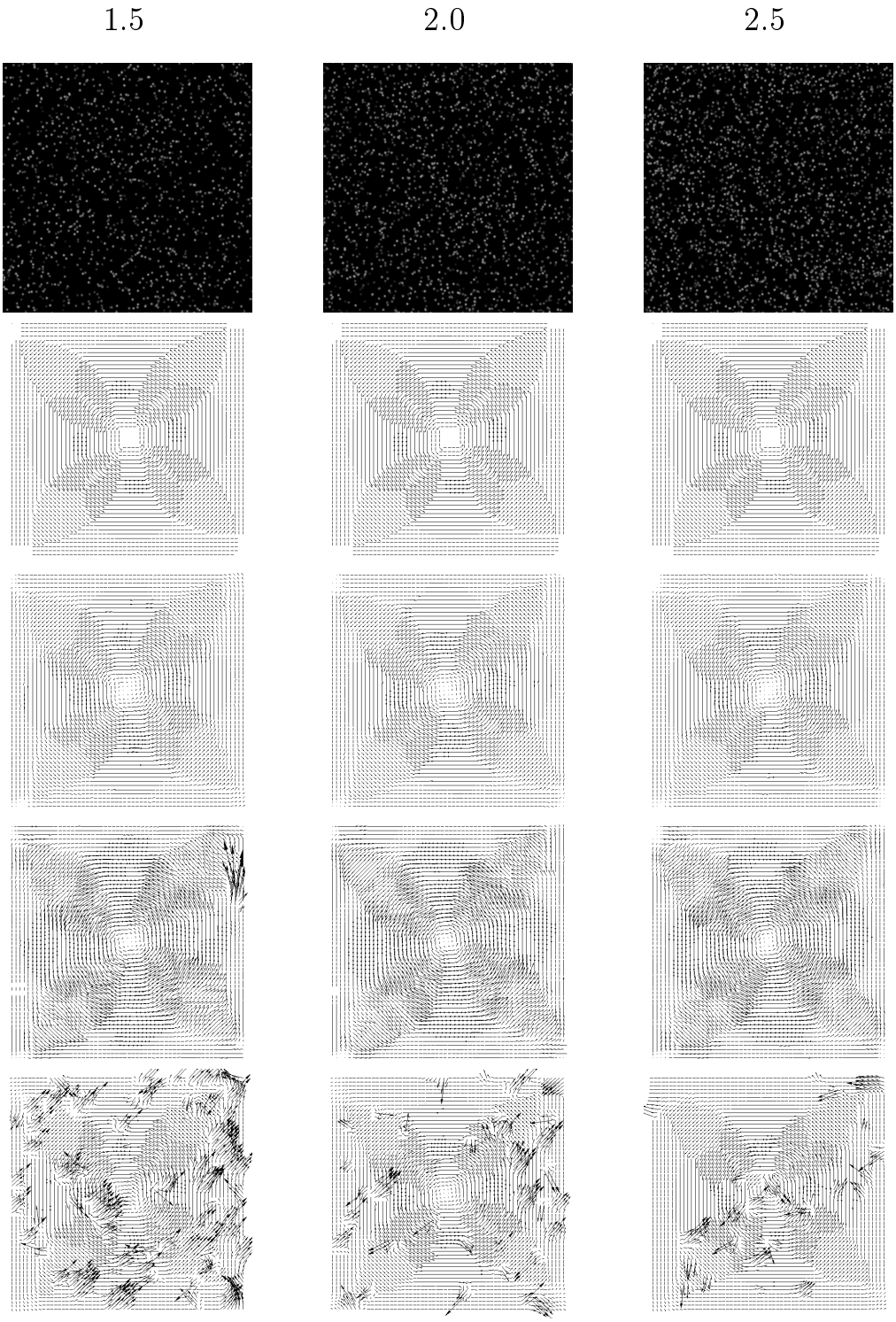

Figure 2.22**(b)**: Comparison between each PIV algorithm

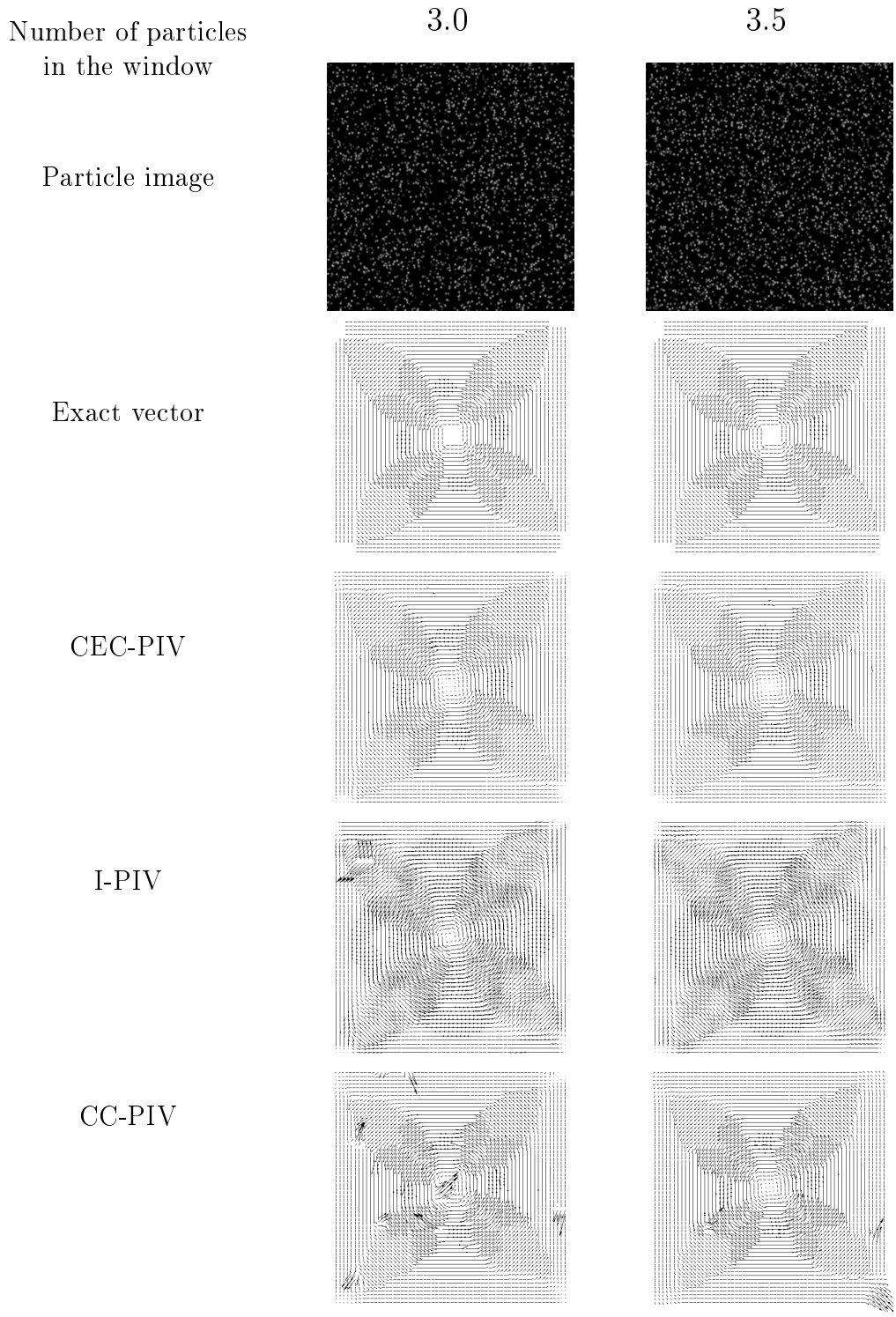

Figure 2.22(**c**): Comparison between each PIV algorithm

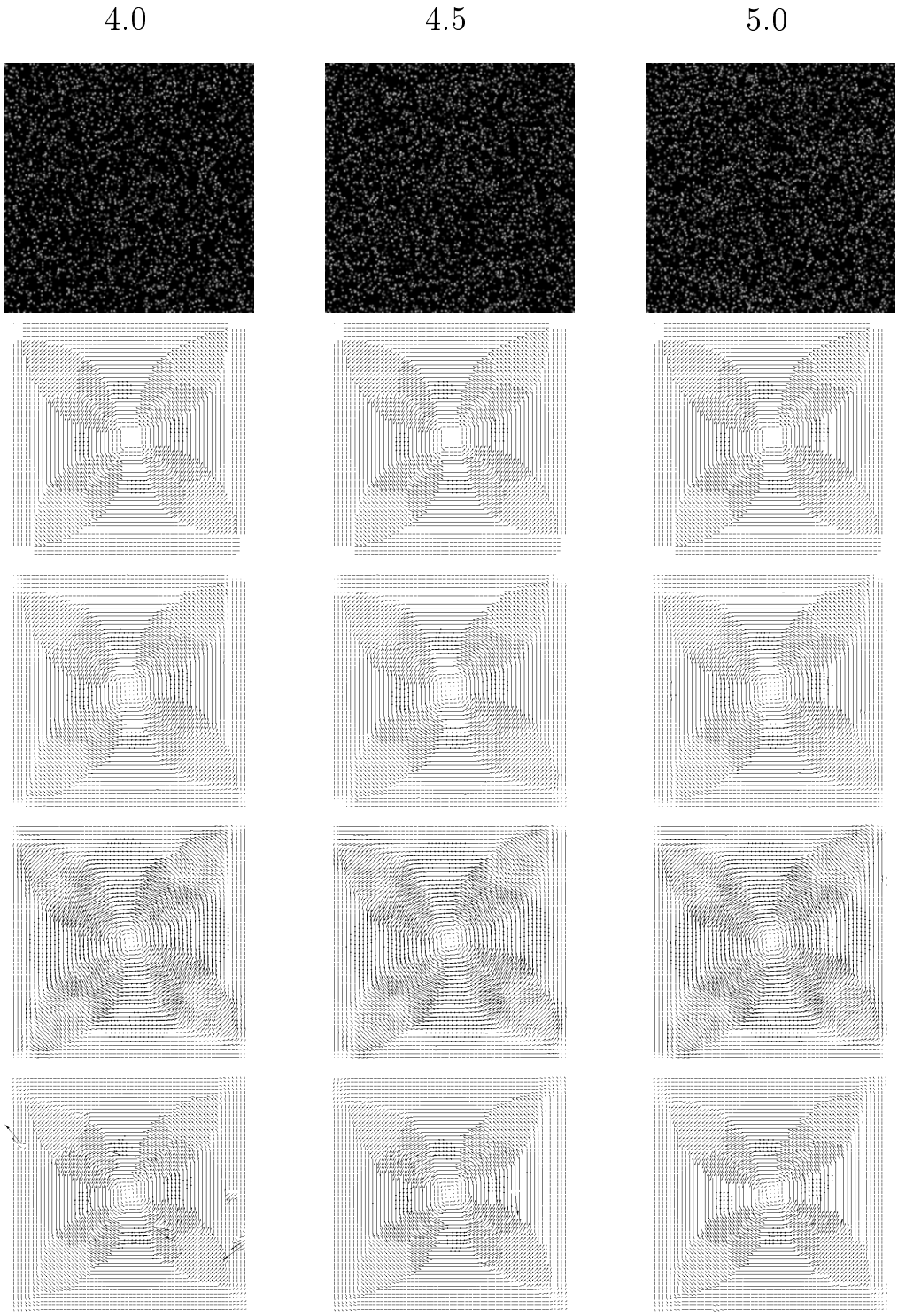

Figure 2.22**(d)**: Comparison between each PIV algorithm

2.5.8 Comparison of accuracy among PIV algorithms

In three algorithms, resulting vector fields are calculated in ten different number of tracer particles in the interrogation window from 0.5 to 5 by 0.5. The resulting vector of PIV and the exact vector of Burgers vortex are denoted as $\mathbf{u_{piv}}$ and $\mathbf{u_{exact}}$, respectively. The measurement error Error (pixel) is defined as

$$\text{Error} = \sqrt{\frac{\sum_{i=1}^{N}(\mathbf{u_{piv}} - \mathbf{u_{exact}})^{\mathbf{2}}}{N}} \tag{2.19}$$

Figure 2.23 shows that the change of measurement error on three algorithms is small when the number of tracer particle is larger than 3.0. CEC-PIV and I-PIV almost achieve the so-called "sub-pixel accuracy", except for the number which is smaller than 1.0 on I-PIV. On the other hand, even if the number is increased, CC-PIV does not achieve sub-pixel accuracy. It is found that the measurement accuracy of CEC-PIV is robust to the number of the tracer particles in the interrogation window on the measurement accuracy.

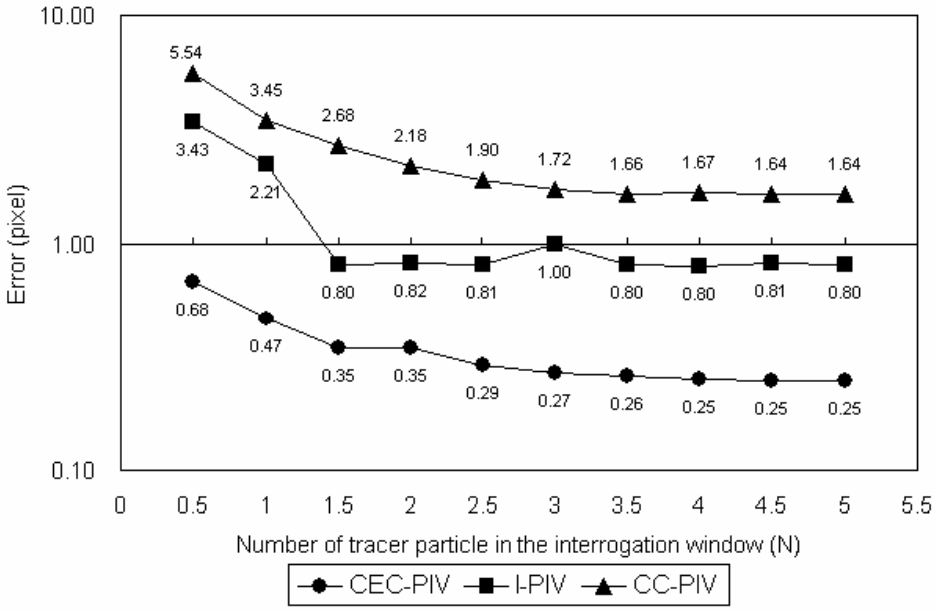

Figure 2.23: Influence of particle number in the interrogation window on the error

2.5.9 Comparison of calculation time among PIV algorithms

The calculation time among three algorithms is presented in Fig. 2.24. The calculation system for PIV is mainly composed of a desktop PC with CPU 2.80 GHz Pentium 4 and 1GB RAM. All algorithms are compiled by the Intel ®C++ Compiler Standard Edition for Windows ver. 4.09.

The calculation time of I-PIV and CC-PIV is almost independent of the number of particle in the interrogation window. In case of I-PIV, it is because the erroneous vectors are detected and are interpolated each twice and in case of CC-PIV, it is because a certain erroneous vectors always occur. Meanwhile, the calculation time of CEC-PIV sharply decreases when the number of particle reaches to 3.0. This is because that the measurement accuracy is stable and erroneous vectors is decreased when the number reaches to 3.0 as described in Sec. 2.5.8.

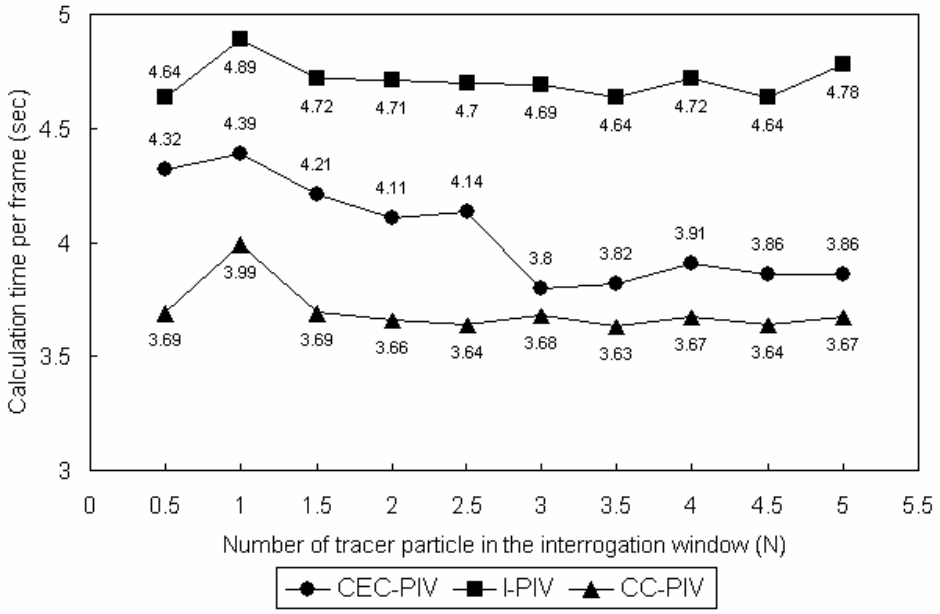

Figure 2.24: Influence of particle number in the interrogation window on the calculation time

2.5.10 An optimal PIV algorithm

The trade-off analysis between the measurement error and the calculation time is performed to select an optimal PIV for this study. The error and the calculation time are plotted in Fig. 2.25. These averaged and standard deviation values are obtained from Fig. 2.23 and Fig. 2.24 at each number of particles.

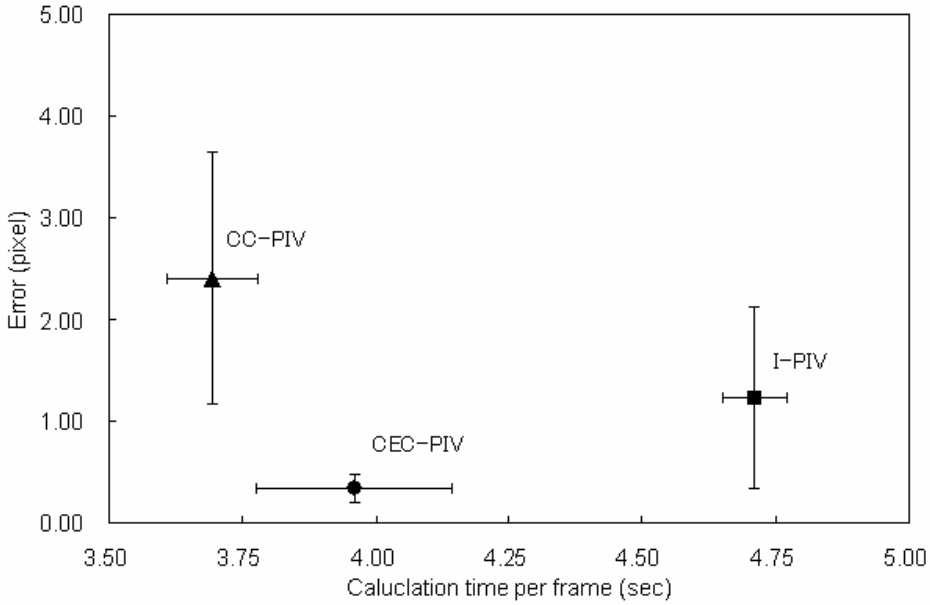

Figure 2.25: Trade-off between calculation time and error

As for the calculation time, CC-PIV is best, followed by CEC-PIV and I-PIV. However the measurement error indicates that CEC-PIV is the best algorithm, followed by I-PIV and CC-PIV. From these results, we give priority to the measurement accuracy and concluded that CEC-PIV is the optimal PIV for the present study.

2.6 Visualization of the influence of a particle on the vortex

In this section, we introduce visualization methods for the effects of a settling particle on a Burgers vortex. Quasi-three-dimensional vorticity field is visualized by tomographic scan of two-dimensional vorticity distribution, and three component velocity of a settling particle is reconstructed by using the data obtained from PIV measurement and a particle velocimetry system. In order to display vorticity and superficial divergence in the same plane, BVD distribution is proposed.

2.6.1 Visualization of quasi-three-dimensional vorticity field

To visualize the three-dimensional vortex structure, the time series data set of vorticity distributions is stacked like a tomographic scan. In the previous study, Taylor's frozen field hypothesis [45] is applied to quasi-three-dimensional vortex structure of a plane jet [28]. This hypothesis is based on the assumptions that the shed vortices remain unchanged as the vortices pass downstream, or, formally, that $\partial/\partial t = -U\partial/\partial z$ and $1 \gg U/U_c$. Here U_c is the convective velocity of a spatial structure and U is the local mean velocity. In the present study, U and U_c are replaced by a mean flow velocity $\overline{U}_z$ and particle velocity V_{zexp}, respectively, and the condition of $1 \gg \overline{U}_z/V_{zexp}$ is satisfied as shown in Table. 2.3. The flow around a particle could be convected with the particle velocity. However, the wake vortices far from a particle could be convected with the mean flow velocity. So time axis, in the present study, is used in place of z axis of quasi-three dimensional vorticity field.

To construct a three-component velocity of a particle on the observation plane, an rθ-component velocity obtained from PIV measurement and a z-component velocity measured by the particle velocimetry system described in Sec. 2.2.3 are used. An rθ-velocity field around a particle is obtained by PIV measurement as shown in Fig. 2.26 (a). The solid line indicates solid-fluid boundary. The enclosed area stands for a particle positioned on the observation plane. The position is manually detected from the frame in which a particle appears. An rθ-component velocity of a particle shown in Fig. 2.26 (b) is constructed as an ensemble average of inner vectors shown in Fig. 2.26 (a). Here, the image of a particle is treated as a tracer particle, and inner vectors are obtained by PIV. Although the particle velocimetry system is installed above the observation plane, z-component velocity of a particle at the observation area is given by the particle velocimetry system, because z-component velocity measured by the particle velocimetry system reaches a terminal velocity as described in Sec. 2.3.2. Figure 2.27 shows the quasi-three dimensional vorticity field and a three component velocity of Particle B.

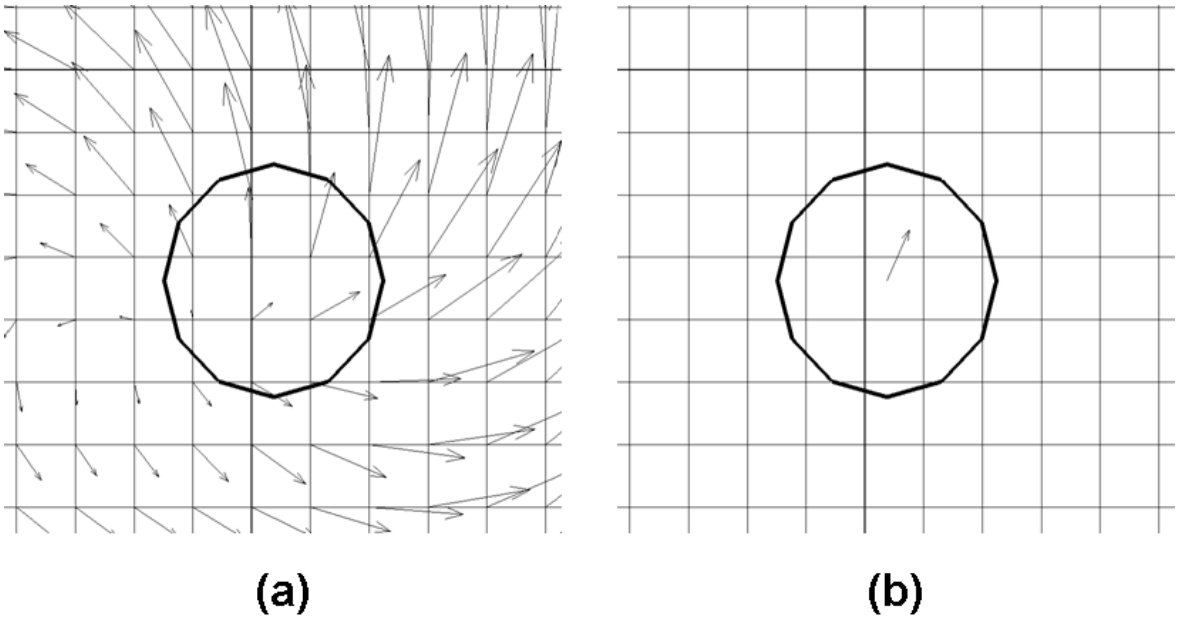

Figure 2.26: Reconstruction of an rθ-component velocity of a particle

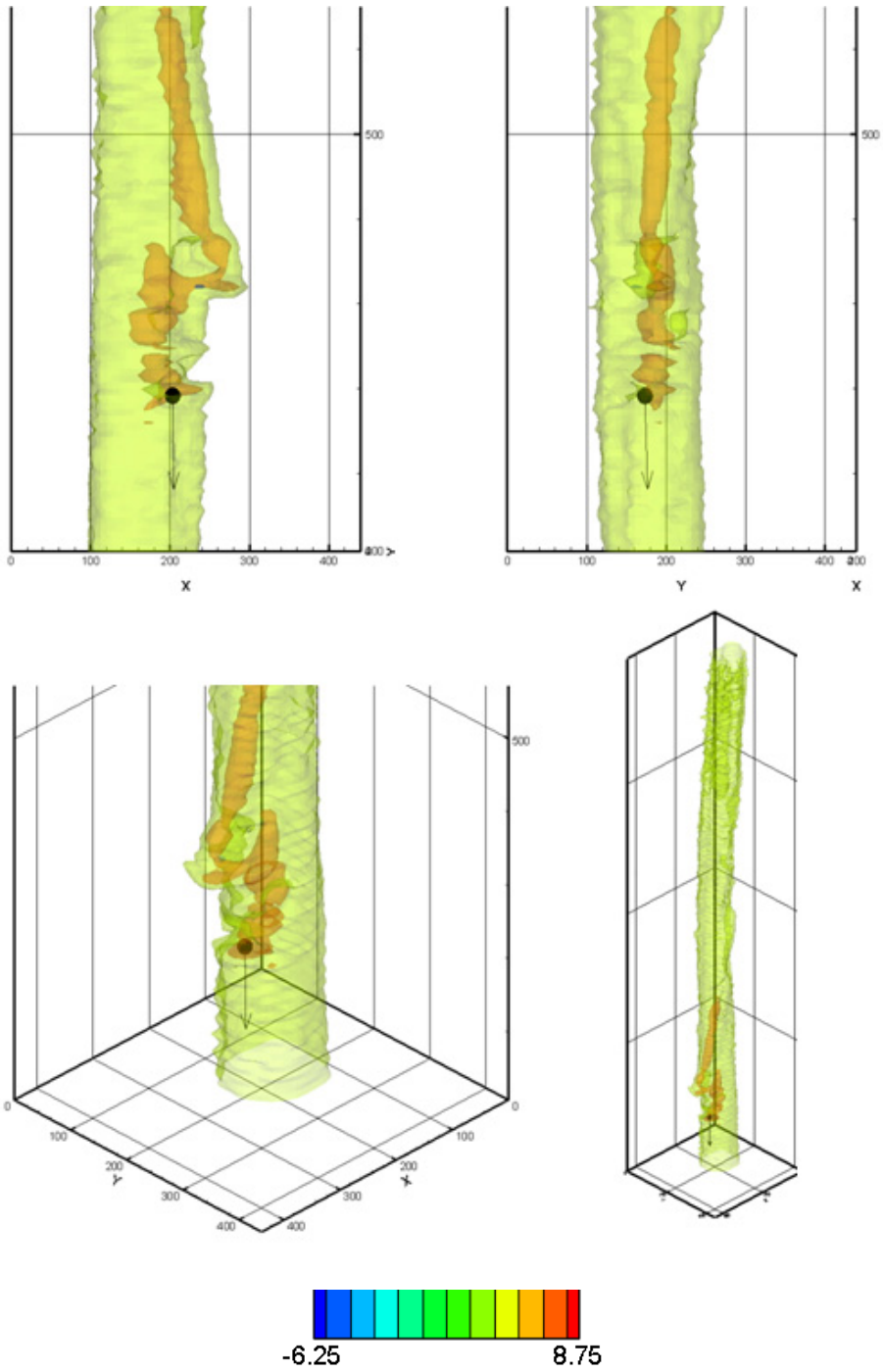

Figure 2.27: Quasi-three dimensional vorticity field $\omega_z(r, \theta, t)$ and a three component velocity of Particle B

2.6.2 Visualization of balance between vorticity and divergence

In the present study, the flow field perpendicular to the rotational axis of the vortex is measured as the observation plane. The divergent and convergent flow are induced in the flow and wake regions of the particle as shown in Fig. 2.28. In cylindrical coordinate (r, θ, z), the superficial divergence of the flow on $r\theta$-plane, $\mathrm{div}_{r\theta}\boldsymbol{u}$, is defined by

$$\mathrm{div}_{r\theta}\boldsymbol{u} = \frac{1}{r}\frac{\partial(ru_r)}{\partial r} + \frac{1}{r}\frac{\partial u_\theta}{\partial \theta}. \tag{2.20}$$

When the flow is incompressible, using the continuity equation, $\mathrm{div}_{r\theta}\boldsymbol{u}$ is given as follows

$$\mathrm{div}_{r\theta}\boldsymbol{u} = -\frac{\partial u_z}{\partial z}. \tag{2.21}$$

Superficial divergent flow ($\mathrm{div}_{r\theta}\boldsymbol{u} > 0$) is induced by the particle approaching the plane ($\partial u_z/\partial z < 0$), and superficial convergent flow ($\mathrm{div}_{r\theta}\boldsymbol{u} < 0$) is induced by the particle leaving $r\theta$ plane ($\partial u_z/\partial z > 0$), as shown in Fig. 2.28.

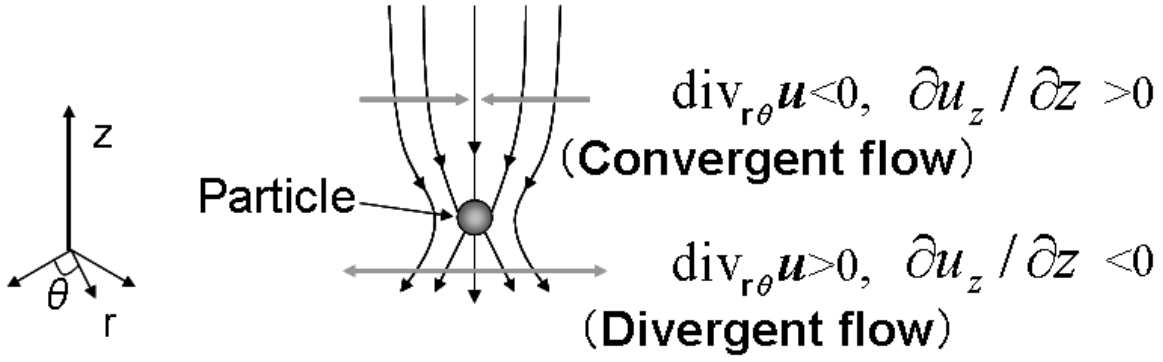

Figure 2.28: Influence of a settling particle on the flow

Figures 2.29 (a) and (b) show the vorticity field $\omega_z(r,\theta)$ and the superficial divergence field $\mathrm{div}_{r\theta}\boldsymbol{u}$, when Particle B has just passed through the observation plane (more detail in Sec. 3.3). The correspondence of position between the vorticity and the divergence is incomprehensible as shown in Figs. 2.29 (a) and (b). To illustrate the position correspondence between them clearly, we propose BVD (Balance between Vorticity and Divergence) defined by

$$\mathrm{BVD}(r,\theta) \quad = \quad |\omega_z(r,\theta)| - |(\mathrm{div}_{r\theta}\boldsymbol{u})(r,\theta)|. \tag{2.22}$$

Figure 2.29 (c) shows $\mathrm{BVD}(r,\theta)$ field.

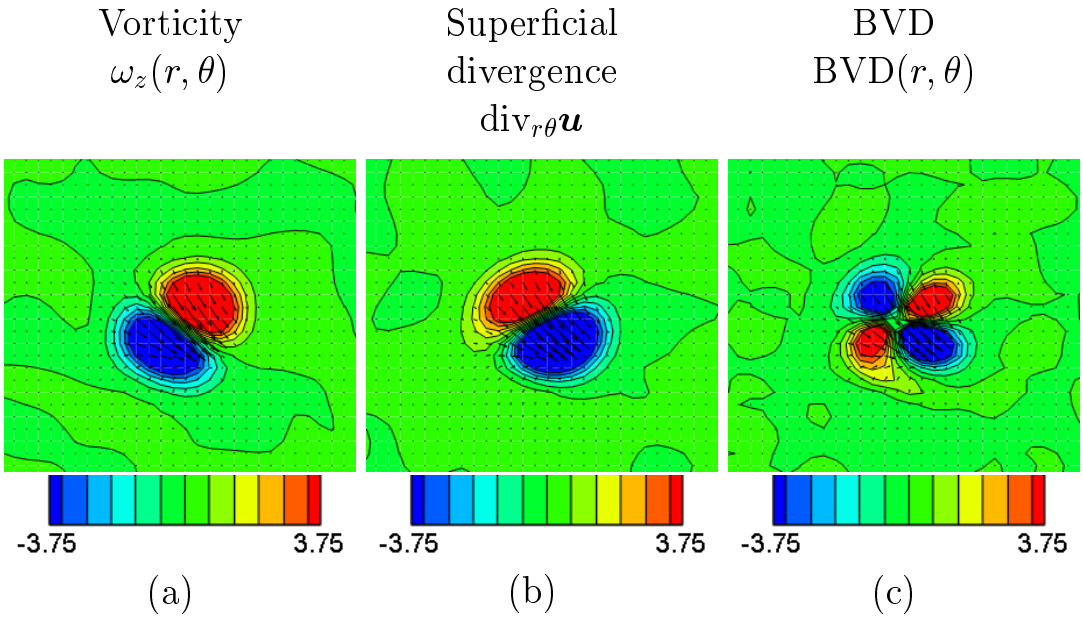

Figure 2.29: Distributions of the vorticity, the superficial divergence and BVD

2.7 Conclusions

In this chapter, the experimental setup, conditions, Particle Image Velocimetry (PIV) techniques and the visualization techniques for the examination of the influence of a settling particle on a Burgers vortex are presented.

In the flow system, the fluid goes through the wide cross section of the upperpart of the water tank to the narrow cross section of the orifice, the stagnation point flow occurs, and a vortex tube is generated by the rotating fan. It is found that the circumferential velocity and vorticity distributions of the generated vortex well agree with the analytical solutions of the Burgers vortex. Thus, the developed flow system enables the generation of a Burgers vortex. Additionally, the particle dispenser and the particle velocimetry system are newly developed. The particle dispenser enables a settling particle to be released reproducibly. The vertical component of the particle velocity at the measuring cross section is measured by the particle velocimetry system.

To observe the interaction between a Burgers vortex and vortices shed from a settling particle, experiments are carried out under the large values of particle Reynolds number. The correspondence of the generated vortex and the vortex of an isotropic turbulent flow is clarified by using the length-scale relation between an isotropic turbulent flow and a Burgers vortex. Four kinds of particles are used in the present study. The particles have the same diameter, but different densities. The resultant particle Reynolds numbers at the measuring section are ranged from 1430 to 3880, hence, all particles shed vortices. By analyzing the Stokes number concerning the traceability to the vortex motion, it is found that the particle motion is in an equilibrium state with respect to the vortex motion.

The measurement accuracy of PIV measurement depends on the number of tracer particles in the interrogation window. Because a tracer particle is heavier than water, the number of particles decreases over time. In order to select an algorithm robust to decrease of tracer particles, three representative PIV algorithms (CC-PIV, I-PIV and CEC-PIV) are examined. From test results by using artificial images, it is found that CEC-PIV algorithm is most robust to the decrease. We conclude that CEC-PIV is the optimal PIV for the present study.

Two kinds of visualization methods for the flow field are introduced. A quasi-three-dimensional vorticity field is constructed by stacking two-dimensional vorticity fields. Three velocity components of a settling particle is reconstructed by combining the velocity components of an $r\theta$-plane obtained from PIV data with z component of the velocity detected by the particle velocimetry system. To make clear the effect of the three-dimensional flow structure on the two-dimensional flow measured on the plane, the superficial divergence on the measured plane is defined. BVD distribution is introduced to present vorticity and superficial divergence field in the same plane.

Chapter 3

Burgers vortex and flow around a settling particle

3.1 Introduction

In this chapter, as the basis to consider the nonlinear interaction between a particle and a Burgers vortex, the flow fields around an isolated particle and an isolated Burgers vortex measured by the PIV are presented.

3.2 Time change of the intensity of Burgers vortex

In the present study, we focus on the time series of the circulation of Burgers vortex to see the influence of a settling particle on the vortex intensity. To express the intensity of the vortex, we define a circulation of Burgers vortex as follows:

$$\Gamma(t) = 2\pi \int_0^{1.12 l_b} \omega_z(t, r) r dr, \tag{3.1}$$

where $w_z(r, \theta)$ is vorticity, the time range is corresponding to the forced vortex region described in Sec. 2.4, and the center of the vortex is defined as a point where the absolute value of velocity takes a minimum value.

We examined the time change of the circulation of the Burgers vortex without particle settling. Figure 3.1 indicates an example of the obtained time series of the circulation and the quasi-three-dimensional presentation of the iso-surface of vorticity ($\omega_z = 6.25$). The circulation is non-dimensionalized by the time averaged circulation $\overline{\Gamma_0}$ (0.0 - 4.0 sec with 500 frames). The standard deviation calculated with four samples is 0.023.

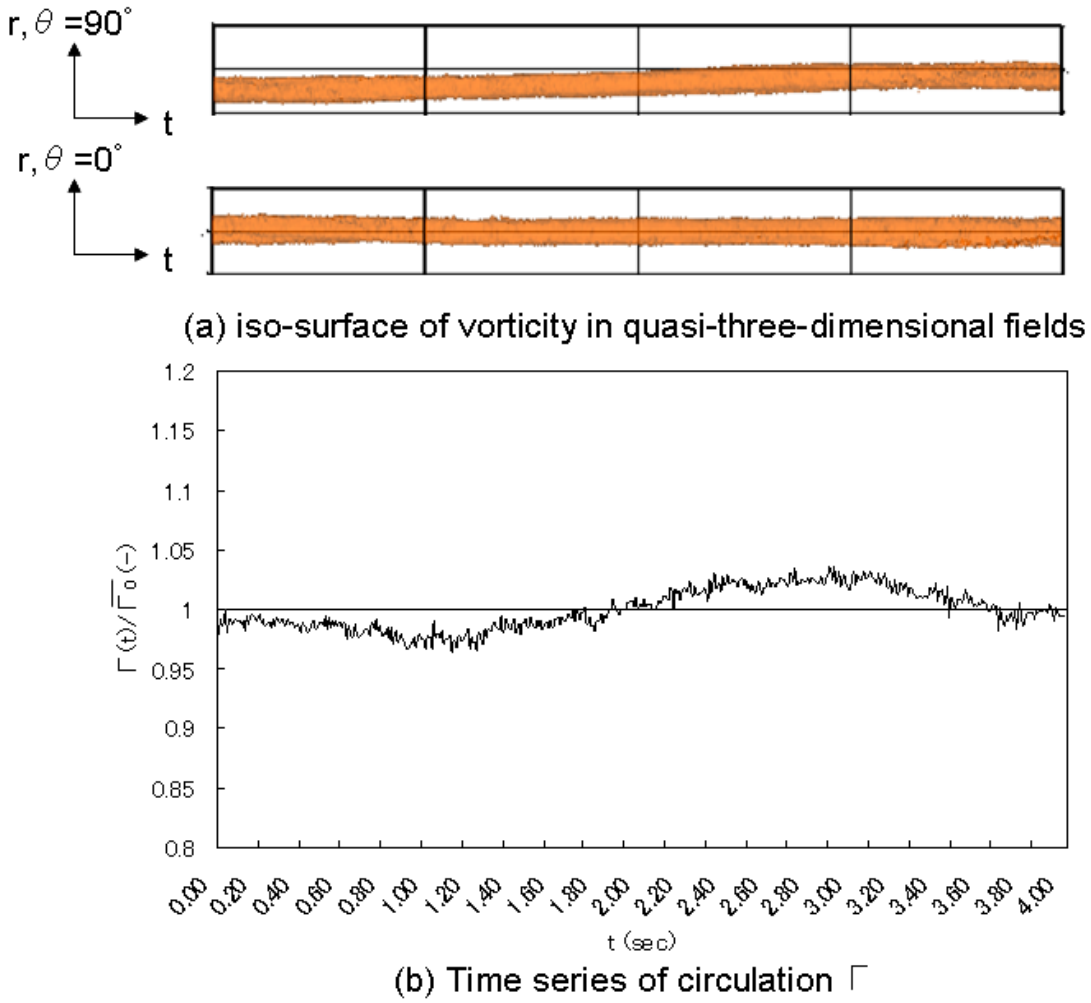

Figure 3.1: Time series of the circulation of Burgers vortex and iso-surface of vorticity magnitude ($\omega_z = 6.25$)

3.3 Vortex-wake structure generated by a particle settling in stationary fluid

To clarify the nature of the wake vortices shed from a settling particle, we performed PIV measurement of the flow around a particle settling in the stationary fluid.

Figures 3.2-3.5 show vortex-wake structures of Particle A, B, C and D, visualized by iso-surface of vorticity in the quasi-three dimensional vorticity field $\omega_z(r, \theta, t)$ described

in Sec. 2.6.1. These figures indicate vortex structures are getting more complicated as particle Reynolds number increases. Figure 3.6 shows comparison of the vorticity distribution $\omega_z(r,\theta)$ of Particle A,B,C and D at different times indicated by solid lines ((a)-(e)) in Fig. 3.2-3.5. In these distributions at different times, several pairs of the vorticities which have positive and negative value are observed.

A pair of vorticities is clearly observed in the case of Particle A as shown at times (c), (d) and (e) in Fig. 3.7 and Fig. 3.8(2). The pair of vorticities is generated between the pair of the superficial divergences having positive and negative value as shown in BVD distributions of (c), (d) and (e). Thus, it is considered that the vorticity near the superficial flow is generated by the particle.

To observe the time evolution of a pair of vorticities and divergences, the maximum and minimum values of vorticity and superficial divergence ($\omega_{z\ max}$, $\omega_{z\ min}$, $\mathrm{div}_{r\theta}\boldsymbol{u}_{max}$ and $\mathrm{div}_{r\theta}\boldsymbol{u}_{min}$) are represented as feature of a pair of the vorticities and the superficial divergences. The time change of these values is plotted in Figs 3.9-3.12 at each Particle A, B, C and D. Here, we set the origin of time when a particle passes through the observation area, and these plots are averaged over five samples. It is found that these pairs of the vorticities and superficial divergences have almost same value at each time in the observation time.

To evaluate the magnitude relation of the vorticity between the Burgers vortex and the shed vortices, we introduce the time averaged maximum vorticity ω_{Bmax} of the Burgers vortex and the time averaged maximum vorticity $\omega_{Pmax} = (\omega_{z\,max} + |\omega_{z\,min}|)/2$ of Particle A,B,C and D. $\overline{\omega_{Pmax}}$ is time averaged from $t = 0$ sec to $t = 1.8$ sec. $\overline{\omega_{Bmax}}$ is time averaged in 4.0 secs, obtained from four samples described in Sec. 3.2. Figure 3.13 shows the ratio of $\overline{\omega_{Pmax}}$ to $\overline{\omega_{Bmax}}$ for each Particle A,B,C and D. This figure indicates that the maximum value of vorticity of Burgers vortex is larger than that of the particles.

3.4 Conclusion

To express the intensity of the vortex, we define a circulation of Burgers vortex. The time change of the circulation of the Burgers vortex without particle settling is observed. The standard deviation of the time change is 0.023.

In stationary fluid, the pair of vorticities is generated between the pair of the superficial divergences having positive and negative value as shown in BVD distributions. Pairs of the vorticities and superficial divergences have almost same value at each time in the observation time.

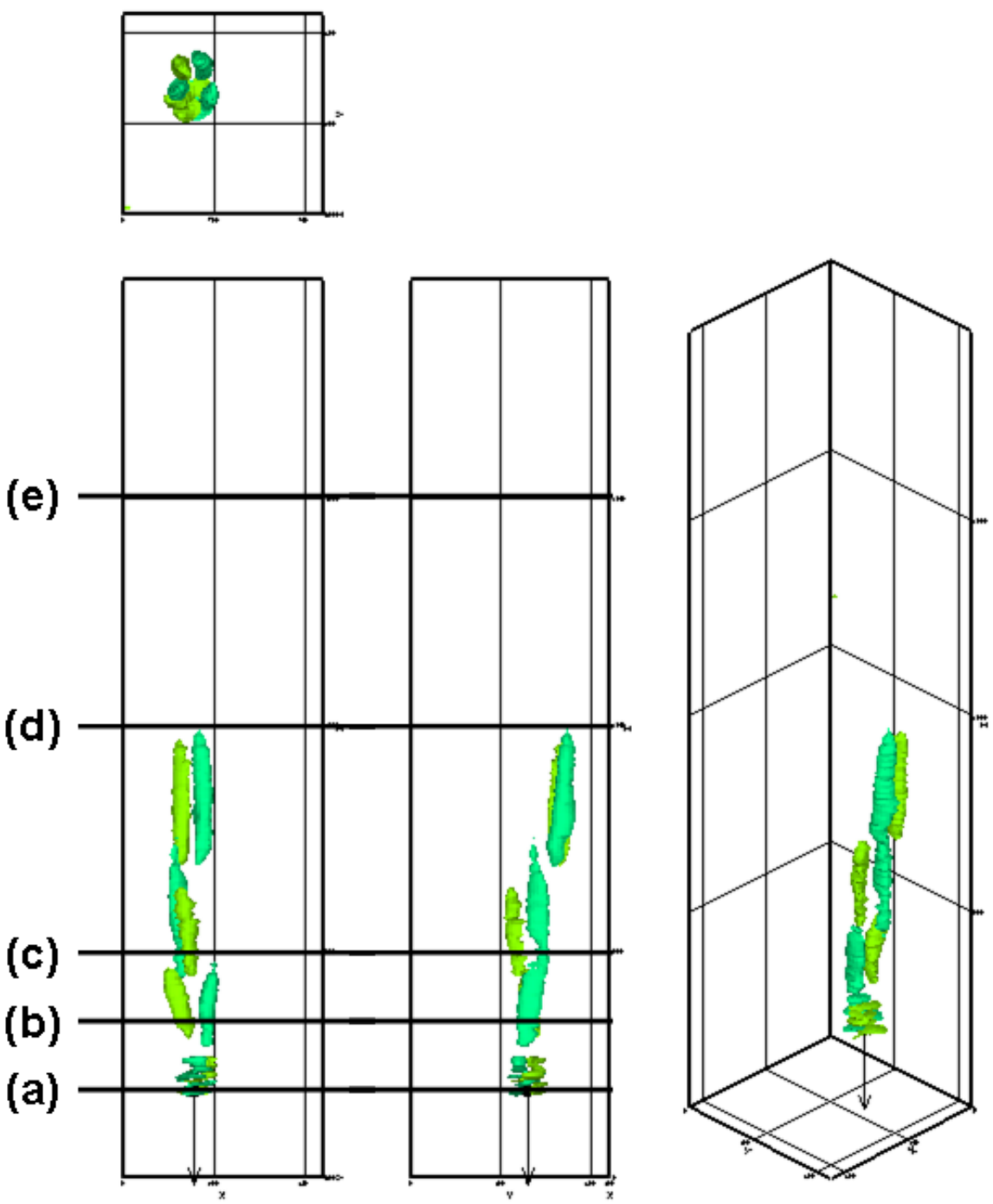

Figure 3.2: Particle A ($Re_p = 1430$): Vortex wake structure generated by a settling particle (iso-surface of vorticity magnitude ($\omega_z = 1.25, -1.25$))

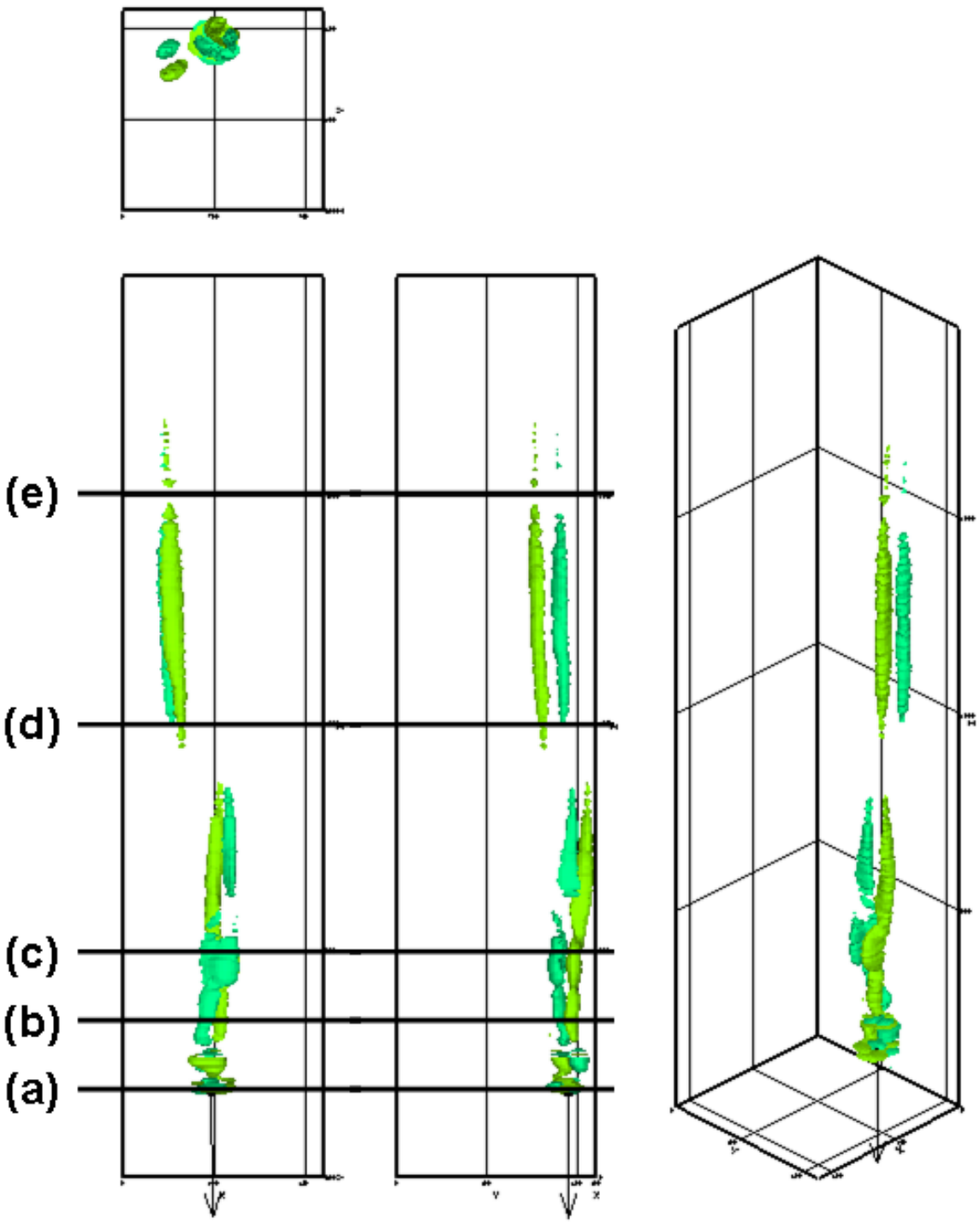

Figure 3.3: Particle B ($Re_p = 1940$): Vortex wake structure generated by a settling particle (iso-surface of vorticity magnitude ($\omega_z = 1.25, -1.25$))

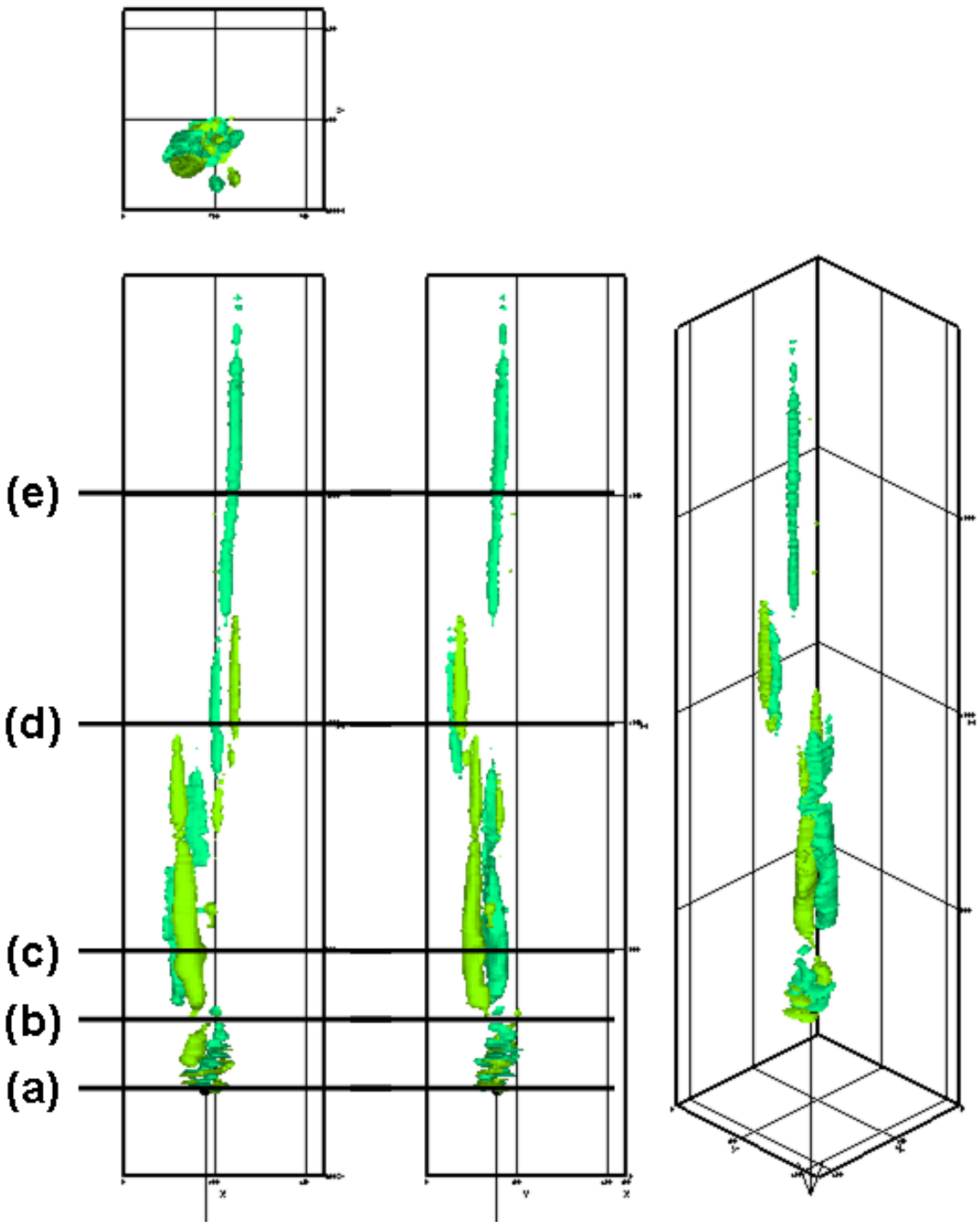

Figure 3.4: Particle C ($Re_p = 3200$): Vortex wake structure generated by a settling particle (iso-surface of vorticity magnitude ($\omega_z = 1.25, -1.25$))

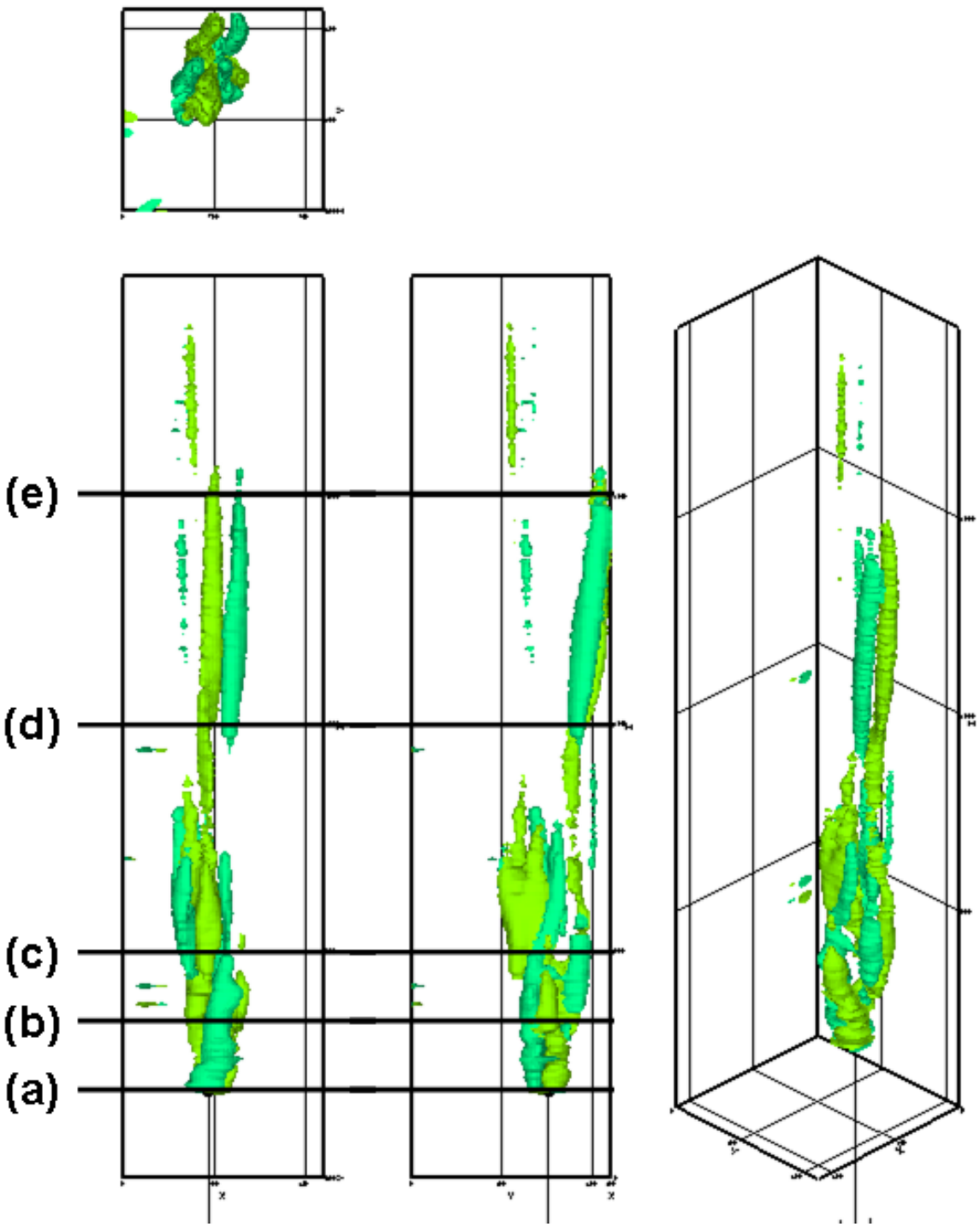

Figure 3.5: Particle D ($Re_p = 3880$): Vortex wake structure generated by a settling particle (iso-surface of vorticity magnitude ($\omega_z = 1.25, -1.25$))

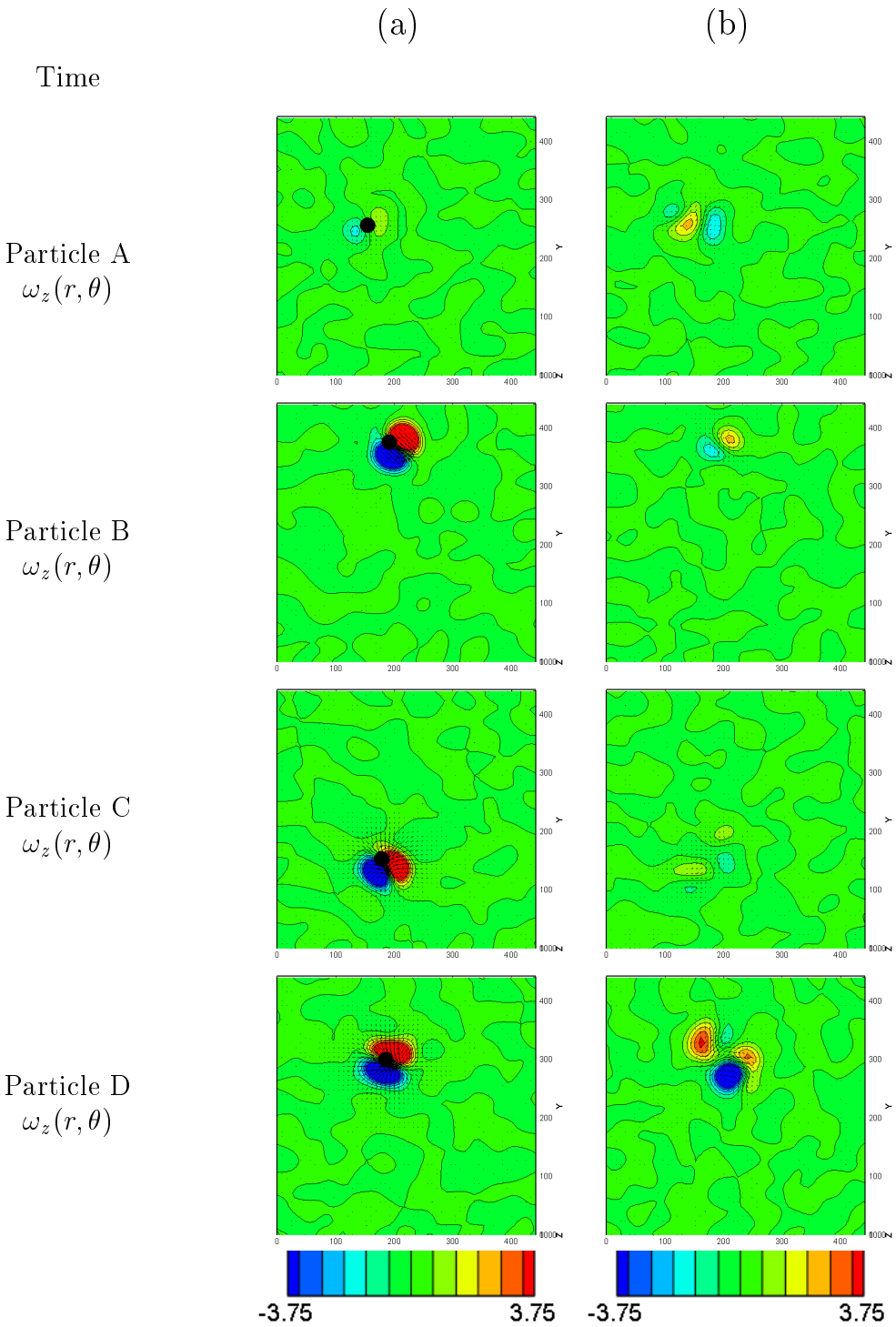

Figure 3.6**(1)**: Comparison of $\omega_z(r,\theta)$ of Particle A,B,C and D at different times

(c) (d) (e)

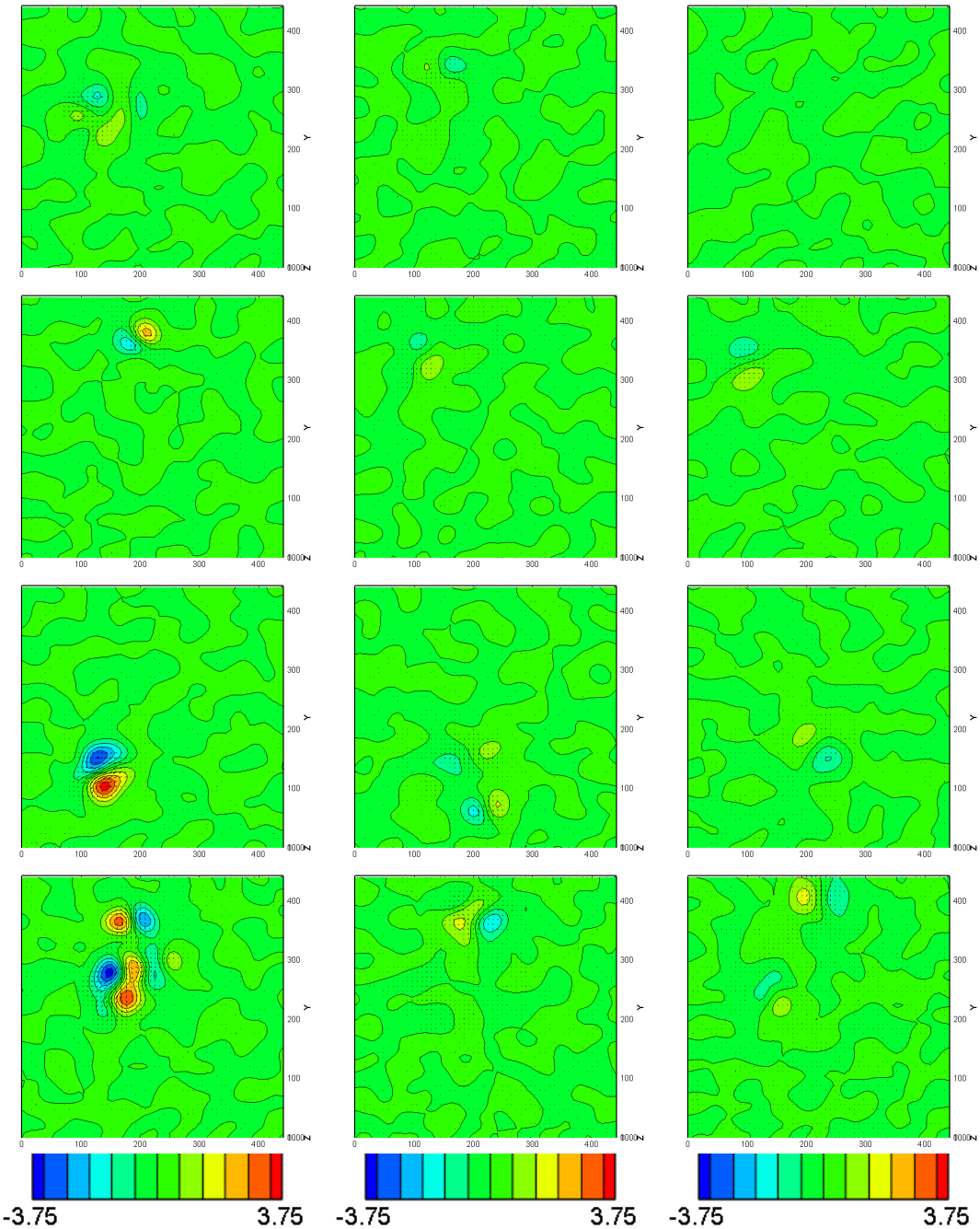

Figure 3.6(**2**): Comparison of $\omega_z(r,\theta)$ of Particle A,B,C and D at different times

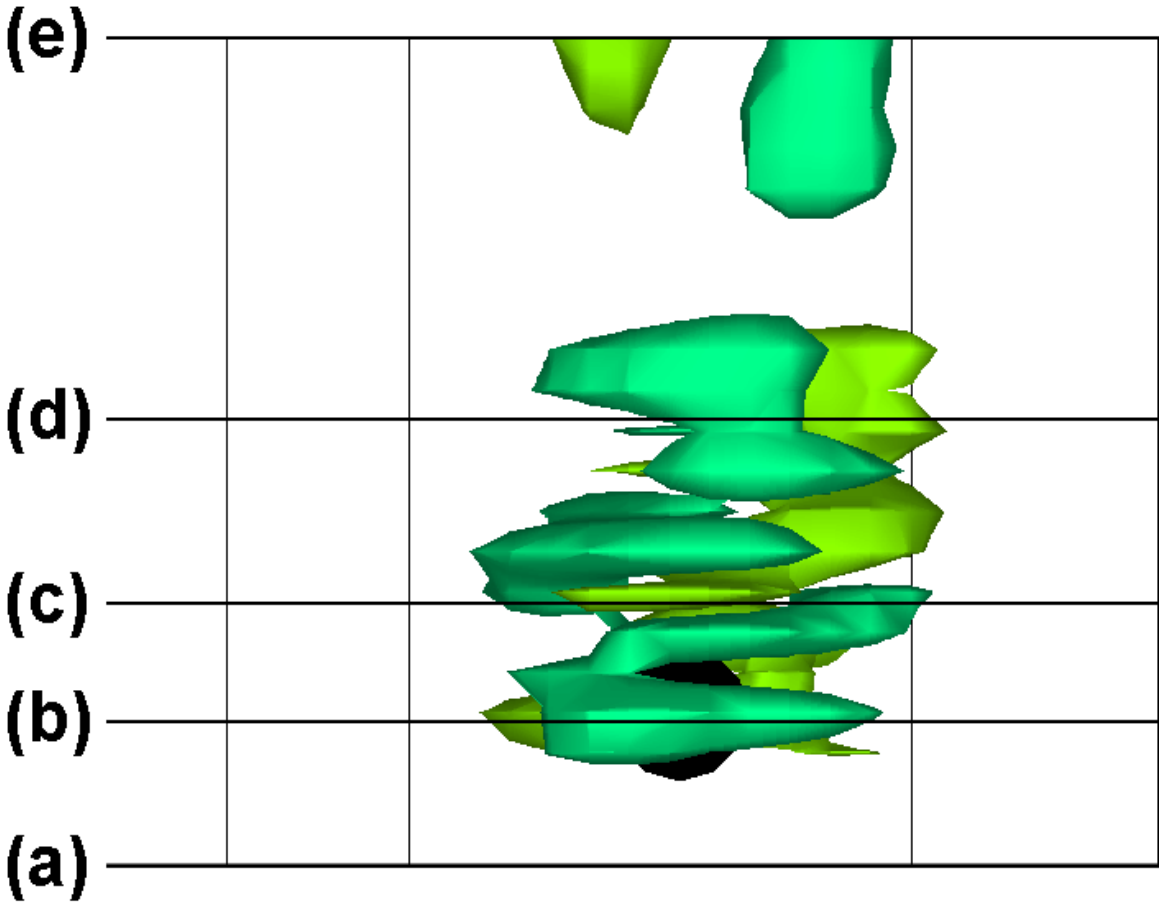

Figure 3.7: Particle A ($Re_p = 1430$): Magnified image of vortex wake structure generated by a settling particle (iso-surface of vorticity magnitude ($\omega_z = 1.25, -1.25$))

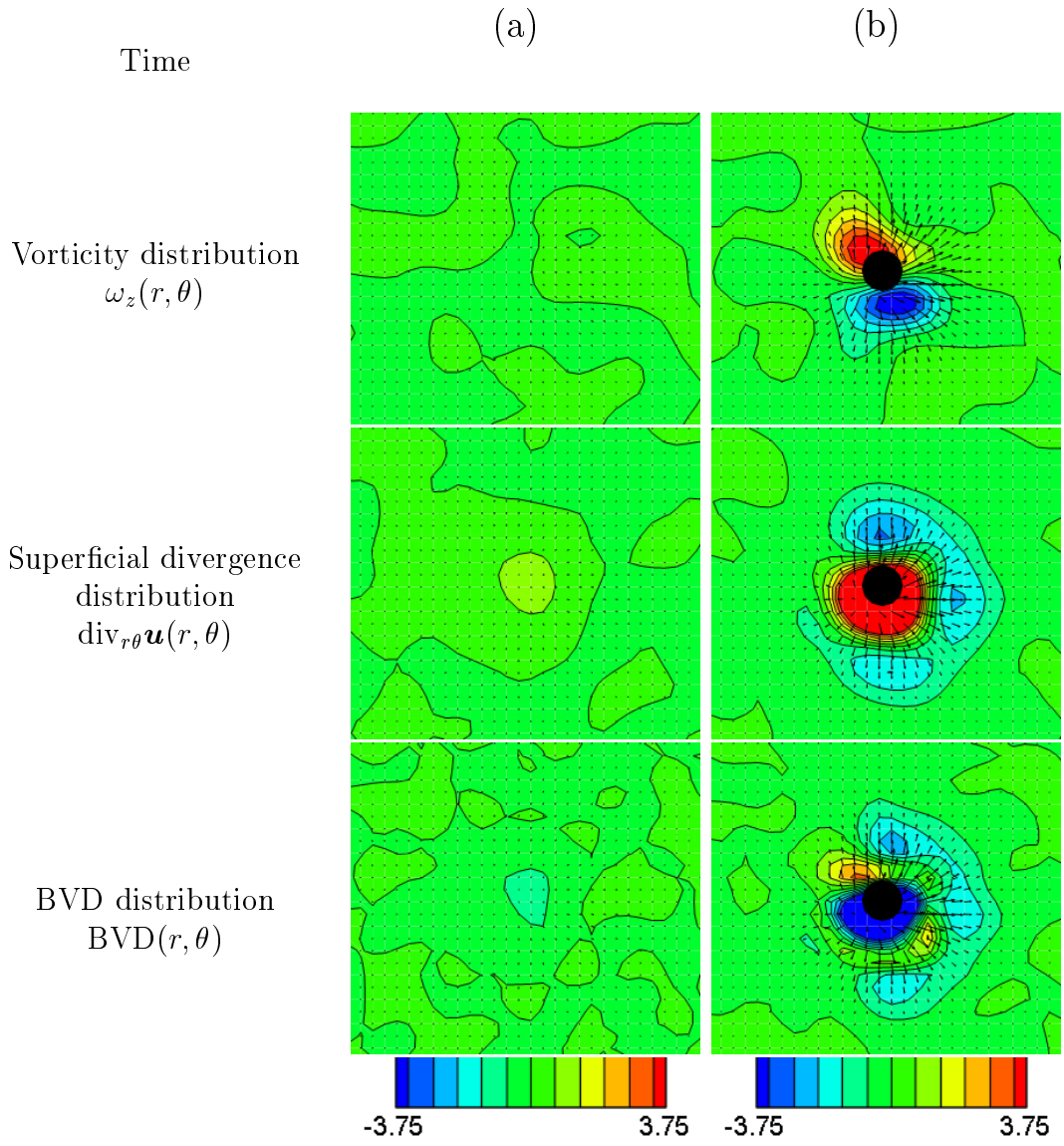

Figure 3.8**(1)**:Particle A: Comparison of $\omega_z(r,\theta)$, $\mathrm{div}_{r\theta}\boldsymbol{u}(r,\theta)$ and $\mathrm{BVD}(r,\theta)$ at different times

(c) (d) (e)

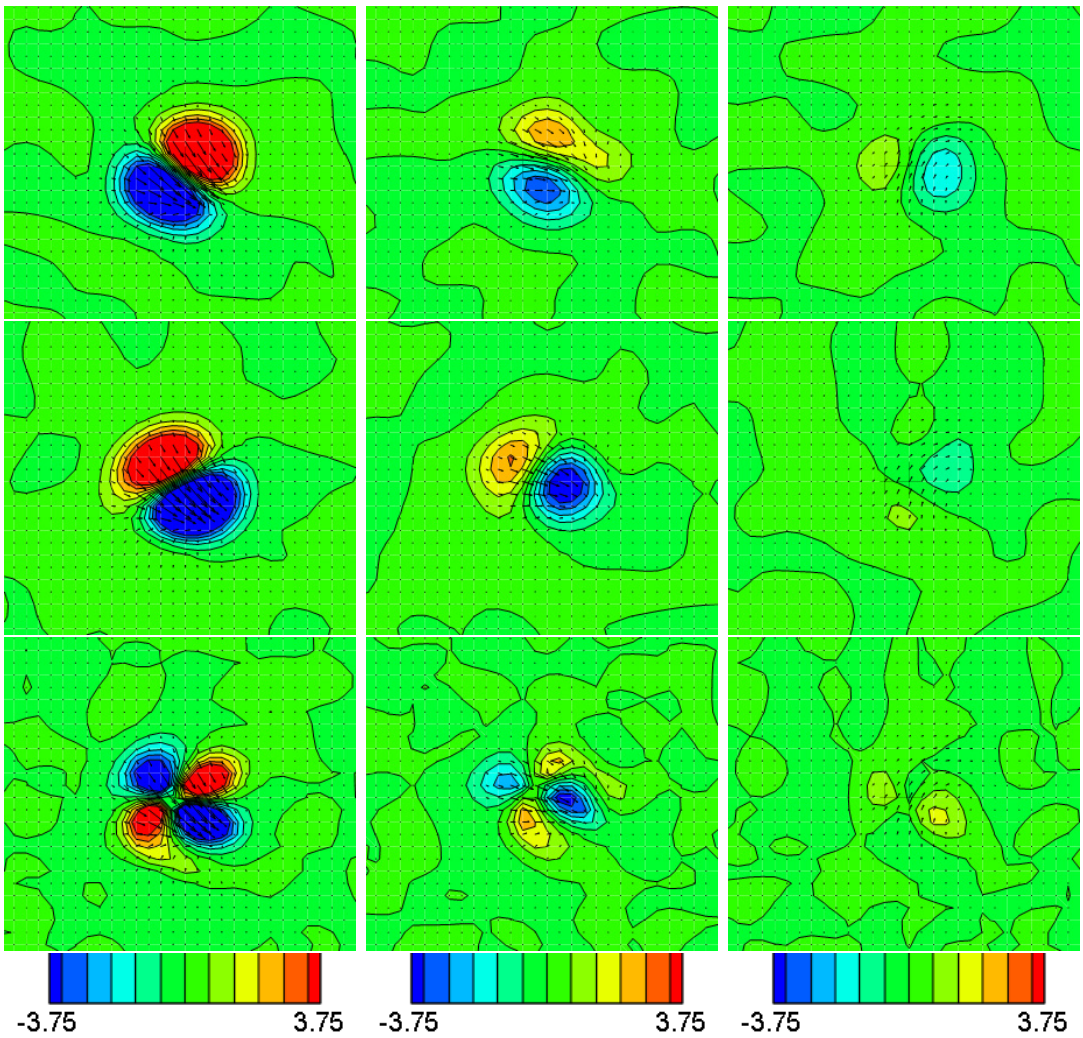

Figure 3.8**(2)**:Particle A: Comparison of $\omega_z(r,\theta)$, $\mathrm{div}_{r\theta}\boldsymbol{u}(r,\theta)$ and $\mathrm{BVD}(r,\theta)$ at different times

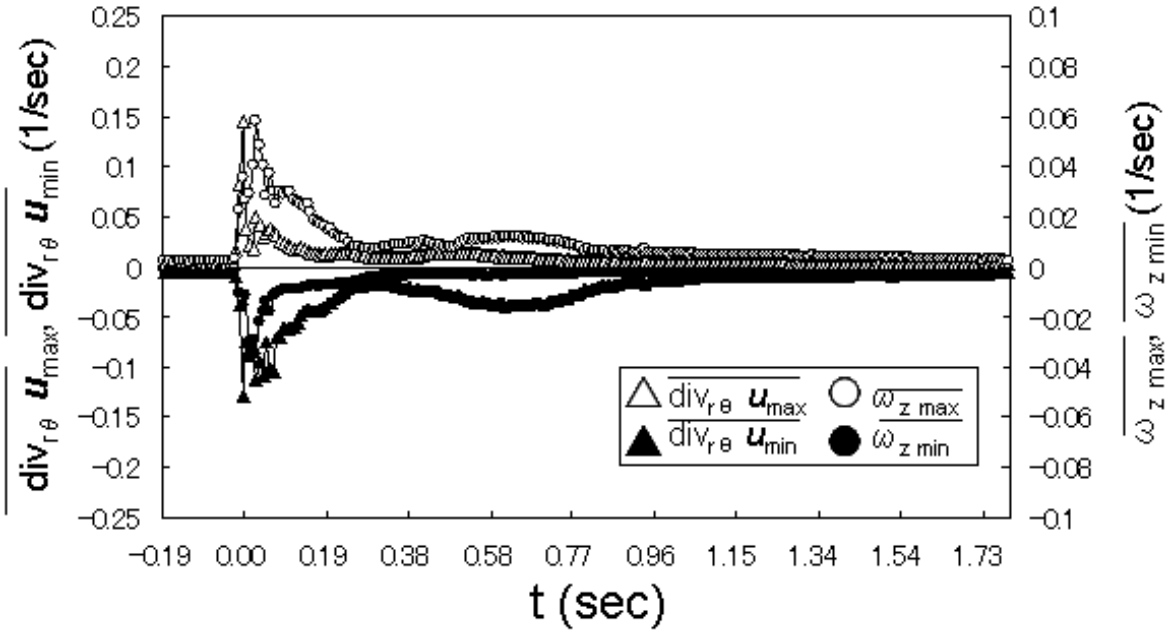

Figure 3.9: Particle A: time series of $\mathrm{div}_{r\theta}\boldsymbol{u}_{max}$, $\mathrm{div}_{r\theta}\boldsymbol{u}_{min}$, $\omega_{z\ max}$ and $\omega_{z\ min}$

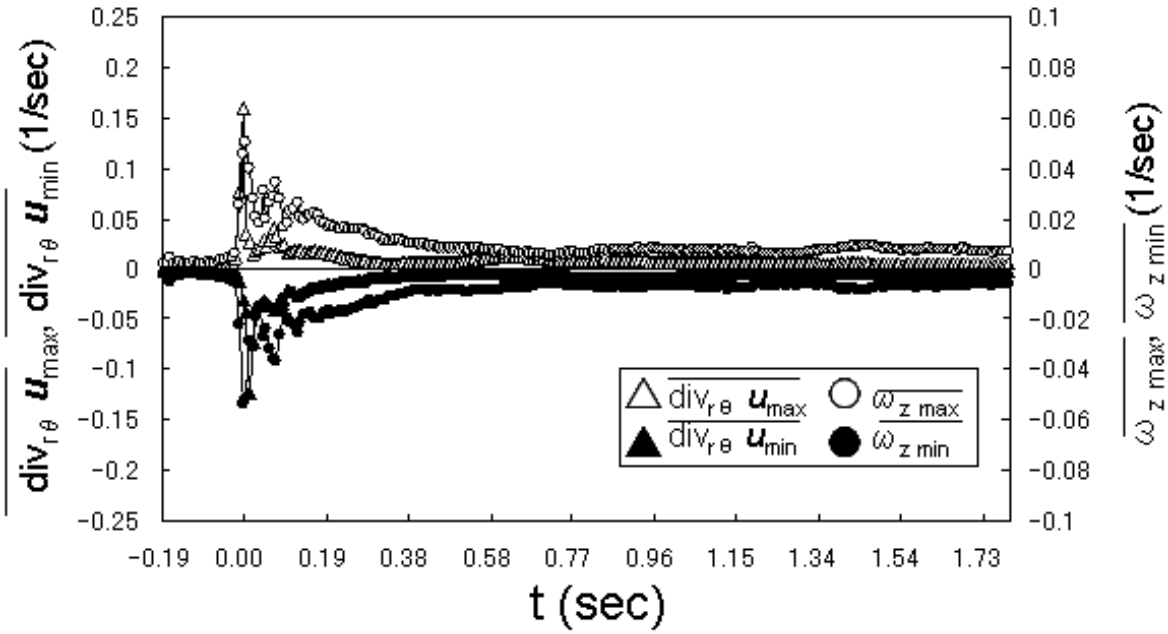

Figure 3.10: Particle B: time series of $\mathrm{div}_{r\theta}\boldsymbol{u}_{max}$, $\mathrm{div}_{r\theta}\boldsymbol{u}_{min}$, $\omega_{z\ max}$ and $\omega_{z\ min}$

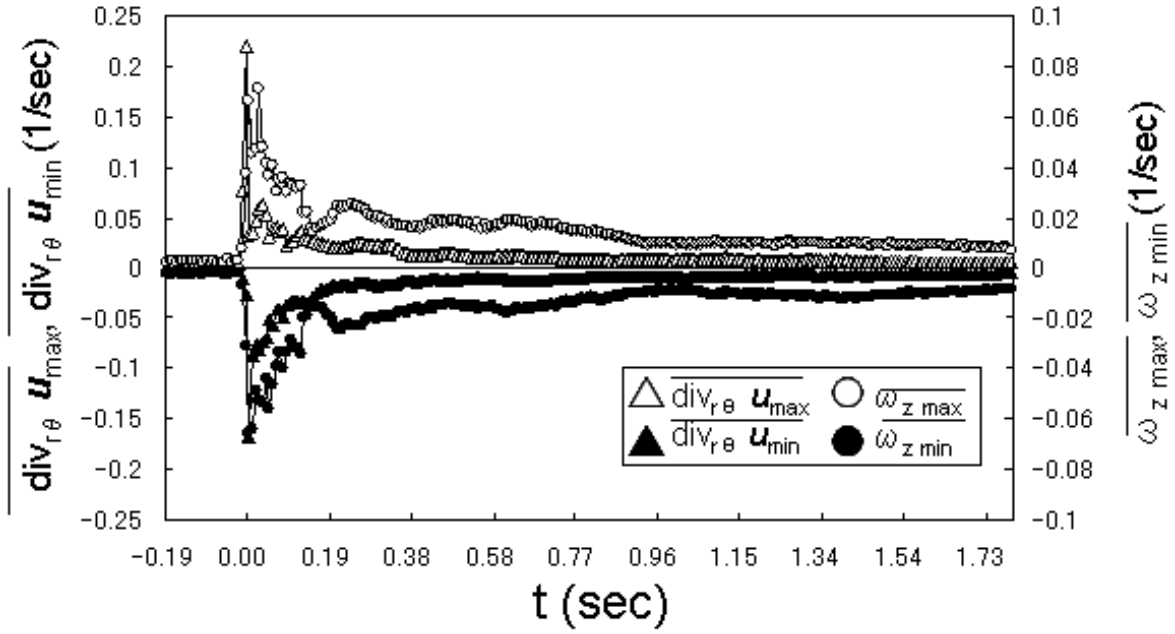

Figure 3.11: Particle C: time series of $\mathrm{div}_{r\theta}\boldsymbol{u}_{max}$, $\mathrm{div}_{r\theta}\boldsymbol{u}_{min}$, $\omega_{z\ max}$ and $\omega_{z\ min}$

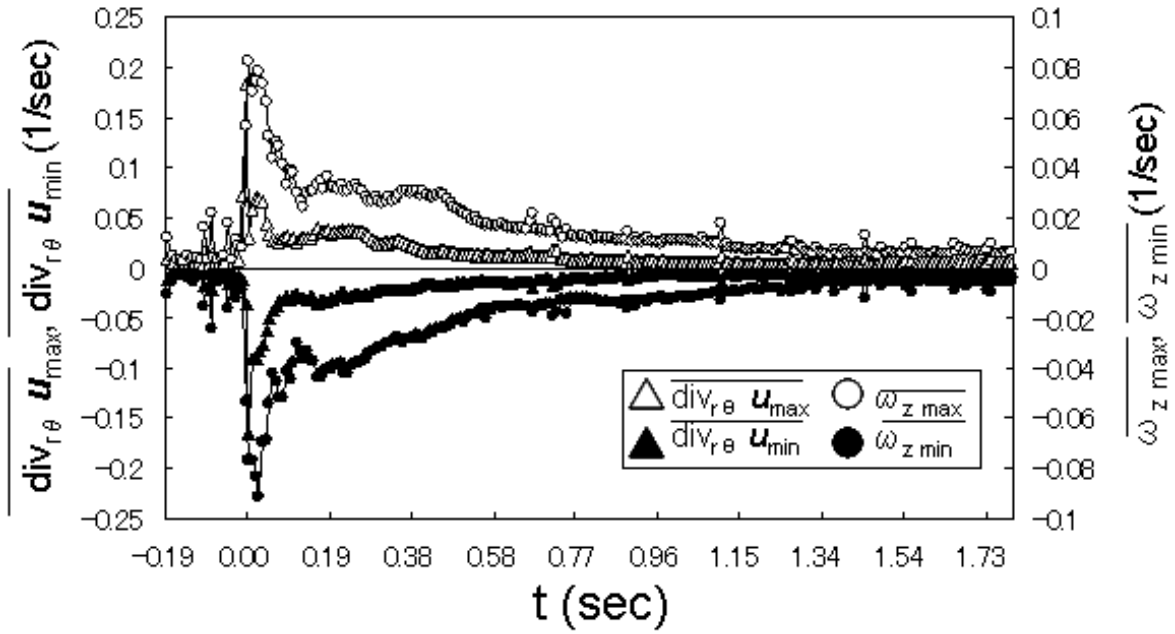

Figure 3.12: Particle D: time series of $\mathrm{div}_{r\theta}\boldsymbol{u}_{max}$, $\mathrm{div}_{r\theta}\boldsymbol{u}_{min}$, $\omega_{z\ max}$ and $\omega_{z\ min}$

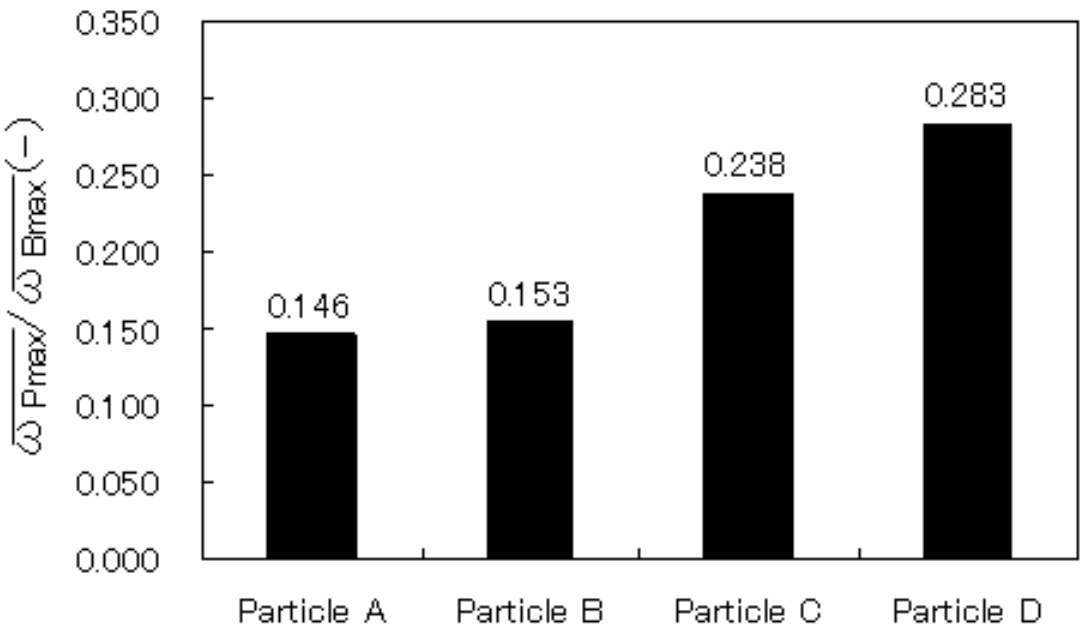

Figure 3.13: Ratio of the time averaged maximum vorticity $\overline{\omega_{Pmax}}$ generated by Particle A,B,C and D to time averaged maximum vorticity $\overline{\omega_{Bmax}}$ of Burgers vortex

Chapter 4

Influence of a settling particle on a Burgers vortex

4.1 Introduction

In this chapter, the influence of a settling particle on a Burgers vortex is divided into the influence of the flow around the particle and of the vortices shed from the particle, and these influences are examined, respectively. We focus on the maximum and minimum values of superficial divergence taken as the representative value of the flow around the particle, and examine the relation between the change of the maximum value of vorticity and the particle's passing position in a Burgers vortex. The influence of the shed vortices on a Burgers vortex is examined as the time change of the vorticity intensity. The interaction between wake structures and a Burgers vortex is observed at the time corresponding to the fluctuation of the vortex intensity. Moreover, as the characteristic fluctuation, the vortex core is observed in detail.

4.2 Influence of the flow around a settling particle on Burgers vortex

Figure 4.1 presents the change of vorticity fields and superficial divergent fields with respect to z/d_p in the cases of Particle B passing through the forced vortex area and the passing through the free vortex area. The distance z between the particle and the observation plane is derived from the product of the measured particle velocity and the elapsed time from the moment that the particle passes through the plane. To observe the influence of the particle position in z direction on the vortex, we ex-

amined the instantaneous maximum values of the vorticity $\omega_{z\ max}$ and the superficial divergence $\overline{\mathrm{div}_{r\theta} u_{max}}$. Figure 4.2 shows the change of $(\omega_{z\ max} - \overline{\omega_{z\ max}})/\overline{\omega_{z\ max}}$ and $\mathrm{div}_{r\theta} u_{max}/\overline{|\mathrm{div}_{r\theta} u_{max}|}$ corresponding to the results of Fig. 4.1. Each value is non-dimensionalized by the time averaged value without the particle. As theoretically predicted in Sec. 2.6.2, superficial divergent flow is induced by the particle approaching the plane ($z/d_p = -1.364$), and superficial convergent flow is induced by the particle leaving the plane ($z/d_p = 1.364$).

In the case of particle passing through the forced vortex area indicated in (a) of Fig. 4.2, increase of the maximum vorticity is observed at $z/d_p = -1.364$ and $z/d_p = 1.364$ - 9.546 corresponding to the peaks of the superficial divergence. On the other hand, in the case of particle passing through the free vortex area, the increase of the maximum vorticity is not observed. In figures 4.1 (a) and (c) it is observed that the vorticities shed from a particle passing in the forced vortex is stronger than the shed vorticities in the free vortex. However, the increase of divergences in both area are almost same as shown in Figs. 4.1 (b) and (d). The same tendency is observed in cases of Particle A, C and D.

Figure 4.3-4.6 show the effect of particle passing through position relative to the vortex axis on the increase rate of maximum vorticities corresponding to the maximum and minimum divergences. Here, the increase rate of the maximum vorticity is defined as $((\omega_{z\ max} - \overline{\omega_{z\ max}})/\overline{\omega_{z\ max}})$. $\overline{\omega_{\mathrm{z\ max}}}$ is the time averaged value without the particle. As observed in (a) of Fig. 4.1, $\omega_{z\ max}$ increase in the case of the shed vorticities passing through the forced vortex area ($r/l_b < 1.12$). In contrast, $\omega_{z\ max}$ is not increased in the case of the shed vorticities passing through the free vortex area ($r/l_b > 1.12$). Additionally, these figures show that $\omega_{z\ max}$ is more increased by the higher particle velocity.

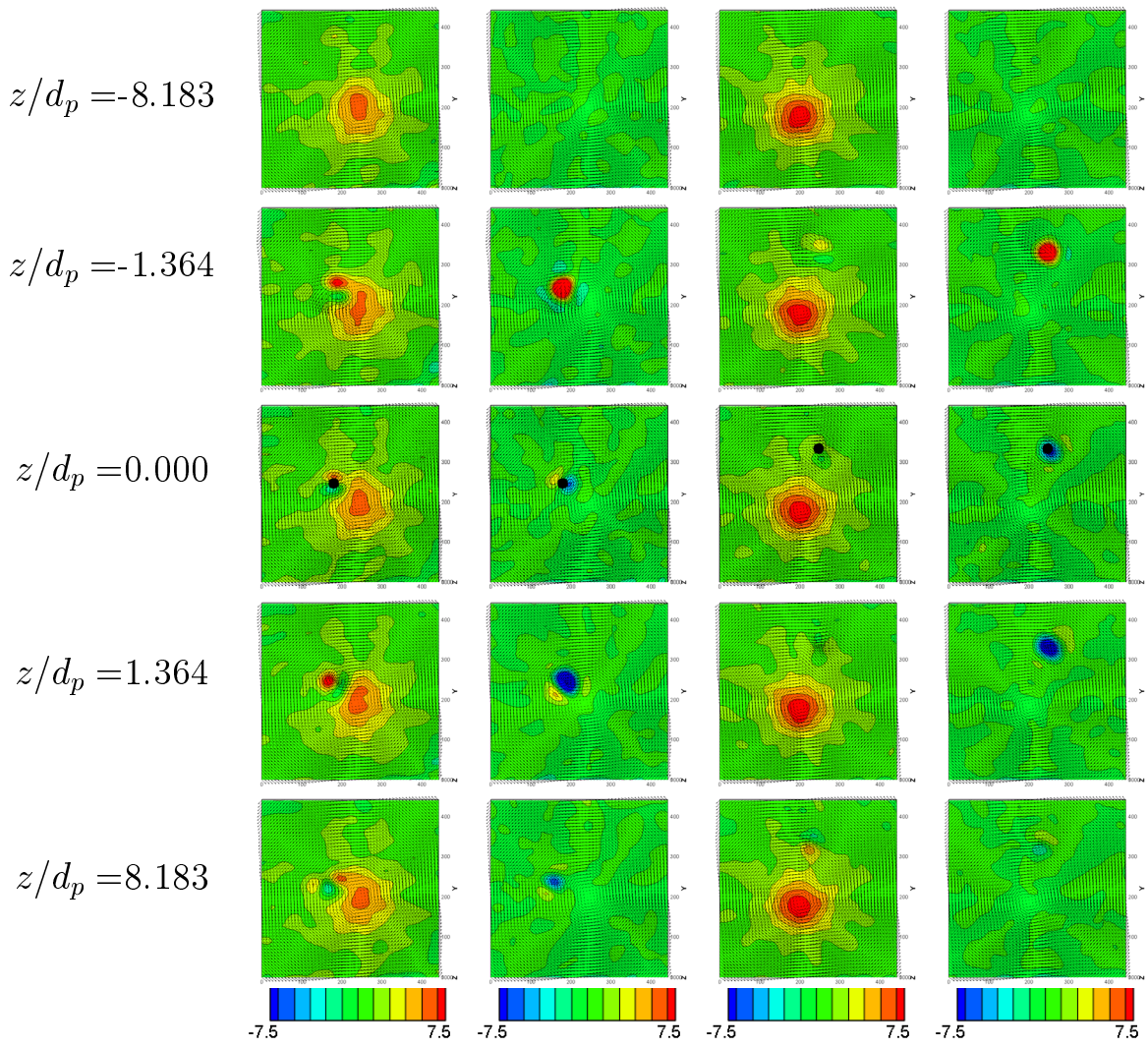

(a)	(b)	(c)	(d)
$r/1.12l_b$ =0.905	$r/1.12l_b$ =0.905	$r/1.12l_b$ =1.887	$r/1.12l_b$ =1.887
$\omega_z(r,\theta)$	$\mathrm{div}_{r\theta}u(r,\theta)$	$\omega_z(r,\theta)$	$\mathrm{div}_{r\theta}u(r,\theta)$

Figure 4.1: $\omega_z(r,\theta)$ and $\mathrm{div}_{r\theta}u(r,\theta)$ for each z/d_p (Particle B)

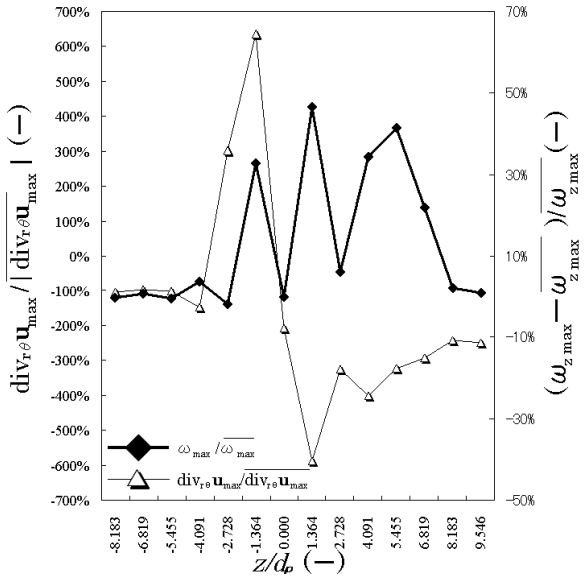

(a) $r/1.12l_b$=0.905

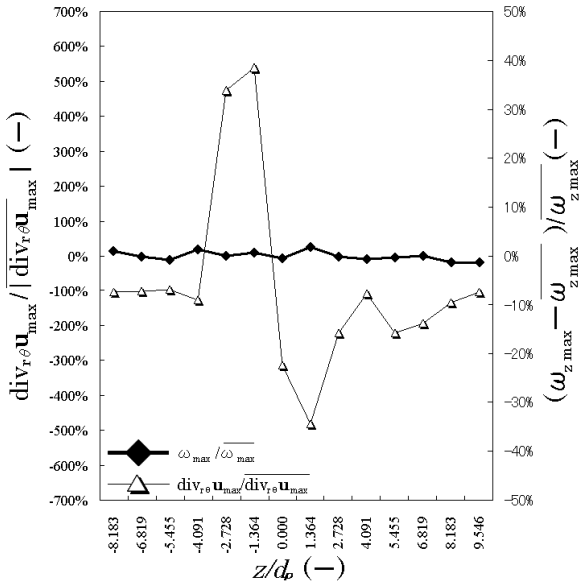

(b) $r/1.12l_b$=1.887

Figure 4.2: $\omega_{z\ max}$ and $\mathrm{div}_{r\theta}u_{max}$ for each t (Particle B)

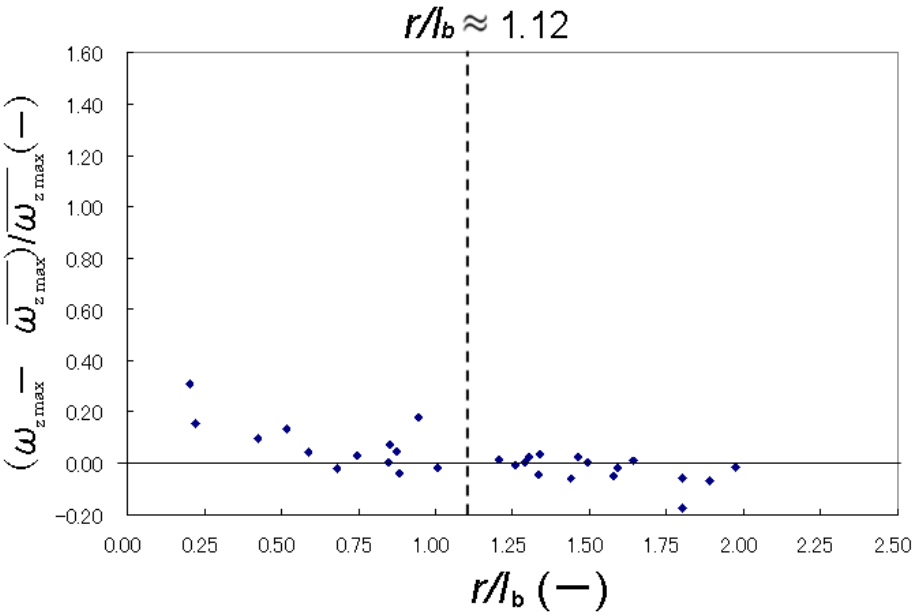

Divergent flow

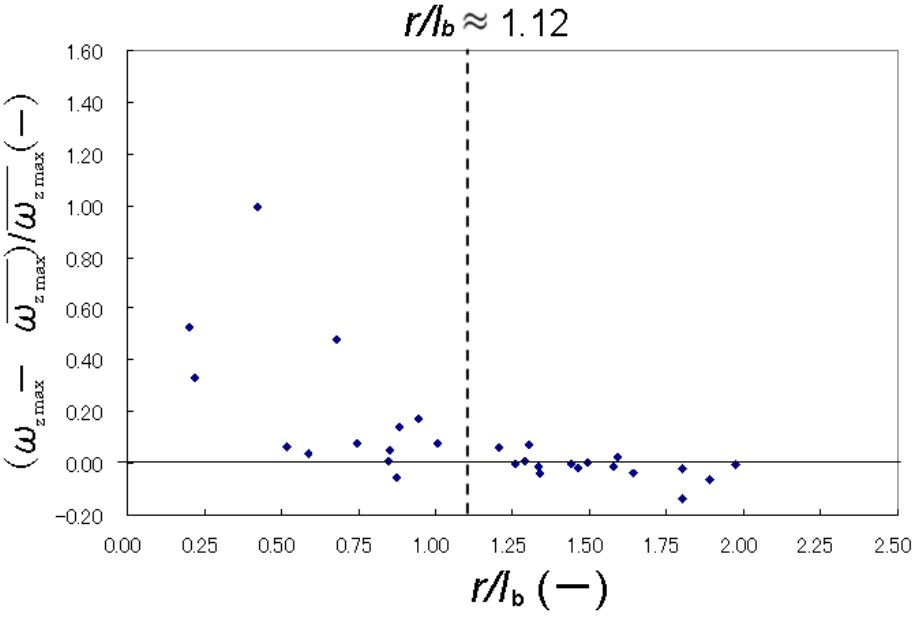

Convergent flow

Figure 4.3: Particle A ($Re_p = 1430$): Influence of particle's passing position on the change of $\omega_{z\,max}$

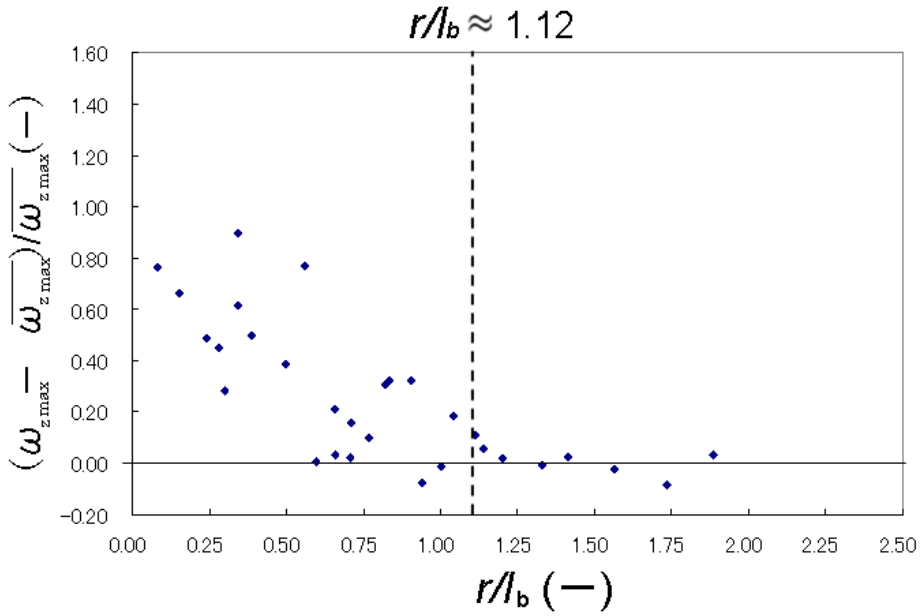

Divergent flow

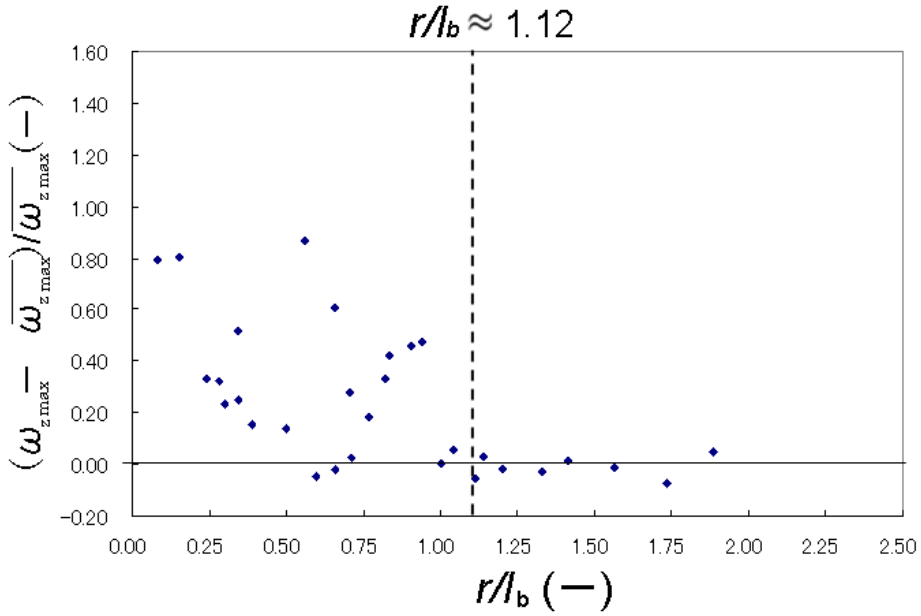

Convergent flow

Figure 4.4: Particle B (Re_p = 1940): Influence of particle's passing position on the change of $\omega_{z\,max}$

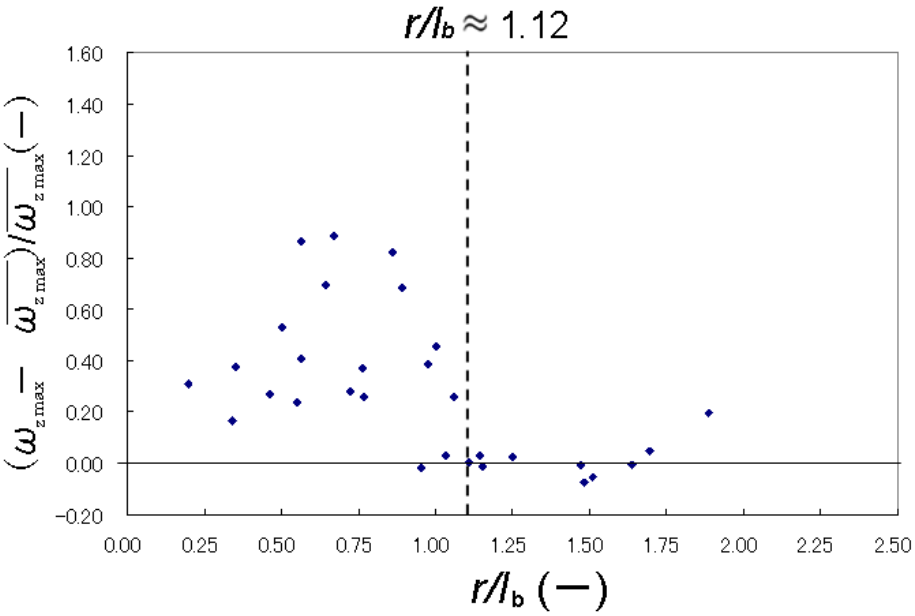

Divergent flow

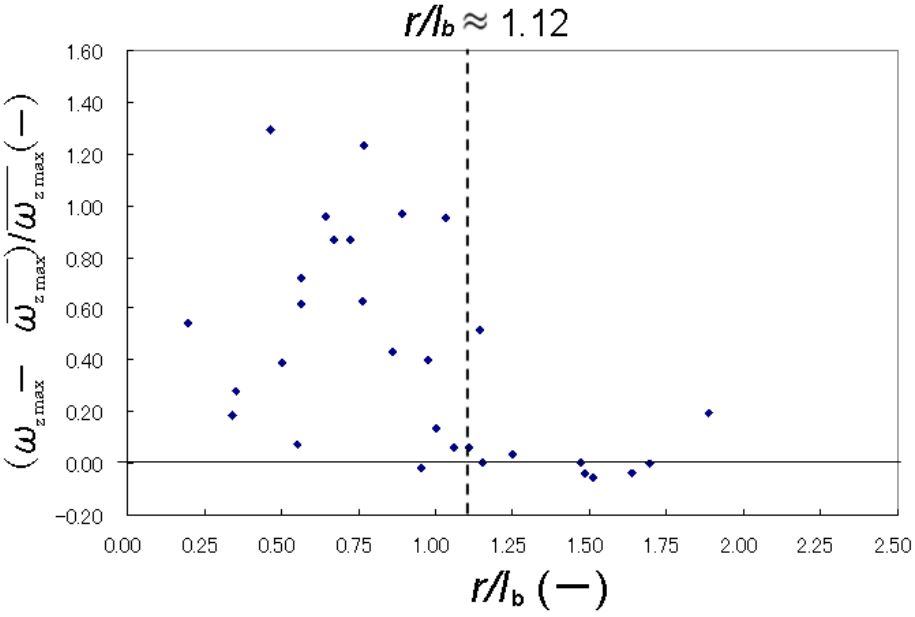

Convergent flow

Figure 4.5: Particle C ($Re_p = 3200$): Influence of particle's passing position on the change of $\omega_{z\,max}$

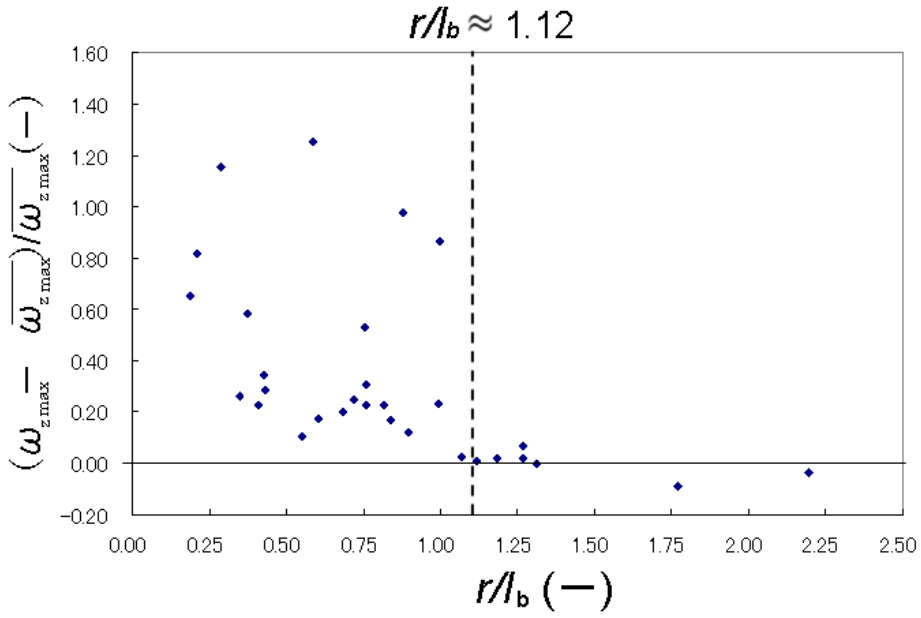

Divergent flow

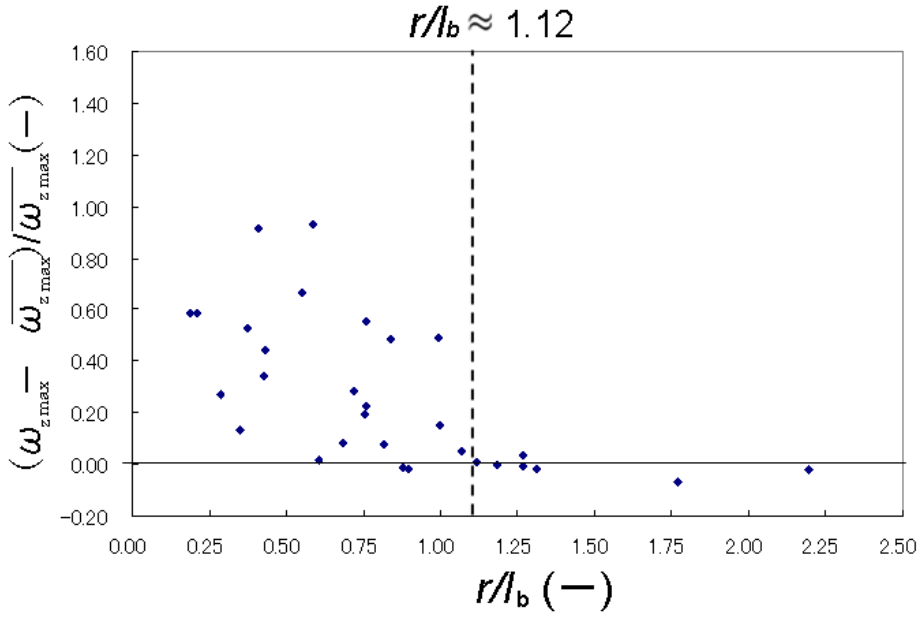

Convergent flow

Figure 4.6: Particle D ($Re_p = 3880$): Influence of particle's passing position on the change of $\omega_{z\,max}$

4.3 Interaction between Burgers vortex and vortex wake structure generated by a settling particle

We observe the time series of the circulation of the Burgers vortex when the particle passing through the vortex. We obtained 30 samples of PIV data (57×57 vectors, 2.0 sec with 250 frames) for each particle. The time series of the circulation are plotted in Figs. 4.8-4.10. Here, the circulation is non-dimensionalized by the time averaged circulation $\overline{\Gamma}$ for 0.2 seconds before particle passing through.

Despite the fact that all wake vorticities in stationary fluid are smaller than those of the Burgers vortex as indicated in Fig. 3.13, within the present observation time, the large fluctuation of the circulation occurs after particle passing through. It is predicted that there will be a long-time effect of a settling particle on the circulation, and the fluctuation will converge to the initial state after a long time.

From examined samples, we select two representative examples of the fluctuation of the circulation. For the two cases of the increase of the circulation ($\Gamma(1.8)/\overline{\Gamma} > 1$) and the decrease of the circulation ($\Gamma(1.8)/\overline{\Gamma} < 1$) at the end of the observation time, we examine the interaction between wake vortices generated by Particle D and the Burgers vortex. Figures 4.11 and 4.13 show time series of $\Gamma(t)/\overline{\Gamma}$ and iso-surface of vorticity in quasi-three dimensional fields. In these figures, the time series of the circulation and iso-surface of vorticity are displayed on the common time axis. Vorticity distribution $\omega_z(r,\theta)$, superficial divergence distribution $\mathrm{div}_{r\theta}\boldsymbol{u}(r,\theta)$ and BVD distribution $\mathrm{BVD}(r,\theta)$ are observed at each time as shown in Figs. 4.12 and 4.14. In the vorticity distribution, the area enclosed by a white circle indicates the integral range of $\Gamma(t)$.

In the case of $\Gamma(1.8)/\overline{\Gamma} > 1$ shown in Fig. 4.11 and Fig. 4.12, Particle D passes through the forced area ($r/1.12l_b = 0.76$). The circulation is fluctuating in the time range of (b) to (i). In the time range of (c) to (g), several pairs of vorticities and superficial divergences are observed in $\omega_z(r,\theta)$, $\mathrm{div}_{r\theta}\boldsymbol{u}(r,\theta)$ and $\mathrm{BVD}(r,\theta)$. When the circulation increases, positive vorticity exists in the area. On the other hand, when the circulation decreases, negative vorticity exists in the area. As described in Sec 3.3, a pair of vorticities and superficial divergences are shedding from a settling particle. Thus it is found that the fluctuation of the circulation is caused by the shed vortices. In the time range from (i) to (k), pair of superficial divergence is not observed. However, it is observed that the mergence of the vortex core occur. Here, the vortex core is the vorticity of the forced vortex area.

In the case of $\Gamma(1.8)/\overline{\Gamma} < 1$, Particle D passes through the free vortex area ($r/1.12l_b = 1.07$) as shown in Fig. 4.13 and Fig. 4.14. The circulation is fluctuating from the time range (b) to (g). In the time range from (b) to (f), several pairs of vorticities and superficial divergences are observed as the case of increase of the circulation. In the time range from (i) to (k), the fragmentation of the vortex core is observed.

4.4 Conclusion

The influence of the flow around a settling particle on a Burgers vortex and the interaction between the wake vortices shed from the particle and a Burgers vortex are examined in this chapter.

In the near-particle region, it is found that the maximum vorticity increases in the case of particle passing through the forced vortex area, on the other hand, the maximum vorticity is not affected in the case of particle passing through the free vortex area. Although the rotation of a settling particle is not measured in this study, it is supposed that the circumferential velocity decreases at the surface of the particle in the forced vortex area than the free vortex area. As a results, it is considered that velocity gradient increases, and vorticity increases.

In the wake of particle, the interaction between the vortices shed from the particle and the Burgers vortex induces the large fluctuation in the circulation of the vortex. It is predicted that there will be a long-time effect of a settling particle on the circulation, and the fluctuation will converge to the initial state after a long time. Moreover, the fragmentation and the mergence of the Burgers vortex core are observed. Because of three-dimensional structure of the interaction, it is supposed that z-component of the vorticity increases (decreases), and then other components decrease (increase). Thus, the mergence (the fragmentation) will occur. Additionally, the shed vortices with the superficial divergences observed in stationary fluid are also observed in the forced and the free vortex of the Burgers vortex.

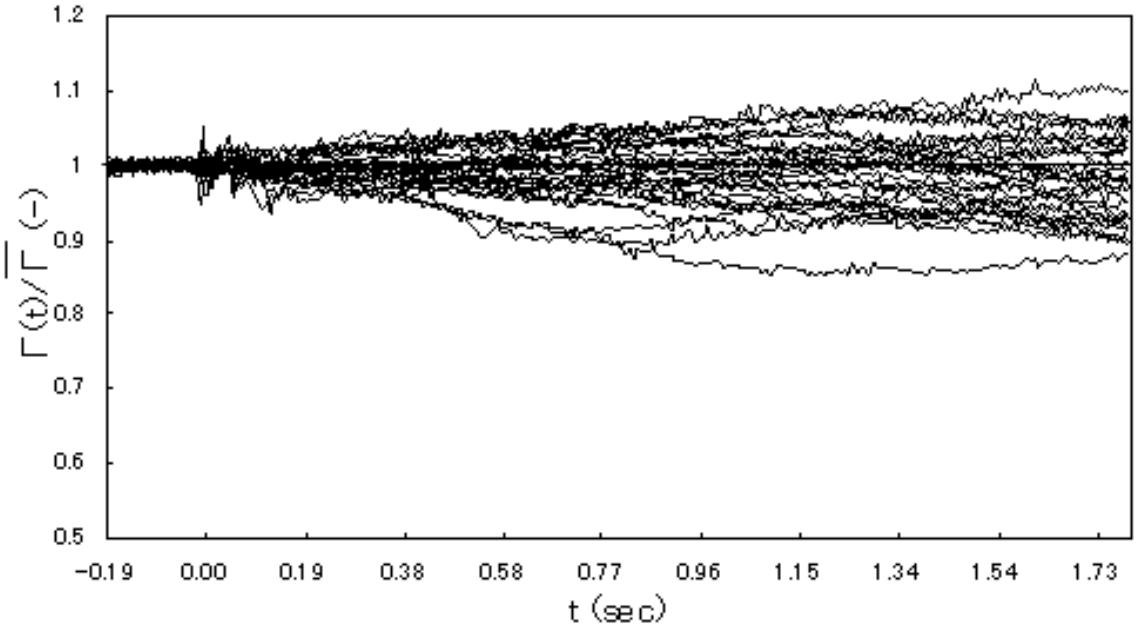

Figure 4.7: Particle A: time series of $\Gamma(t)/\overline{\Gamma}$

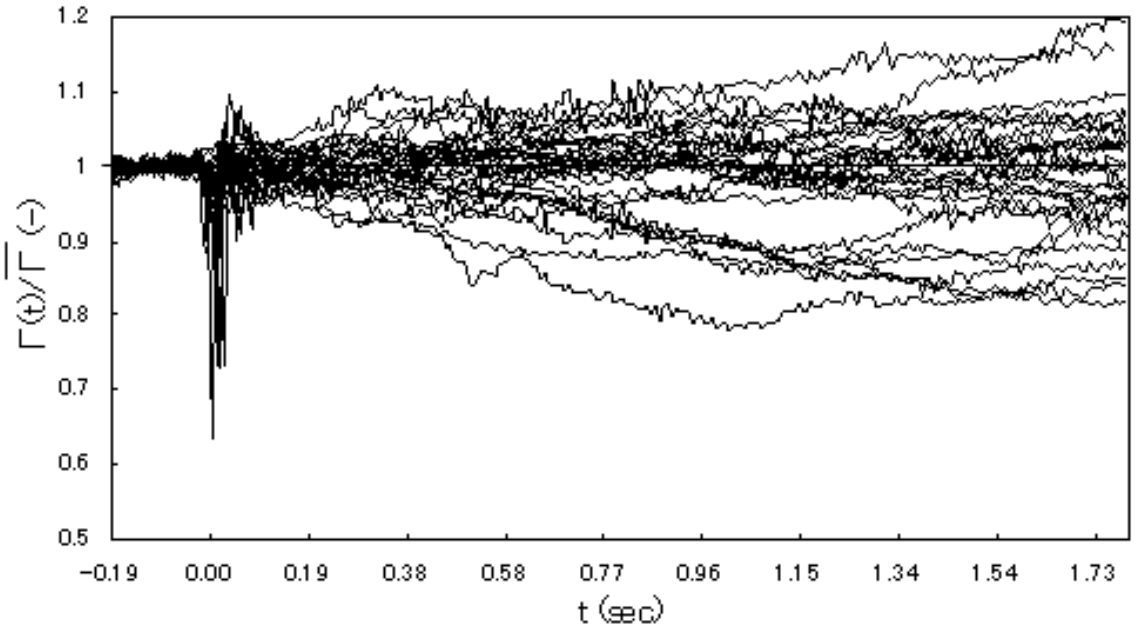

Figure 4.8: Particle B: time series of $\Gamma(t)/\overline{\Gamma}$

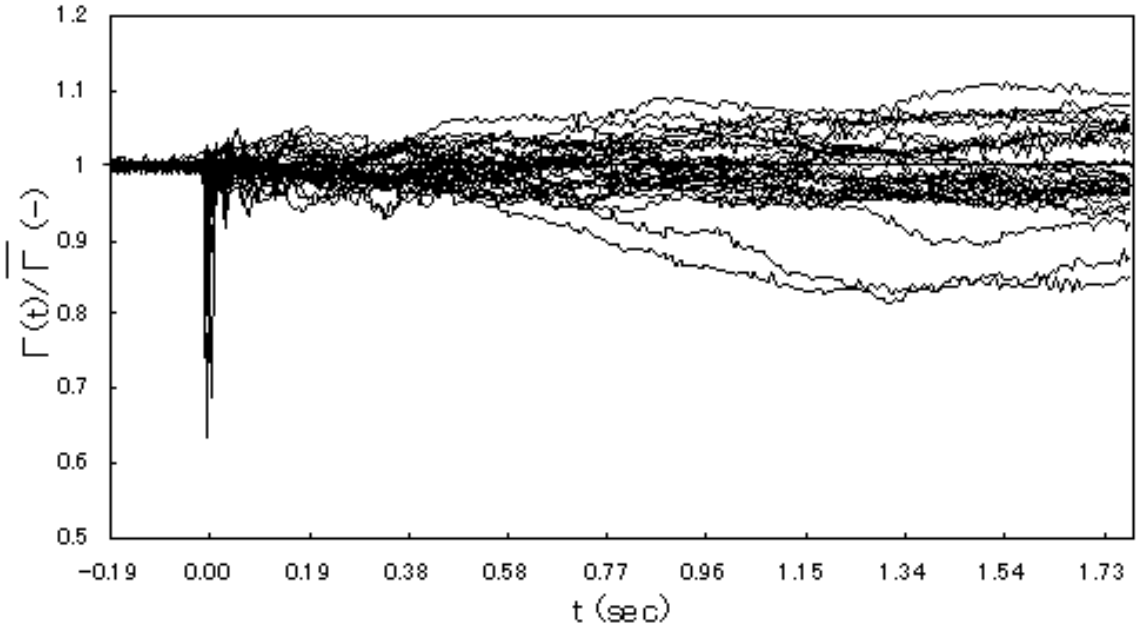

Figure 4.9: Particle C: time series of $\Gamma(t)/\overline{\Gamma}$

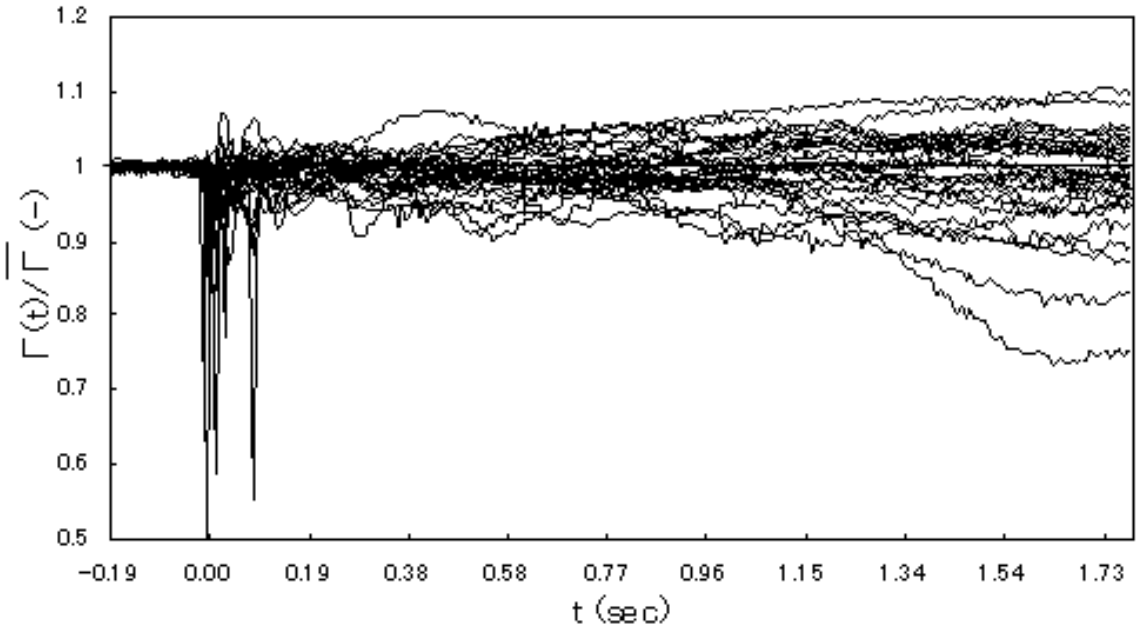

Figure 4.10: Particle D: time series of $\Gamma(t)/\overline{\Gamma}$

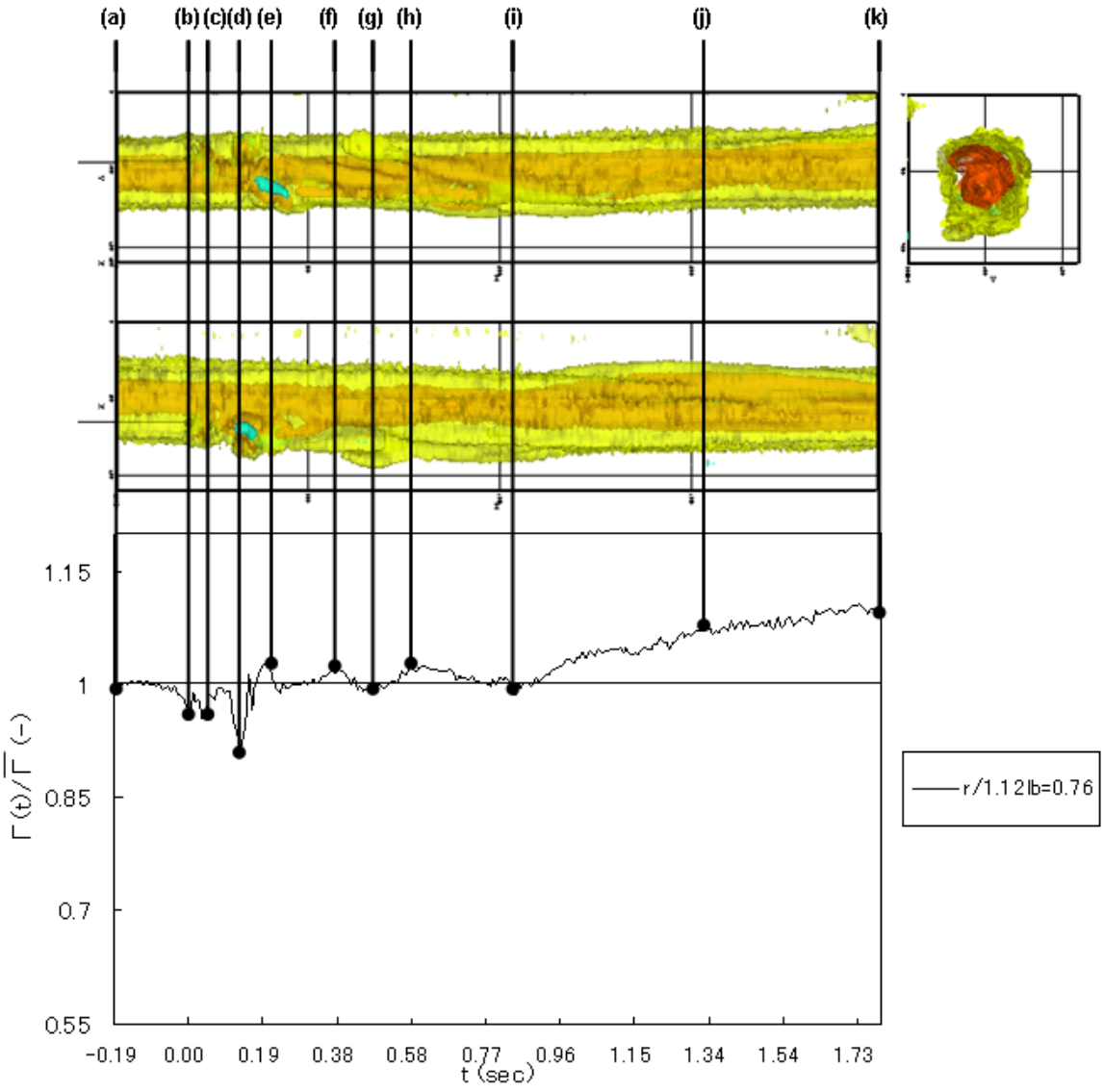

Figure 4.11: Particle D ($r/1.12l_b$ = 0.76, $\Gamma(1.8)/\overline{\Gamma}$ >1): time series of $\Gamma(t)/\overline{\Gamma}$ and iso-surface of vorticity magnitude (ω_z =6.25, 3.125 and -3.125)

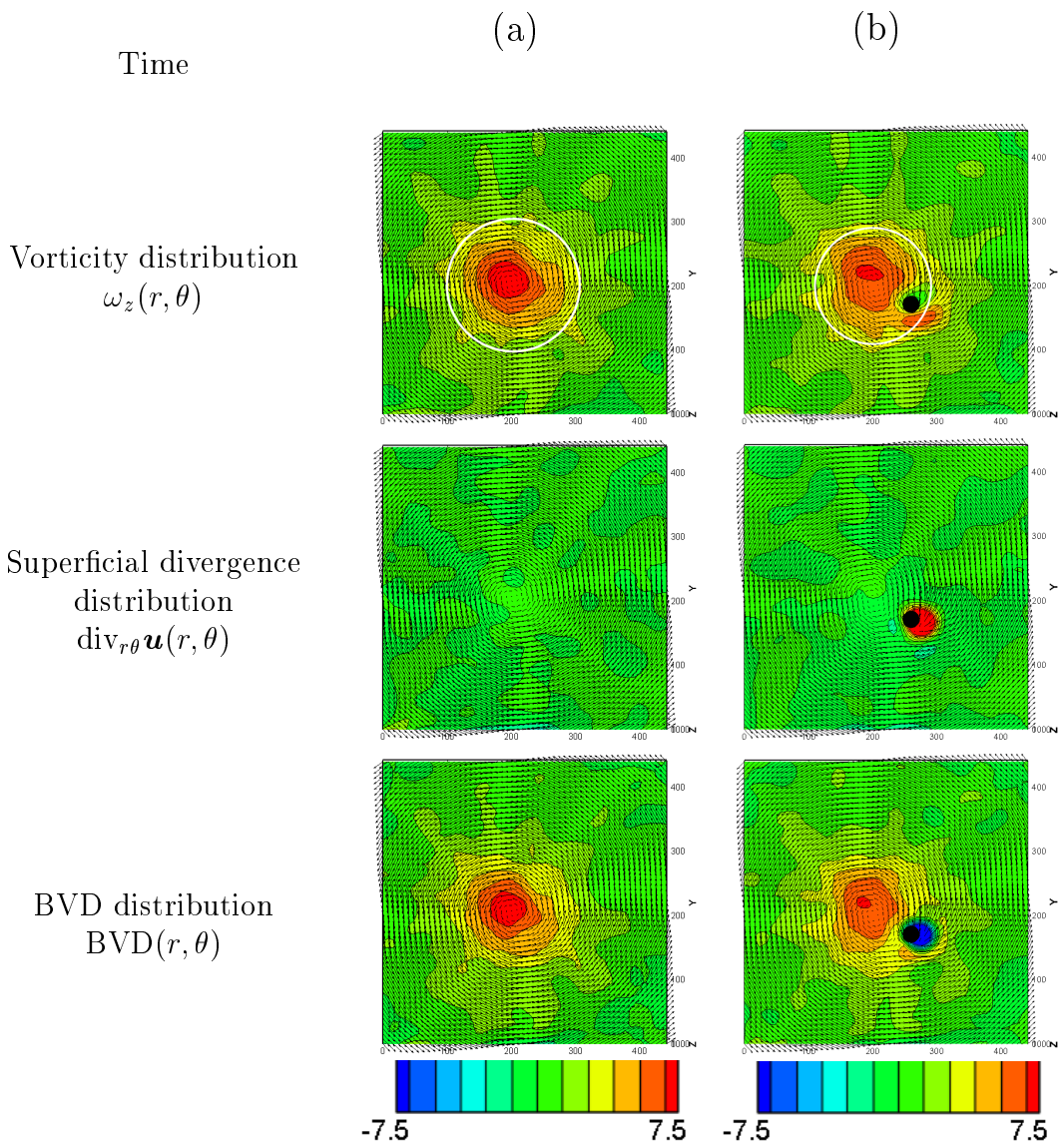

Figure 4.12**(1)**:Particle D ($r/1.12l_b = 0.76$): Comparison of $\omega_z(r,\theta)$, $\mathrm{div}_{r\theta}\boldsymbol{u}(r,\theta)$ and $\mathrm{BVD}(r,\theta)$ at different times. The area enclosed by a white circle indicates the integral range of $\Gamma(t)$.

(c) (d) (e)

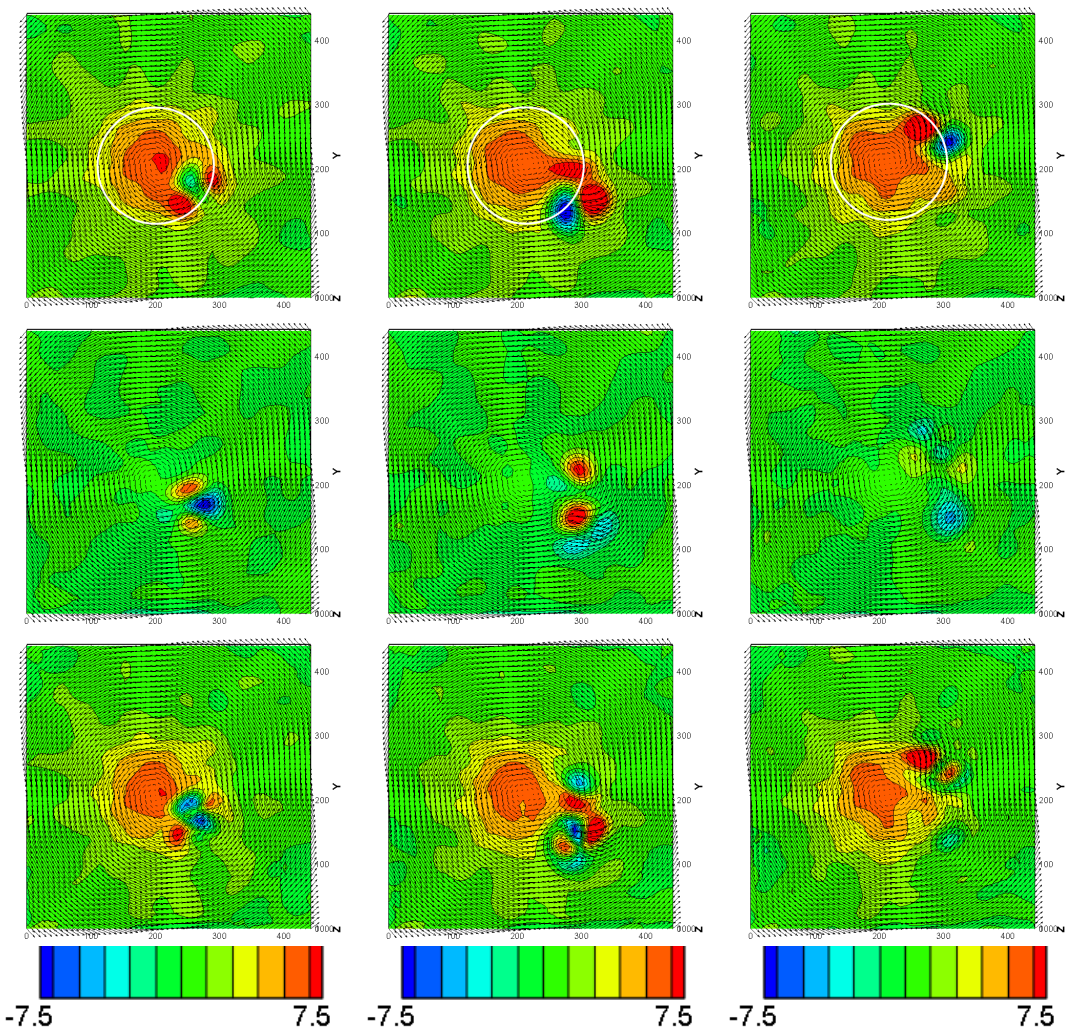

Figure 4.12**(2)**:Particle D ($r/1.12l_b = 0.76$): Comparison of $\omega_z(r,\theta)$, $\mathrm{div}_{r\theta}\boldsymbol{u}(r,\theta)$ and $\mathrm{BVD}(r,\theta)$ at different times. The area enclosed by a white circle indicates the integral range of $\Gamma(t)$.

(f) (g) (h)

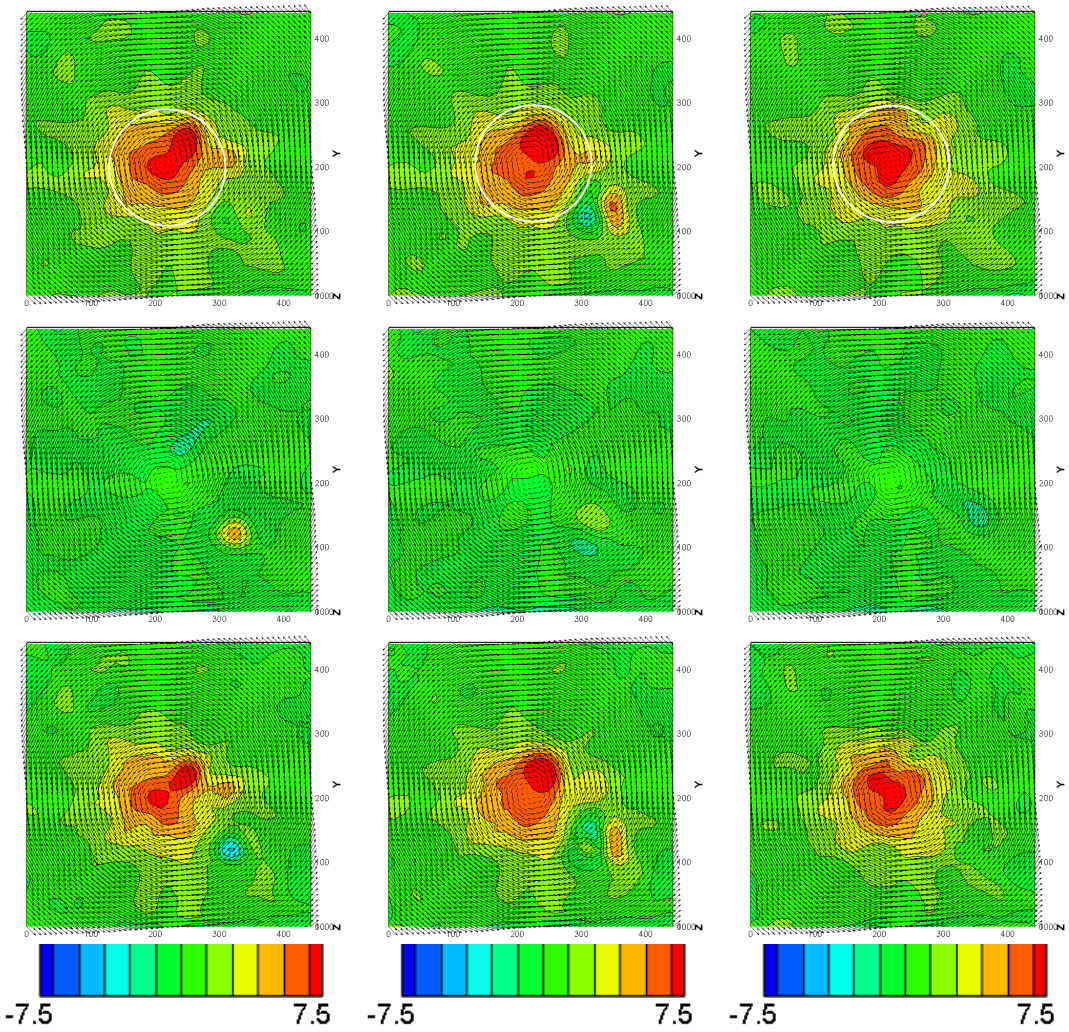

Figure 4.12**(3)**:Particle D ($r/1.12l_b = 0.76$): Comparison of $\omega_z(r,\theta)$, $\mathrm{div}_{r\theta}\boldsymbol{u}(r,\theta)$ and $\mathrm{BVD}(r,\theta)$ at different times. The area enclosed by a white circle indicates the integral range of $\Gamma(t)$.

(i) (j) (k)

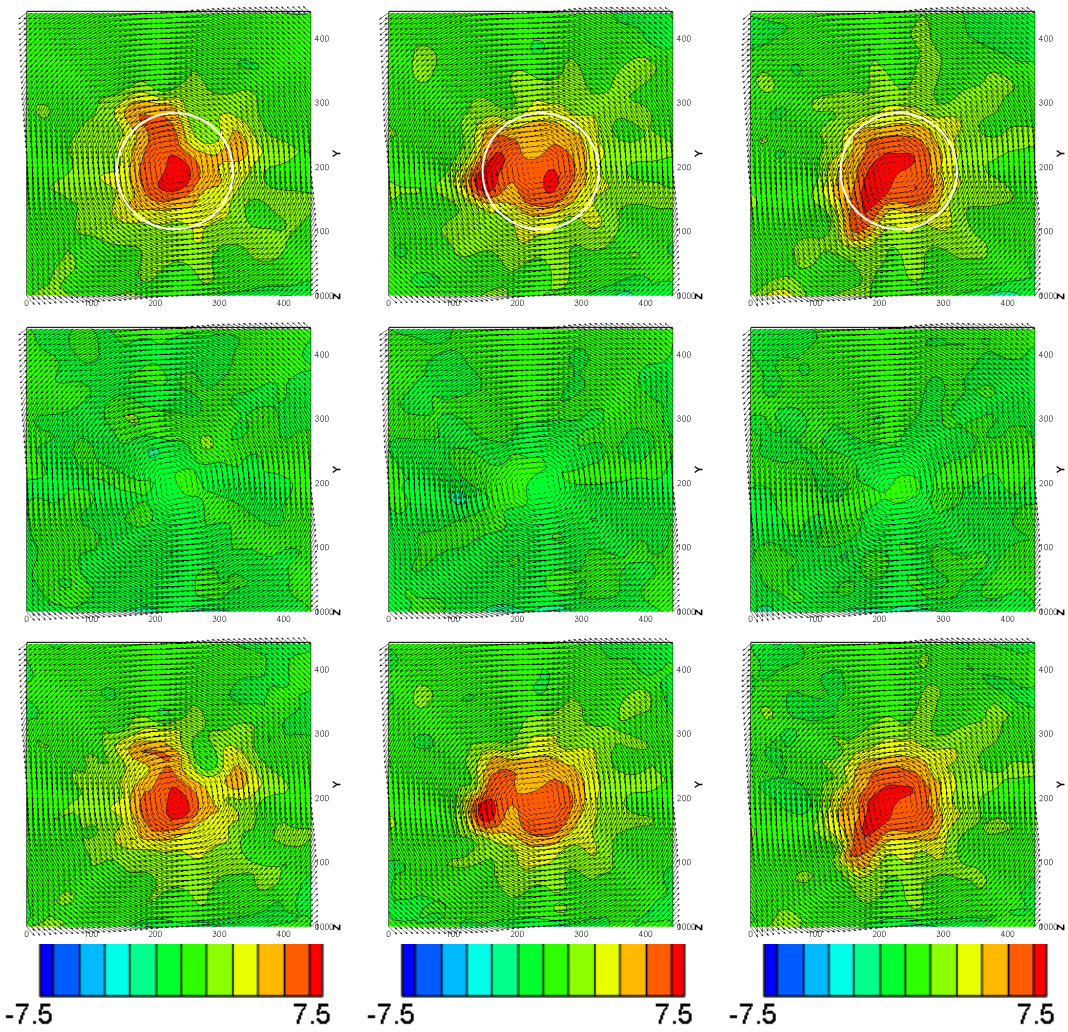

Figure 4.12**(4)**:Particle D ($r/1.12l_b = 0.76$): Comparison of $\omega_z(r,\theta)$, $\mathrm{div}_{r\theta}\boldsymbol{u}(r,\theta)$ and $\mathrm{BVD}(r,\theta)$ at different times. The area enclosed by a white circle indicates the integral range of $\Gamma(t)$.

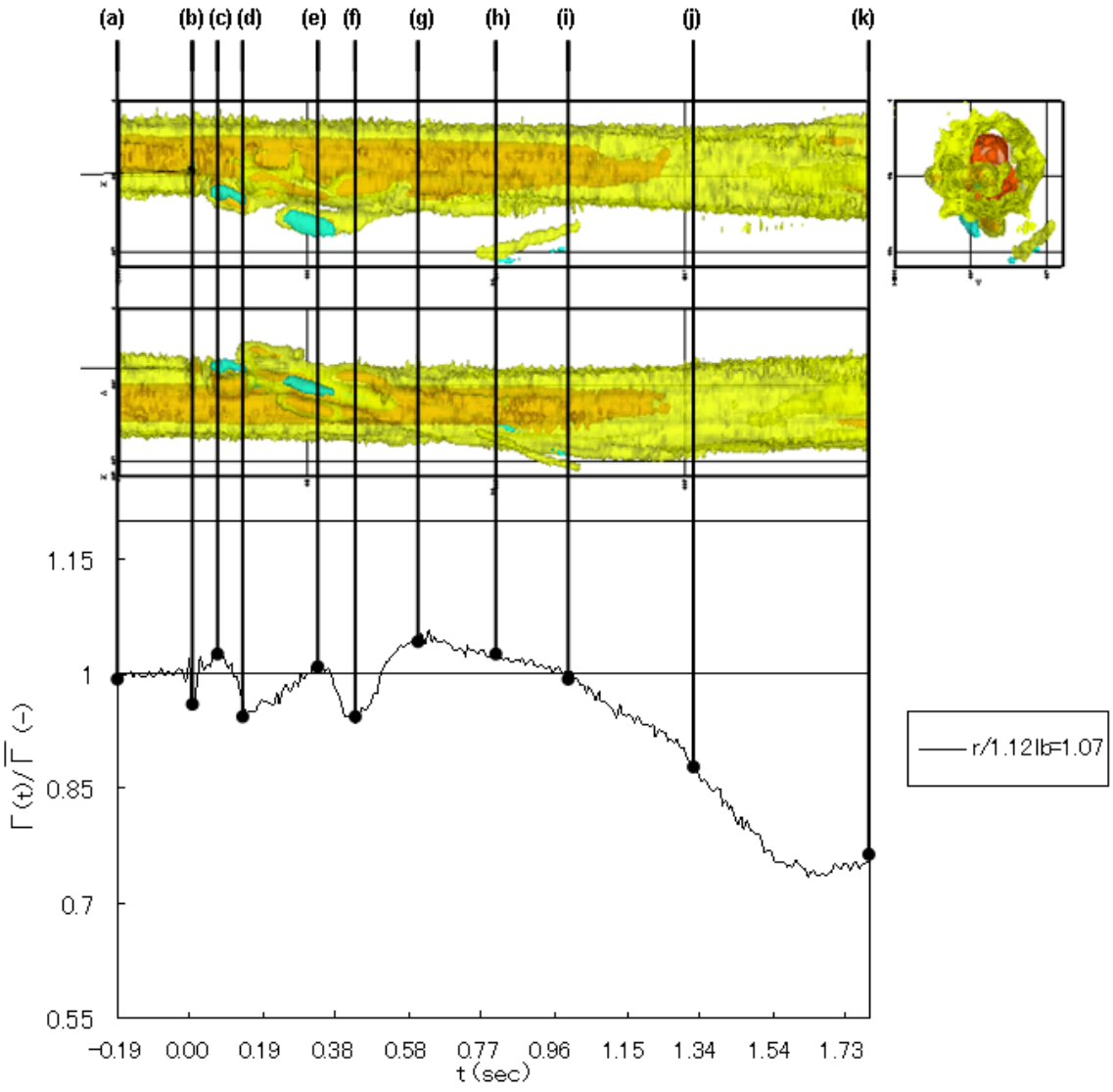

Figure 4.13: Particle D ($r/1.12l_b$ = 1.07, $\Gamma(1.8)/\overline{\Gamma}$ <1): time series of $\Gamma(t)/\overline{\Gamma}$ and iso-surface of vorticity magnitude (ω_z =6.25, 3.125 and -3.125)

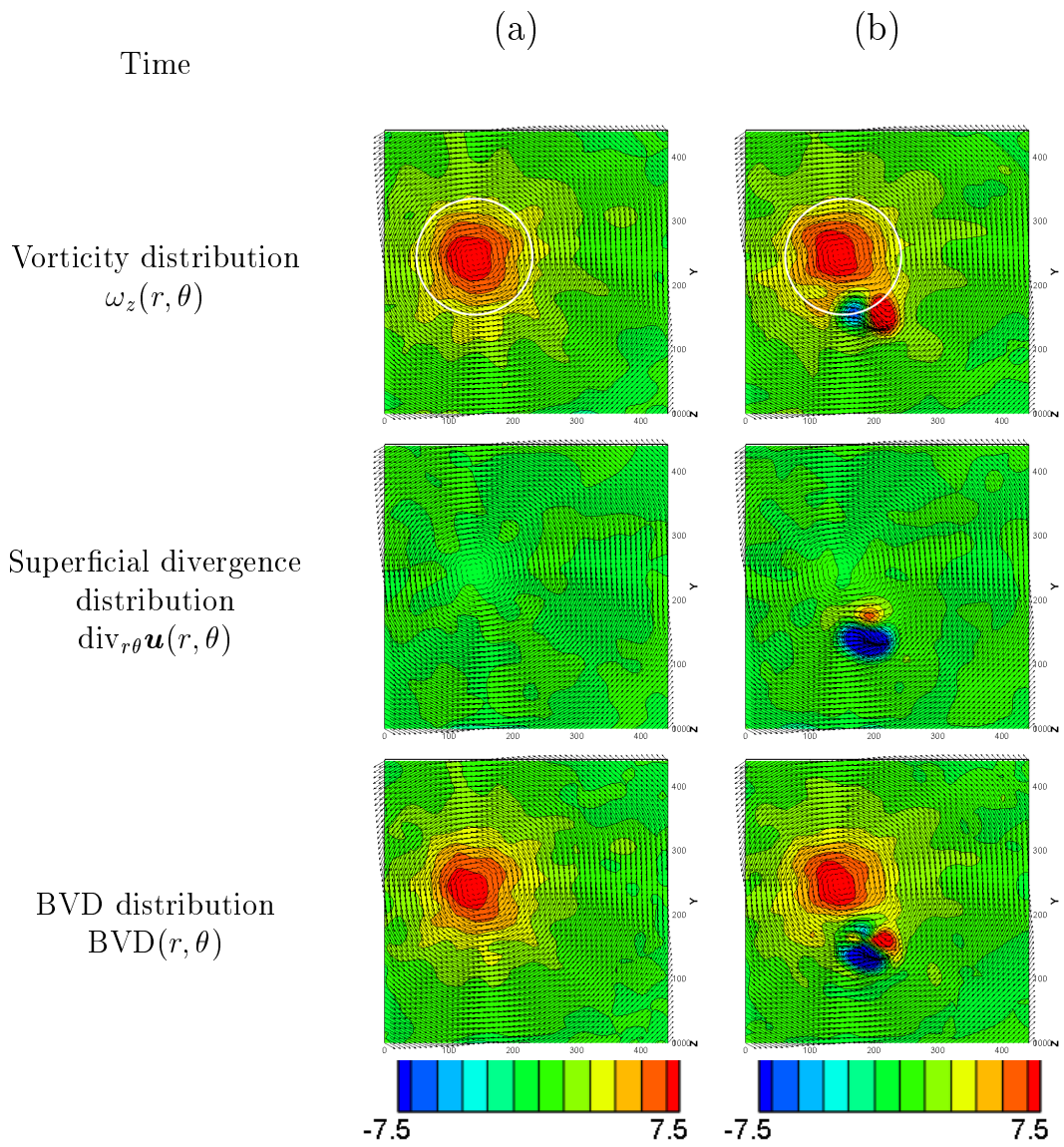

Figure 4.14**(1)**:Particle D ($r/1.12l_b = 1.07$): Comparison of $\omega_z(r,\theta)$, $\mathrm{div}_{r\theta}\boldsymbol{u}(r,\theta)$ and $\mathrm{BVD}(r,\theta)$ at different times. The area enclosed by a white circle indicates the integral range of $\Gamma(t)$.

(c) (d) (e)

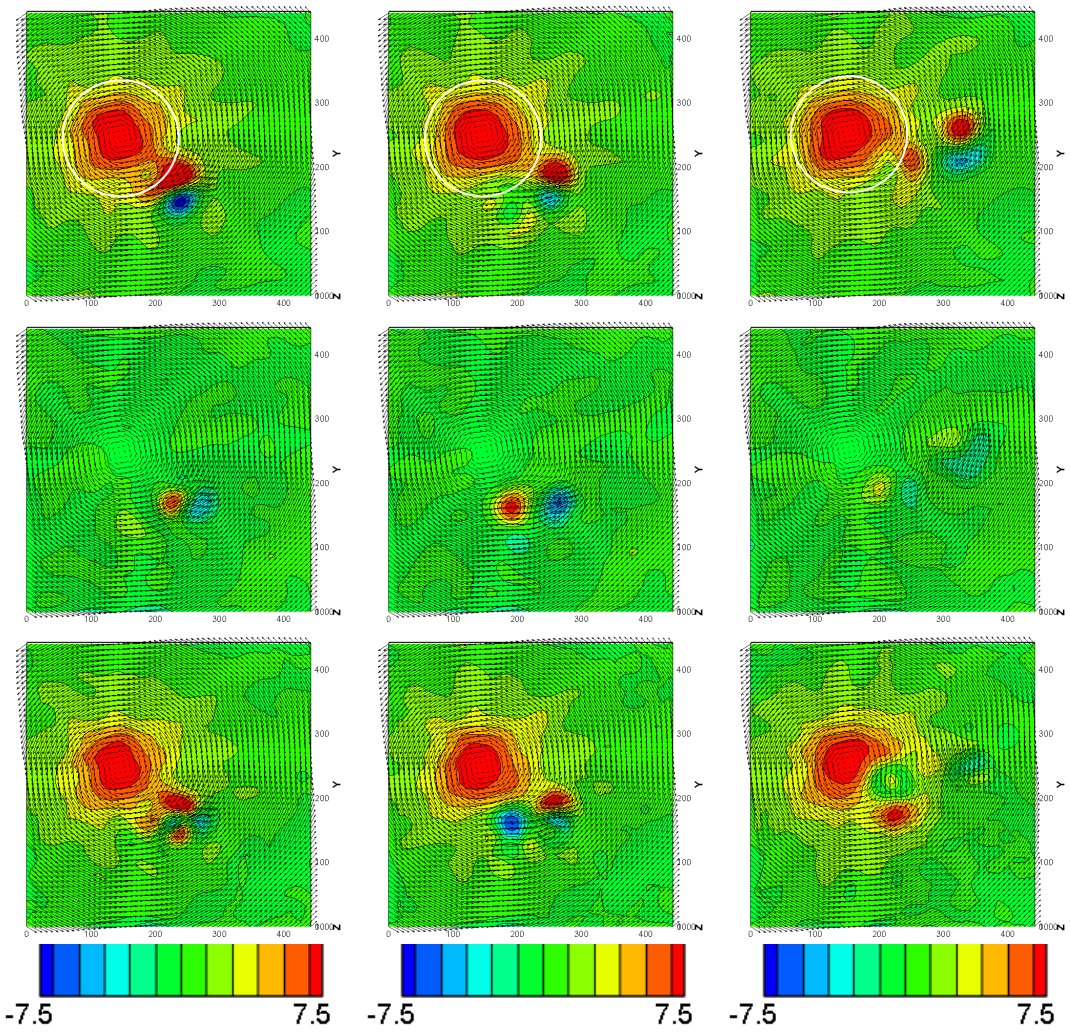

Figure 4.14**(2)**:Particle D $(r/1.12l_b = 1.07)$: Comparison of $\omega_z(r,\theta)$, $\mathrm{div}_{r\theta}\boldsymbol{u}(r,\theta)$ and $\mathrm{BVD}(r,\theta)$ at different times. The area enclosed by a white circle indicates the integral range of $\Gamma(t)$.

(f) (g) (h)

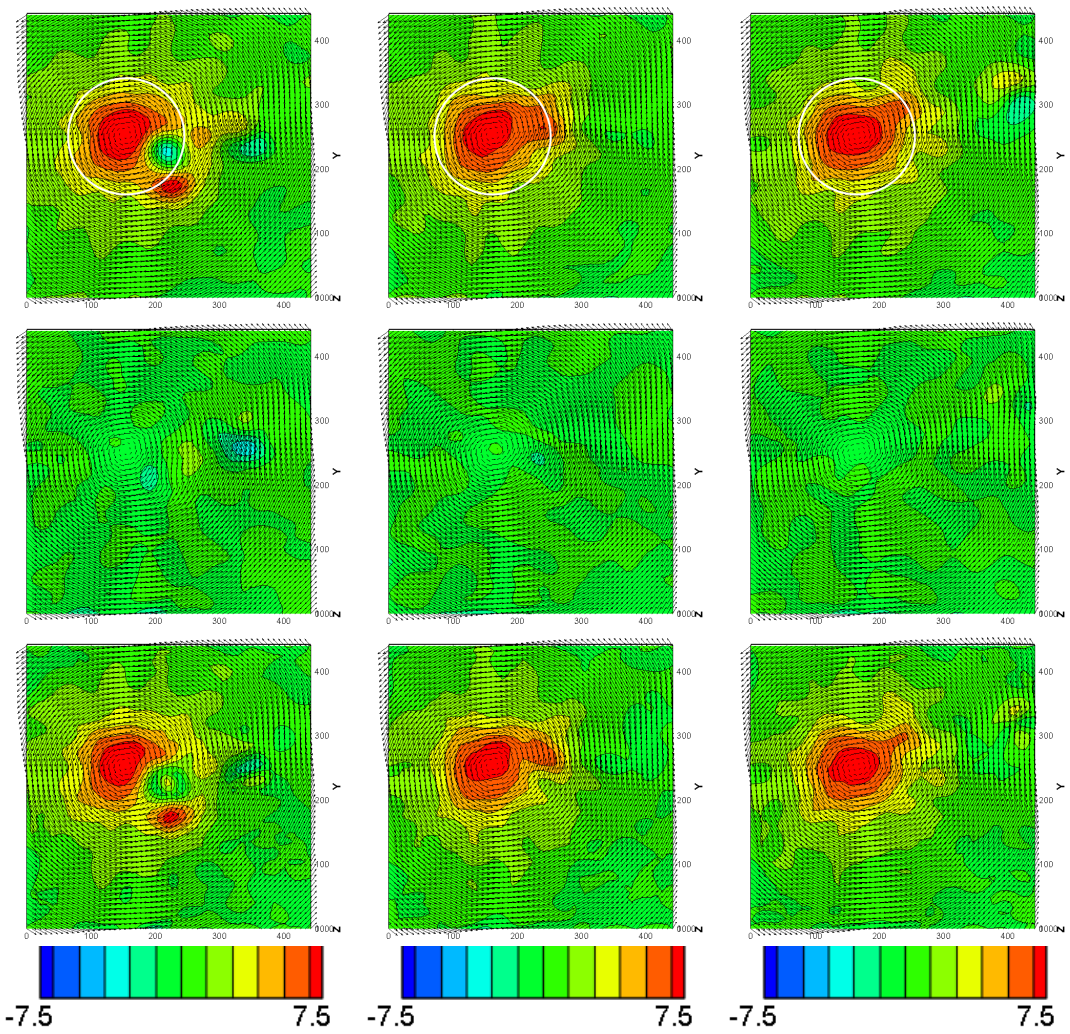

Figure 4.14**(3)**:Particle D ($r/1.12l_b = 1.07$): Comparison of $\omega_z(r,\theta)$, $\mathrm{div}_{r\theta}\boldsymbol{u}(r,\theta)$ and $\mathrm{BVD}(r,\theta)$ at different times. The area enclosed by a white circle indicates the integral range of $\Gamma(t)$.

(i) (j) (k)

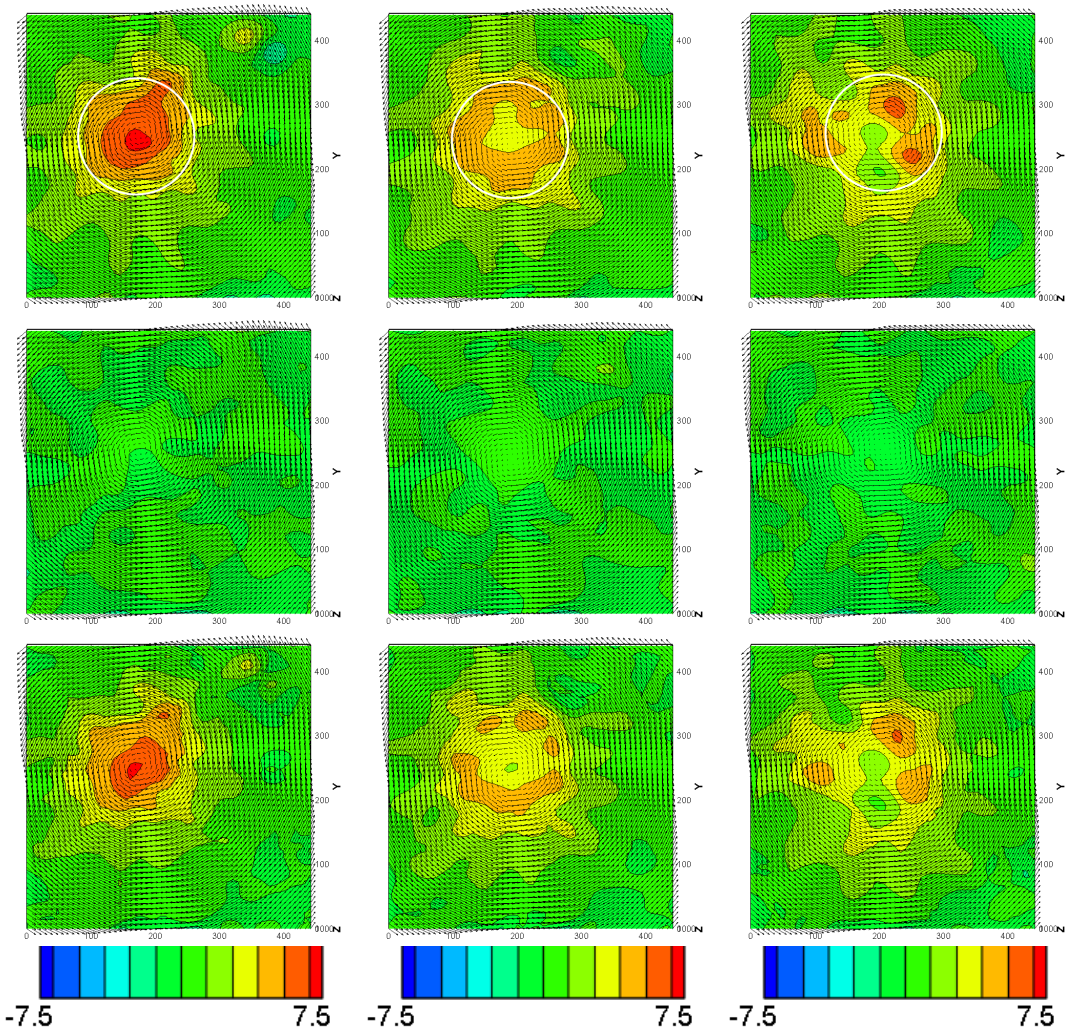

Figure 4.14**(4)**:Particle D ($r/1.12l_b = 1.07$): Comparison of $\omega_z(r,\theta)$, $\mathrm{div}_{r\theta}\boldsymbol{u}(r,\theta)$ and $\mathrm{BVD}(r,\theta)$ at different times. The area enclosed by a white circle indicates the integral range of $\Gamma(t)$.

Chapter 5

Conclusions

This thesis is devoted to an elementary study on the influence of a settling particle on a Burgers vortex. This study focuses on the influence of the flow around a settling particle on a Burgers vortex and the interaction between a Burgers vortex and the wake vortices generated by a settling particle. This work is composed of (1) generation of the Burgers vortex using newly developed vortex generator, (2) selection of the optimal PIV algorithm for the present study, (3) introduction of visualization methods of the influence of particle on the vortex, and (4) examination of the interaction between the Burgers vortex and a settling particle. The outline of the present work is as follows:

In Chapter 1, beginning with a review of turbulent flows laden with particles is provided. The theoretical basis of a Burgers vortex is described. Next the past works are described. Lastly the originality of this study is shown.

In Chapter 2, the experimental setup, conditions, Particle Image Velocimetry (PIV) techniques and the visualization techniques for the examination of the influence of a settling particle on a Burgers vortex are presented. A Burgers vortex, having the vortex axis directed in the gravitational direction, is generated in a cylindrical water tank. Flow fields in the observation plane perpendicular to the vortex axis is measured by PIV measurement. It is shown that the distribution of vorticity and velocity in the measured plane almost agrees with the theoretical ones of Burgers vortex, and its vortex Reynolds number is 6590. The correspondence of the generated vortex and the vortex of an isotropic turbulent flow is clarified by using the length-scale relation between an isotropic turbulent flow and a Burgers vortex. The vertical component of the particle velocity at the measuring cross section is measured by the particle velocimetry system.

Four kinds of particles, which have a same diameter but different densities, are used

in the present study. The resultant particle Reynolds numbers at the measuring section are ranged from 1430 to 3880, hence, all particles shed vortices. By analyzing the Stokes number concerning the traceability to the vortex motion, it is found that the particle motion is in an equilibrium state with respect to the vortex motion.

In order to select a PIV algorithm robust to decrease of tracer particles, the three representative PIV algorithms (CC-PIV, I-PIV and CEC-PIV) are examined. From the test results with using artificial images, it is found that CEC-PIV algorithm is most robust to the decrease of tracer particles. We conclude that CEC-PIV is the optimal PIV for the present study.

Two kinds of visualization methods for the flow field are proposed. A quasi-three-dimensional vorticity field is constructed by stacking two-dimensional vorticity fields. To make clear the effect of the three-dimensional flow structure on the two-dimensional flow measured on the plane, the superficial divergence on the measured plane is defined. Additionally, BVD distribution is proposed to present vorticity and superficial divergence field in the same plane.

In Chapter 3, the flow fields of the Burgers vortex and around a settling particle are independently observed.

To express the intensity of the vortex, a circulation of Burgers vortex is defined. The time change of the circulation of the Burgers vortex without particle settling is observed. The standard deviation of the observed flucutuation of the circulation is evaluated as 0.023.

The flow fields around the particles and of the vortices shed from the particles are examined by using the two-dimensional fields of vorticity, superficial divergence and BVD, and quasi-three-dimensional equi-vorticity surface structures.

In Chapter 4, the influence of the flow around a settling particle on a Burgers vortex and the interaction between the wake vortices shed from the particle and a Burgers vortex are examined.

It is found that the maximum vorticity increases in the case of particle passing through the forced vortex area, on the other hand, the maximum vorticity is not affected in the case of particle passing through the free vortex area.

Concerning the effect of the shed vortices on the Burgers vortex, the interaction induces a large fluctuation in the circulation of the vortex. Moreover, the fragmentation and the mergence of the Burgers vortex core are observed.

The present study provides knowledge about the influence of a settling particle on a Burgers vortex which is one of the elementary physics of particle-laden turbulent flows, and proposes the experimental techniques and setup for the observation of the influence. The main results are summarized as follows:

(1) The Burgers vortex is generated by the presented experimental setup, and the flow fields of a Burgers vortex affected by a gravitationally settling particle are obtained by the PIV measurement.

(2) In the near-particle region, the maximum vorticity of the vortex increases in the case of particle passing through the forced vortex area, on the other hand, the maximum vorticity is not affected in the case of particle passing through the free vortex area.

(3) In the wake of particle, the interaction between the vortices shed from the particle and the Burgers vortex induces the large fluctuation in the circulation of the vortex. Moreover, the fragmentation and the mergence of the Burgers vortex core are observed.

(4) Additionally, the shed vortices with the superficial divergences observed in static flow are also observed in the forced and the free vortex of the Burgers vortex.

The author hopes that the present study promotes the investigation of interactions between a particle and a vortex and contributes to understanding the turbulent flows laden with particles.

Appendix A

Theory

A.1 Derivation of the exact solution of Burgers vortex

Substituting the velocity field of Burgers vortex $u(r,\theta,z) = (-\alpha r, u_\theta(r), 2\alpha z)$ into the Navier-Stokes equation, the Navier-Stokes gives the equation in θ direction is

$$\frac{\partial u_\theta}{\partial t} - \alpha r\left(\frac{u_\theta}{r} + \frac{\partial u_\theta}{\partial r}\right) = \nu\left(\frac{\partial^2 u_\theta}{\partial r^2} + \frac{1}{r}\frac{\partial u_\theta}{\partial r} - \frac{u_\theta}{r^2}\right). \tag{A.1}$$

Circulation is defined as follows:

$$\Gamma(r,t) = 2\pi r u_\theta(r,t), \tag{A.2}$$

which substituted into Eq.(A.1) gives

$$\begin{aligned}
&\frac{\partial}{\partial t}\left(\frac{\Gamma}{2\pi r}\right) - \alpha r\left\{\frac{\Gamma}{2\pi r}\frac{1}{r} + \frac{1}{2\pi r}\left(\frac{\partial\Gamma}{\partial r} - \frac{\Gamma}{r}\right)\right\} \\
&\qquad = \nu\left\{\frac{1}{2\pi r}\left(\frac{\partial^2\Gamma}{\partial r^2} - \frac{2}{r}\left(\frac{\partial\Gamma}{\partial r} - \frac{\Gamma}{r}\right) + \frac{1}{r}\frac{1}{2\pi r}\left(\frac{\partial\Gamma}{\partial r} - \frac{\Gamma}{r}\right) - \frac{1}{r^2}\frac{\Gamma}{2\pi r}\right\},
\end{aligned}$$

$$\frac{\partial\Gamma}{\partial t} - \alpha r\left\{\frac{\Gamma}{r} + \left(\frac{\partial\Gamma}{\partial r} - \frac{\Gamma}{r}\right)\right\} = \nu\left\{\frac{\partial^2\Gamma}{\partial r^2} - \frac{2}{r}\left(\frac{\partial\Gamma}{\partial r} - \frac{\Gamma}{r}\right) + \frac{1}{r}\left(\frac{\partial\Gamma}{\partial r} - \frac{\Gamma}{r}\right) - \frac{\Gamma}{r^2}\right\},$$

$$\frac{\partial\Gamma}{\partial t} - \alpha r\frac{\partial\Gamma}{\partial r} = \nu\left(\frac{\partial^2\Gamma}{\partial r^2} - \frac{1}{r}\frac{\partial\Gamma}{\partial r}\right) \tag{A.3}$$

If $\partial\Gamma/\partial t = 0$, Equation (A.3) becomes

$$\frac{\partial^2\Gamma}{\partial r^2} = \left(\frac{1}{r} - \frac{\alpha}{\nu}r\right)\frac{\partial\Gamma}{\partial r}, \tag{A.4}$$

and substituting $f = \partial\Gamma/\partial r$ into Eq.(A.4), elementary integration yields

$$\frac{\partial f}{\partial r} = \left(\frac{1}{r} - \frac{\alpha}{\nu}r\right)f,$$

$$\int\frac{df}{f} = \int\left(\frac{1}{r} - \frac{\alpha}{\nu}r\right)dr + C,$$

$$\log f = \log r - \frac{\alpha r^2}{2\nu} + C,$$

$$\log\frac{f}{r} = -\frac{\alpha r^2}{2\nu} + C,$$

$$\frac{f}{r} = \frac{1}{r}\frac{\partial\Gamma}{\partial r} = C\exp\left(-\frac{\alpha r^2}{2\nu}\right), \tag{A.5}$$

and resubstituting $f = \partial\Gamma/\partial r$ into Eq.(A.5), elementary integration yields

$$\begin{aligned}\Gamma(r) &= C\int r\exp\left(-\frac{\alpha r^2}{2\nu}\right)dr + B \\ &= A\exp\left(-\frac{\alpha r^2}{2\nu}\right) + B\end{aligned} \tag{A.6}$$

where, A and B are constants. A solution is sought which is regular for $r = 0$; thus, let $A = -B = \Gamma_0$, so that the solution is

$$\Gamma(r) = \Gamma_0\left\{1 - \exp\left(-\frac{\alpha r^2}{2\nu}\right)\right\}, \tag{A.7}$$

and

$$u_\theta(r) = \frac{\Gamma_0}{2\pi r}\left\{1 - \exp\left(-\frac{\alpha r^2}{2\nu}\right)\right\} \tag{A.8}$$

Appendix B

Experiments

B.1 Tracer particle

Figure B.1 shows the tracer particle has the particle size distribution in the range of 56.0μm to 94.6 μm. The average particle diameter is 73.5 μm, and the standard deviation is 9.2μm. From the SEM image of tracer particles (as photographed by Mr. Arata MATSUMOTO, master's student of Osaka university), tracer particle size distribution is measured by using digital image processing (Software: Image J).

The spherical ion exchange resin (DIAION SP20SS:Mitsubishi Chemical (Fig. B.2)) is used as a tracer particle. The spherical resin has a porous surface as shown in Fig. B.3. Fluorescent is absorbed in the surface. Here, the fluorescent dye is Rhodamine B ($C_{28}H_{31}O_3N_2Cl$:NACALAI TESQUE,INC.). This fluorescent have an absorption and an emission peaks around 543 nm and 565 nm, respectively. This tracer is illuminated by Ar-laser (range from 457.9 nm to 514.5 nm:GLG3282,NEC) and emits red light.

B.2 Biometal

BioMetal is a thin fiber-like metal actuator (driving unit) which acts like a muscle. Although it is soft and pliable like a nylon thread under normal conditions, it becomes stiff like a piano wire and sharply contracts when a current is fed through it. If the current is shut off, it will soften and extend back to its original length. It repeatedly works any number of times. The same effect can be obtained by heating it by hot air. Actuators mainly used for extension and contraction are called artificial muscles to distinguish them from ordinary motors. Artificial muscles are generally classified into two types: rubber-based (pneumatic pressure-driven) and chemicals-based (high polymer).

BioMetal is a metal-based artificial muscle made of a shape-memory alloy. Its name is derived from the fact that it is a metal actuator which moves flexibly and smoothly like a living being. BioMetal is a registered trademark of TOKI CORPORATION. It is incorporated into two families of products: thread-like BioMetal Fiber (BMF series) and microcoil-like BioMetal Helix (BMX series).

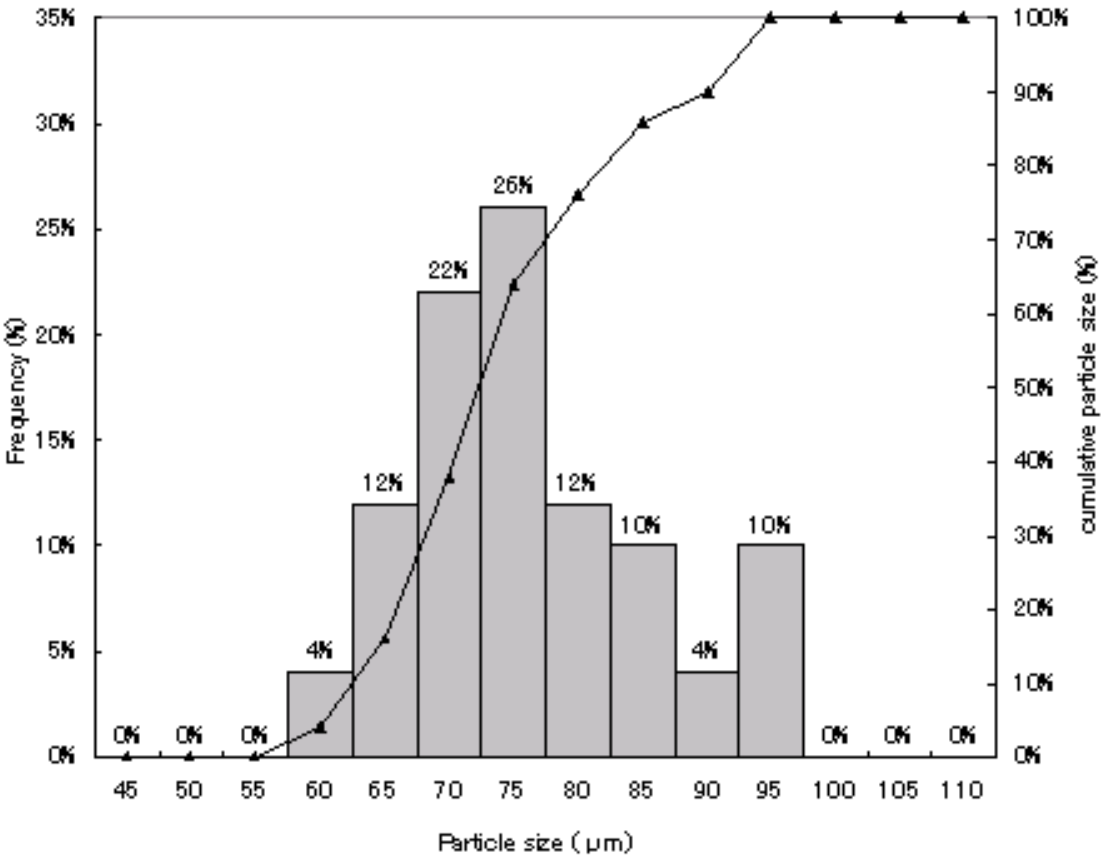

Figure B.1: Particle size distribution of tracer particle

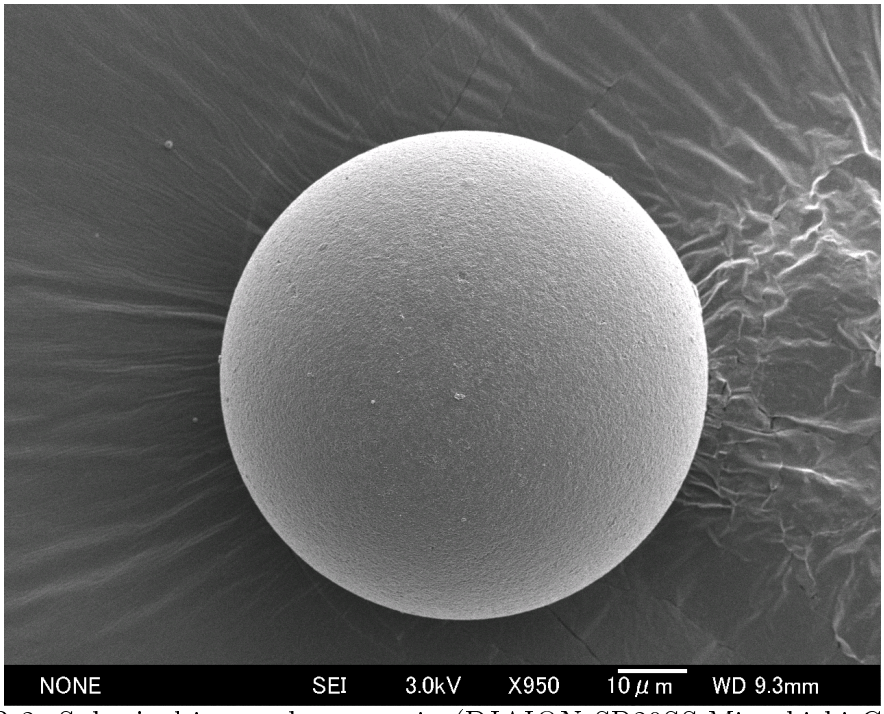

Figure B.2: Spherical ion exchange resin (DIAION SP20SS:Mitsubishi Chemical)

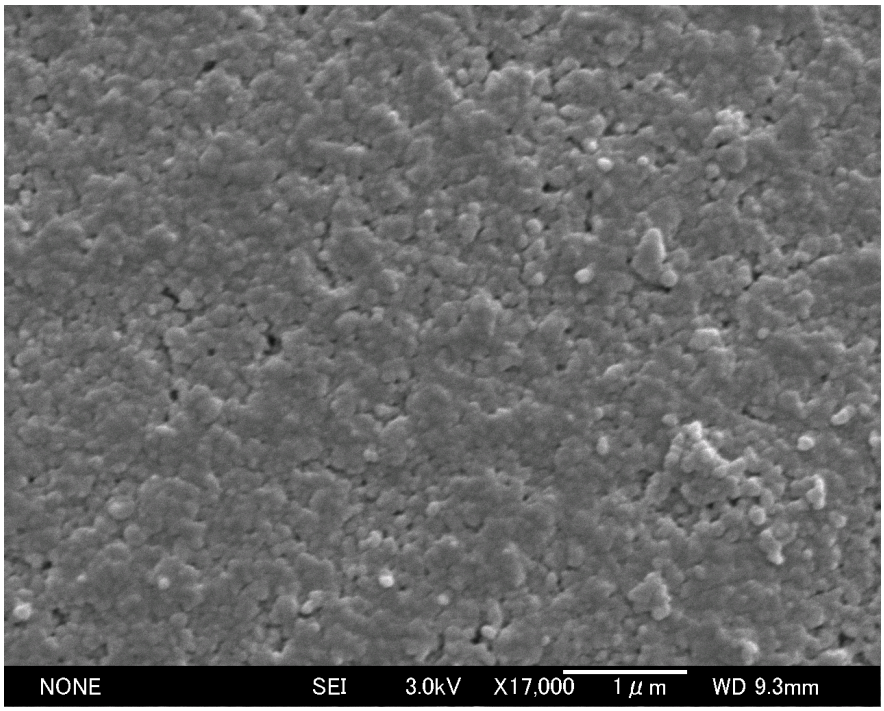

Figure B.3: Surface of spherical ion exchange resin

Nomenclature

$\mathrm{BVD}(r,\theta)$	: Balance between Vorticity and Divergence, [1/sec]
$C(x,y)$	: cross correlation table, [bit]
C_d	: drag coefficient, [-]
d_p	: particle diameter, [m]
$\mathrm{div}_{r\theta}\mathbf{u}$	: superficial divergence, [1/sec]
$\mathrm{div}_{r\theta}\mathbf{u_{max}}$	: maximum superficial divergence, [1/sec]
Error	: measurement error, [pixel]
f	: focal length, [m]
$f(x,y,t)$	: luminance function, [bit]
$I(x,y)$	: interrogation window table, [bit]
I_0	: light intensity, [bit]
L	: spacing between area sensors, [m]
l_b	: Burgers length scale, [m]
$l_{sub}(x,y)$	: sub-pixel displacement, [m]
Re_p	: particle Reynolds number, [-]
Re_Γ	: vortex Reynolds number, [-]
$S(x,y)$	: search window table, [bit]
St	: Stokes number, [-]
U	: particle velocity detected by the particle velocimetry system, [m/sec]
U_c	: convective vector, [m/sec]
$\mathbf{u_{exact}}$	: exact vector of Burgers vortex, [pixel/sec]
$\mathbf{u_{piv}}$	: resulting vector of PIV, [pixel/sec]
$u(r,\theta,z)$	: velocity field in the cylindrical coordinate, [m/sec]
$u^*_{i,j}$	: interpolated vector, [m/sec]
$\lvert\mathbf{u_f}-\mathbf{u_p}\rvert$	: relative velocity between flow and particle, [m/sec]
$\overline{U}_z$	: mean flow velocity, [m/sec]
$u_\theta(r)$	: circumferential velocity, [m/sec]

$\vec{v}$	: velocity vector of Hopfield network, [m/sec]
v_K	: Kolmogorov velocity, [m/sec]
v_{rms}	: root mean square value of velocity fluctuation, [m/sec]
V_{zemp}	: particle velocity calculated by empirical equation, [m/sec]
V_{zexp}	: particle velocity detected by particle velocimetry system, [m/sec]
z	: relative distance between particle and observation plane, [m]
α	: strain rate of the stagnation point flow, [1/sec]
ϵ	: rate of dissipation of energy, [m^2/sec^3]
η	: Kolmogorov length scale, [m]
λ	: Taylor microscale, [m]
ν	: kinematic coefficient of viscosity, [m^2/sec]
ρ_f	: density of fluid, [Kg/m^3]
ρ_p	: density of particle, [Kg/m^3]
τ_f	: particle's residence time, [sec]
τ_K	: Kolmogorov time, [sec]
τ_p	: particle response time, [sec]
$\omega(r, \theta, t)$	: quasi-three dimensional vorticity, [1/sec]
$\omega(r, \theta, z)$	: vorticity in the cylindrical coordinate, [1/sec]
ω_{Bmax}	: maximum vorticity of Burgers vortex in static flow, [1/sec]
ω_{Pmax}	: maximum vorticity of vorticities shed from particle in static flow, [1/sec]
ω_{zmax}	: maximum vorticity of Burgers vortex, [1/sec]
Γ	: circulation, [m^2/sec]
$\Gamma(t)$	: circulation of the Burgers vortex, [m^2/sec]
Γ_0	: circulation in the forced vortex area, [m^2/sec]
ΔT	: time delay, [sec]

Bibliography

[1] Y. Tsuji, Y. Morikawa and H. Shiomi, "LDV measurements of an air-solid two-phase flow in a vertical pipe", *J. Fluid Mech*, **139**, (1984), pp.417-434.

[2] M. Rashidi, G. Hetsroni and S. Banerjee, "Particle-turbulence interaction in a boundary layer", *Int. J. Multiphase Flow*, **16**-6, (1990), pp.935-949.

[3] K.D. Squires and J.K. Eaton, "On the preferential concentration of solid particles in turbulent", *Phys.Fluids A*, **3**-3, (1991), pp.1169-1178.

[4] J.R. Fessler, J.D. Kulick and J.K. Eaton, "Preferential concentration of heavy particles in a turbulent channel flow", *Phys.Fluids*, **6**-11, (1994), pp.3742-3749.

[5] Y. Pan and S. Banerjee, "Numerical simulation of particle interactions with wall turbulence", *Phys. Fluids*, **8**-10, (1996), pp.2733-2755.

[6] M. Boivin, O. Simonin and K.D. Squires, "Direct numerical simulation of turbulence modulation by particles in isotropic turbulence", *J.Fluid Mech.*, **375**, (1998), pp.235-263.

[7] A.M. Ahmed and S. Elghobashi, "On the mechanisms of modifying the structure of turbulent homogeneous shear flows by dispersed particles", *Phys.Fluids*, **12**-11, (2000), pp.2906-2930.

[8] A. Vincent and M. Meneguzzi, "The spatial structure and statistical properties of homogeneous turbulence", *J.Fluid Mech.*, **225**, (1991), pp.1-20.

[9] S. Douady, Y. Couder and M.E. Brachet, "Direct observation of the intermittency of intense vorticity filaments in turbulence", *Phys. Rev. Lett*, **67**-8, (1991), pp.983-987.

[10] J. Jiménez, A.A. Wray, P.G. Saffman and R.S. Rogallo, "The structure of intense vorticity in isotropic turbulence", *J.Fluid Mech.*, **255**, (1993), pp.65-90.

[11] U. Frisch, "*Turbulence*", Cambridge University Press, (1995), pp.182-188.

[12] I. Hosokawa, S. Oide and K. Yamamoto, "Existence and significance of 'soft worms' in isotropic turbulence", *J.Phys.Soc.Jpn.*, **66**-10, (1997), pp.2961-2964.

[13] K. Fujibayashi, M. Tanahashi and T. Miyauchi, "Hierarchical structure and clusters of coherent fine-Scale eddies in homogeneous isotropic turbulence", *JSFM-18*, (2004), **A3-4** (on CD-ROM), (in Japanese).

[14] M. Tanahashi, S.J. Kang, T. Miyamoto, S. Shiokawa and T. Miyauchi, "Scaling law of fine scale eddies in turbulent channel flows up to Re_T =800", *Int. J. Heat and Fluid Flow*, **25**, (2004), pp.331-340.

[15] J.M. Burgers, "A mathematical model illustrating the theory of turbulence", *Adv.Appl.Mech.*, **1**, (1948), pp.171-199.

[16] N. Hatakeyama and T. Kambe, "Statistical laws of random strained vortices in turbulence", *Phys. Rev. Lett*, **79**-7, (1997), pp.1257-1260.

[17] T. Kambe and N. Hatakeyama, "Statistical laws and vortex structures in fully developed turbulence", *Fluid Dyn. Res.*, **27**, (2000), pp.247-267.

[18] T.S. Lundgren, "Strained spiral vortex model for turbulent fine structure", *Phys. Fluids*, **25**-12, (1982), pp.2193-2203.

[19] D.I. Pullin and T.S. Lundgren, "Axial motion and scalar transport in stretched spiral vortices", *Phys. Fluids*, **13**-9, (2001), pp.2553-2563.

[20] G. Kawahara, S. Kida, M. Tanaka and S. Yanase, "Energy dissipation in spiral vortex layers wrapped around a straight vortex tube", *Phys. Fluids*, **17**, (2005), pp.055111-1-055111-13.

[21] T. Kambe, *J.Phys.Soc.Jpn.*, "Axisymmetric vortex solution of Navier-Stokes equation", **53**-1, (1984), pp.13-15.

[22] N. Rott, "On the Viscous Core of a Line Vortex", *Z. angew. Math. Phys.*, **9**-5-6, (1958), pp.543-553.

[23] P. Bagchi and S. Balachander, "Response of the wake of an isolated particle to an isotropic turbulent flow", *J. Fluids Mech*, vol. 518, (2004), pp. 95-123.

[24] I. Kim, S. Elghobashi and W.A. Sirignano, "Unsteady flow interactions between an advected cylindrical vortex tube and a spherical particle", *J.Fluid Mech*, **288**, (1995), pp.123-155.

[25] H. Niazmand and M. Renksizbulut, "Viscous interaction between a vortex tube and a rotating spherical particle", *Part. Part. Syst. Charact.*, **20**, (2003), pp.47-61.

[26] I. Kim, S. Elghobashi and W.A. Sirignano, "Unsteady flow interactions between a pair of advected vortex tubes and a rigid sphere", *Int. J. Multiphase Flow*, **23**-1, (1997), pp.1-23.

[27] M. Sun and J.S. Marshall, "A flow visualization study of vortex interaction with the wake of a sphere", *J. Fluids Eng* , **122**, (2000), pp.560-568.

[28] J. Sakakibara and T. Anzai, "Chain-link-fence structures produced in a plane jet", *Phys.Fluids* , **13**, (2001), pp.1541-1544.

[29] W.J.M. Rankine, "*A Manual Applied Mechanics*", 21ed, C. Griffin, (1921), pp.574-578.

[30] P.A. Davidson, "*turbulence*", OXFORD University Press, (2004), pp.76-80.

[31] Y. Tanaka, G. Oba and Y. Hagiwara, "Experimental study on the interaction between large scale vortices and particles in liquid-solid two-phase flow", *Int. J. Multiphase Flow*, **29**, (2003), pp.361-373.

[32] A.R. Khan and J.F. Richardson, "The resistance to motion of a solid sphere in a fluid", *Chem. Eng. Comm*, **62**, (1987), pp.135-150.

[33] M. Raffel, C. Wilert and J. Kompenhans, "Particle Image Velocimetry", Second edition,(2007), Springer, New York, pp.1-13.

[34] "PIV Handbook", edited by Visualization Society of Japan, Tokyo, (2002), Morikita Shuppan, pp.1-7 (in Japanese).

[35] C.E. Willert and M. Gharib, "Digital particle image velocimetry", *Exp in Fluids.*, **10**, (1991), pp.181-193.

[36] Y. Yamamoto, M. Nishida and T. Uemura, "Super-Resolution PIV by accelerated successive abandonment method", *Jour. of the Visualization Society of Japan*, Vol.21 Suppl. No.1, (2001), pp.43-44 (in Japanese).

[37] M. Ishikawa, Y. Murai, T. Matsubara and F. Yamamoto, "Validation and application of a gradient-based PIV algorithm constructed by recursive image processing", *PSFVIP-3* Maui, Hawaii 18-21 March 2001, (2001), **F3111** (on CD-ROM).

[38] Y. Sugii, T. Okuno and S. Nishino, "High-resolution adaptive PIV technique using gradient method", *9th. International Symposium on Flow Visualization*, Heriot-Watt University, Edinburgh 2000, (2000), **337** (on CD-ROM).

[39] Y. Sugii, S. Nishio, T. Okuno and K. Okamoto, "A highly accurate iterative PIV technique using a gradient method", *Meas. Sci. Technol.* **11**, (2000), pp.1666-1673.

[40] S. Nishio, Y. Sugii and T. Okuno, "Analytics of PIV measurement for its higher performances", *4th International Symposium on Particle Image Velocimetry Göttingen*, Germany, September 2001 PIV'01, (2001), Paper 1066 (on CD-ROM).

[41] D.P. Hart, "PIV error correction", *Exp in Fluids.*, **29**, (2000), pp.13-22.

[42] I. Kimura, N. Yamasita and Y. Kuroe, "Determination of erroneous velocity vectors using neural network", *Trans. JSME.*, (B), **920**, (1992), pp.310-312 (in Japanese).

[43] Y. Murai, T. Ido, M. Ishikawa, and F. Yamamoto, "Development of the post-processing method for PIV measurement result using computational fluid dynamics procedure", *Trans. JSME.*, (B) Vol.64, No.626, (1997), pp.109-116 (in Japanese).

[44] Y. Tanaka, "Experimental study on the interaction between large scale vortices and particles in solid-liquid two-phase flow", *Master's thesis*, Kyoto institute of technology, Department of Mechanical engineering, (2002).

[45] J. Hinze, "*Turbulence*", Second edition, McGraw-Hill Mechanical Engineering, (1975), pp.44-48.

List of publications

Papers in Scientific journal

(1) Y. Tanaka, K. Otsu, T. Kawaguchi and Y. Tsuji, "Experimental study on the interaction between Burgers vortex and a solid particle using 2D PIV measurement", *Journal of ISEM* **7**, Special issue, (2007), pp.17-20.

(2) Y. Tanaka, K. Otsu, T. Tsuji and T. Tanaka, "Influence of a Gravitationally-Settling Particle on a Burgers Vortex", *JSME* **734**, B in Japanese, (2007), pp.2107-2115.

Presentations at International conference

(1) Y. Tanaka, K. Otsu, T. Kawaguchi and Y. Tsuji, "Development of an in-line stereoscopic PIV system to 3-component velocity measurements with a single camera", *The Fifth World Congress on Par-ticle Technology*, Orland, Florida, USA, 23-27 April, (2006), **245C** (on CD-ROM).

(2) Y. Tanaka, K. Otsu, T. Kawaguchi and Y. Tsuji, "Experimental study on the interaction between Burgers vortex and a solid particle using 2D PIV measurement", *International Symposium on Advanced Fluid/Solid Science and Technology in Experimental Mechanics*, Sapporo, Hokkaido, Japan, 11-14 September, (2006) **A1-3** (on CD-ROM).

(3) Y. Tanaka, T. Tsuji, T. Kawaguchi, T. Tanaka and Y. Tsuji, "Experimental study on the interaction between Burgers vortex and a solid particle using 2D PIV measurement", *59th Annual Meeting of the division of Fluid Dynamics*, Tampa, Florida, USA, 19-21 November, (2006), **59**, p.28.

(4) Y. Tanaka, K. Otsu, T. Tsuji and T. Tanaka, "Measurement of the interaction between a single particle and a single Burgers vortex", *5th Joint ASME/JSME Fluids Engineer-ing Conference*, San Diego, California, USA, 30 July-2 August, (2007), **FEDSM2007-37217** (on CD-ROM).

(5) Y. Tanaka, T. Tsuji and T. Tanaka, "Experimental study on the interaction between Burgers vortex and single particle for modeling of a particulate turbulent flow", *5th international symposium on Turbulence and Shear Flow Phenomena, Proceedings*, Munich, Germany, 27-29 August, (2007), **3**, pp.1343-2348.

(6) Y. Tanaka, K. Otsu, T. Tsuji and T. Tanaka, "Interaction between Burgers vortex and a settling particle", *The second Inter-national Symposium on Advanced Fluid/Solid Science and Technology in Experimental Mechanics*, Suita, Osaka, Japan, 23-25 September (2007), **69** (on CD-ROM).